LUND UNIVERSITY

Light-Matter Interaction and Quantum Computing in Rare-Earth-Ion-Doped Crystals

Kinos, Adam

2018

Citation for published version (APA):
Kinos, A. (2018). *Light-Matter Interaction and Quantum Computing in Rare-Earth-Ion-Doped Crystals*. [Doctoral Thesis (compilation), Atomic Physics]. Atomic Physics, Department of Physics, Lund University.

LUND UNIVERSITY

PO Box 117
221 00 Lund
+46 46-222 00 00

Light-Matter Interaction and Quantum Computing in Rare-Earth-Ion-Doped Crystals

ADAM KINOS
DEPARTMENT OF PHYSICS | FACULTY OF ENGINEERING | LUND UNIVERSITY

Light-matter interaction and quantum computing in rare-earth-ion-doped crystals

Adam Kinos

Doctoral Thesis
2018

LUND UNIVERSITY

Akademisk avhandling som för avläggande av teknologie doktorsexamen vid tekniska fakulteten vid Lunds Universitet kommer att offentligen försvaras den 2 mars 2018, kl. 09.15 i Rydbergs sal, på Fysiska Institutionen, Professorsgatan 1, Lund.

Fakultetsopponent: Dr. Charles W. Thiel
Montana State University, USA

Academic thesis which, by due permission of the Faculty of Engineering at Lund University, will be publicly defended on 2nd of March 2018, at 09.15 a.m. in Rydberg's hall, at the Department of Physics, Professorsgatan 1, Lund, for the degree of Doctor of Philosophy in Engineering.

Faculty opponent: Dr. Charles W. Thiel
Montana State University, USA

Organization
LUND UNIVERSITY

Division of Atomic Physics
Department of Physics
P.O. Box 118
SE-221 00 Lund, Sweden

Document name
DOCTORAL DISSERTATION

Date of issue
January, 2018

Sponsoring organization

Author
Adam Kinos

Title and subtitle
Light-Matter Interaction and Quantum Computing in Rare-Earth-Ion-Doped Crystals

Abstract

In this thesis, crystals of yttrium orthosilicate (Y_2SiO_5) that are randomly doped with another rare-earth element, such as praseodymium (Pr), europium (Eu), or cerium (Ce), are investigated with lasers locked to ultra-stable cavities using the Pound-Drever-Hall locking technique.

Many of these rare-earth elements have long-lived 4f-4f transitions, hundreds of microseconds to a few milliseconds, with even longer ground hyperfine lifetimes of up to several days. The coherence properties are, to the best of the author's knowledge, the longest achieved for any material, currently with a record of six hours for the nuclear spin states of Eu^{3+}:Y_2SiO_5 measured at cryogenic temperatures. Furthermore, due to natural trapping and differences in the local environments, each dopant ion experiences a slightly different crystal field, and thus an inhomogeneity in the 4f-4f transition exists between all ions in a crystal. Since the homogeneous linewidth is in the order of kHz or below, whereas the inhomogeneous profile can be several GHz wide, these materials have dense storing capabilities.

This thesis explores how light interacts with such rare-earth-ion-doped crystals; how the absorption and light polarization varies during propagation; how spectral features in the inhomogeneous absorption profile can be tailored to create narrowband spectral filters; how the speed of light is slowed down significantly in such narrow transmission windows; and how that can be used to either frequency shift incoming light, control its group velocity, or temporally compress pulses.

It also uses rare-earth-ions to research quantum computing, the field of using quantum mechanical effects such as superpositions and entanglements to outperform classical computers on certain specific problems. This is done by examining how two-color pulses can be used to rapidly induce coherence from an initially mixed state; how qubit-qubit interactions can be performed experimentally using ensemble qubits, which opens the door to two-qubit experiments such as the CNOT-gate and entanglements; how a scalable quantum computer might be constructed using a single ion qubit approach with a dedicated readout ion and buffer ion(s) to improve readout fidelity; and how cerium is investigated as a candidate for such a dedicated readout ion.

Key words:
Rare-earth-ion-doped crystals, Light-matter interaction, Quantum computing, Slow light

Classification system and/or index terms (if any):

Supplementary bibliographical information:

Language
English

ISSN and key title:
ISSN 0281-2762, Lund Reports on Atomic Physics, LRAP-543

ISBN
978-91-7753-543-0

Recipient's notes

Number of pages
219

Price

Security classification

Signature Adam Kinos

Date January 22nd 2018

Light-matter interaction and quantum computing in rare-earth-ion-doped crystals

Adam Kinos

Doctoral Thesis
2018

Light-matter interaction and quantum computing in rare-earth-ion-doped crystals

Printed in Sweden by Media-Tryck, Lund, 2018

Division of Atomic Physics
Department of Physics
Faculty of Engineering, LTH
Lund University
P.O. Box 118
SE–221 00 Lund
Sweden

http://www.atomic.physics.lu.se

ISSN: 0281-2762
Lund Reports on Atomic Physics, LRAP-543 (2018)

ISBN (print): 978-91-7753-543-0
ISBN (pdf): 978-91-7753-544-7

ABSTRACT

In this thesis, crystals of yttrium orthosilicate (Y_2SiO_5) that are randomly doped with another rare-earth element, such as praseodymium (Pr), europium (Eu), or cerium (Ce), are investigated with lasers locked to ultra-stable cavities using the Pound-Drever-Hall locking technique.

Many of these rare-earth elements have long-lived 4f-4f transitions, hundreds of microseconds to a few milliseconds, with even longer ground hyperfine lifetimes of up to several days. The coherence properties are, to the best of the author's knowledge, the longest achieved for any material, currently with a record of six hours for the nuclear spin states of Eu^{3+}:Y_2SiO_5 measured at cryogenic temperatures. Furthermore, due to natural trapping and differences in the local environments, each dopant ion experiences a slightly different crystal field, and thus an inhomogeneity in the 4f-4f transition exists between all ions in a crystal. Since the homogeneous linewidth is in the order of kHz or below, whereas the inhomogeneous profile can be several GHz wide, these materials have dense storing capabilities.

This thesis explores how light interacts with such rare-earth-ion-doped crystals; how the absorption and light polarization varies during propagation; how spectral features in the inhomogeneous absorption profile can be tailored to create narrowband spectral filters; how the speed of light is slowed down significantly in such narrow transmission windows; and how that can be used to either frequency shift incoming light, control its group velocity, or temporally compress pulses.

It also uses rare-earth-ions to research quantum computing, the field of using quantum mechanical effects such as superpositions and entanglements to outperform classical computers on certain specific problems. This is done by examining how two-color pulses can be used to rapidly induce coherence from an initially mixed state; how qubit-qubit interactions can be performed experimentally using ensemble qubits, which opens the door to two-qubit experiments such as the CNOT-gate and entanglements; how a scalable quantum computer might be constructed using a single

ion qubit approach with a dedicated readout ion and buffer ion(s) to improve readout fidelity; and how cerium is investigated as a candidate for such a dedicated readout ion.

POPULÄRVETENSKAPLIG SAMMANFATTNING

Ljus-materia växelverkan är något som finns överallt: ljus genereras i lampor; absorberas eller reflekteras av material; fokuseras på näthinnorna med hjälp av linserna i våra ögon; tapparna och stavarna absorberar ljuset; och signaler skickas via synnerven vidare till hjärnan så att vi kan tolka världen runtom oss i färger, mörker, och ljus.

Väldigt kortfattat fungerar det enligt följande: det inkommande ljusets svängningar får atomernas elektroner att börja svänga och skicka ut sitt eget ljus, som tillsammans med det ursprungliga ljuset, likt två vattenvågor, kan släcka ut eller förstärka varandra. Samtidigt kan atomerna absorbera energin från ljusvågen och exciteras.

Denna avhandlingen handlar om hur ljus interagerar med ett specifikt material, nämligen kristaller dopade med sällsynta jordartsmetaller som, t.ex., praseodymium eller europium. Sådana atomer är intressanta att undersöka eftersom de har väldigt långa livstider, vilket betyder att de kan vara exciterade en relativt (millisekunder) lång tid innan de åter faller tillbaka till grundtillståndet, ibland genom att skicka ut nytt ljus.

De dopade kristallerna undersöks i anknytning till kvantdatorer som, i kontrast med en vanlig dator vars bitar endast kan vara nollor och ettor, har kvantbitar som även kan vara i tillstånd som är både noll och ett samtidigt, så kallade superpositioner. Man kan säga att en kvantdator har tillgång till fler valmöjligheter för varje kvantbit. Dock, när man ska läsa ut vad en kvantbit är, får man alltid antingen noll eller ett som svar, även om kvantbiten innan man gjorde utläsningen var lite av båda samtidigt. Detta betyder att utläsningen av en vanlig bit och en kvantbit båda innehåller endast en enhet av information (även kallat en bit av information). Vid första anblicken kan man därför tro att en kvantdator inte tillför något som en klassisk dator inte redan har, men tack vara en kvantdators förmåga att använda kvantmekaniska fenomen såsom superpositioner och sammanflätningar (engelska: entanglement) kan vissa problem lösas mycket snabbare än på en vanlig dator; man måste bara tänka till ordentligt angående vilken information man vill få ut i slutändan och hur denna beror på kvantinformationen under beräkningen.

I nuläget är kvantdatorer i ett tidigt skede, men utvecklingen av flera olika implementationer går fort framåt. I denna avhandlingen undersöks som sagt kristaller dopade med sällsynta jordartsmetaller där två olika energinivåer hos atomerna används som nollor och ettor i kvantbitarna. Det som undersöks är hur man experimentellt kan få två kvantbitar, var och en bestående av miljontals atomer, att interagera. För att dock kunna skala systemet till flera kvantbitar måste man gå mot att använda enskilda atomer till varje kvantbit. Svårigheten är då istället utläsningen av om en kvantbit är i noll eller ett. Detta har vår grupp länge försökt lösa genom att använda cerium som en hängiven utläsningsatom, och även om vi ännu inte lyckats detektera en enskild ceriumatom så har en permanent hålbränningsprocess upptäckts i materialet vi studerar, något som dessvärre ytterligare försvårar experimenten.

Kristaller dopade med sällsynta jordartsmetaller är också speciella eftersom man kan skräddarsy hur atomerna absorberar ljus med lite olika frekvenser (färger), något som i vissa fall kan bibehållas i upp till dagar utan att förändras märkbart. Detta kan användas till mycket och här undersöks vissa sådana strukturer som kan absorbera respektive transmittera ljus som skiljer sig ytterst lite i frekvens; sakta ner ljus så att det endast rör sig med en bråkdel av hastigheten som det normalt färdas med; eller med hjälp av en elektrisk ström skifta frekvensen något på inkommande ljus.

LIST OF PUBLICATIONS

This thesis is based on the following papers, which will be referred to in the text by their roman numerals. Note that the thesis author previously published under Adam N. Nilsson.

I **Wave propagation in birefringent materials with off-axis absorption or gain**
M. Sabooni, A. N. Nilsson, G. Kristensson, and L. Rippe.
Phys. Rev. A **93**, 013842 (2016).

II **Development and characterization of high suppression and high étendue narrowband spectral filters**
A. Kinos, Q. Li, L. Rippe, and S. Kröll.
Appl. Opt. **Vol. 55 No. 36**, 10442 (2016).

III **Slow-light-based optical frequency shifter**
Q. Li, Y. Bao, A. Thuresson, A. N. Nilsson, L. Rippe, and S. Kröll.
Phys. Rev. A **93**, 043832 (2016).

IV **Using electric fields for pulse compression and group-velocity control**
Q. Li, A. Kinos, A. Thuresson, L. Rippe, and S. Kröll.
Phys. Rev. A **95**, 032104 (2017).

V **Fast all-optical nuclear spin echo technique based on EIT**
A. Walther, A. N. Nilsson, Q. Li, L. Rippe, and S. Kröll.
Eur. Phys. J. D **70:**, 166 (2016).

VI **Towards CNOT operations using ensemble qubits**
A. Kinos, L. Rippe, A. Walther, and S. Kröll.
(2018) *Manuscript in preparation.*

VII **High-fidelity readout scheme for rare-earth solid-state quantum computing**
A. Walther, L. Rippe, Y. Yan, J. Karlsson, D. Serrano, A. N. Nilsson, S. Bengtsson, and S. Kröll.
Phys. Rev. A **92**, 022319 (2015).

VIII **High-resolution transient and permanent spectral hole burning in $\mathbf{Ce^{3+}{:}Y_2SiO_5}$ at liquid helium temperatures**
J. Karlsson*, A. N. Nilsson*, D. Serrano, A. Walther, P. Goldner, A. Ferrier, L. Rippe, and S. Kröll;
(*Authors contributed equally).
Phys. Rev. B **93**, 224304 (2016).

Other publications by the author not included in this thesis:

Competitive binding-based optical DNA mapping for fast identification of bacteria - multi-ligand transfer matrix theory and experimental applications on Escherichia coli

A. N. Nilsson*, G. Emilsson*, L. K. Nyberg, C. Noble, L. S. Stadler, J. Fritzsche, E. R. B. Moore, J. O. Tegenfeldt, T. Ambjörnsson, and F. Westerlund;
(*Authors contributed equally).
Nucleic Acids Res. **42**, e118 (2014).

A fast and scalable kymograph alignment algorithm for nanochannel-based optical DNA mappings

C. Noble, A. N. Nilsson, C. Freitag, J. P. Beech, J. O. Tegenfeldt, and T. Ambjörnsson.
PLOS One **10**, e0121905 (2015).

Visualizing the entire DNA from a chromosome in a single frame

C. Freitag, C. Noble, J. Fritzsche, F. Persson, M. Reiter-Schad, A. N. Nilsson, A. Graneli, T. Ambjörnsson, K. U. Mir, and J. O. Tegenfeldt.
Biomicrofluidics **9**, 044114 (2015).

Bacteriophage strain typing by rapid single molecule analysis

A. Grunwald, M. Dahan, A. Giesbertz, A. N. Nilsson, L. K. Nyberg, E.Weinhold, T. Ambjörnsson, F. Westerlund, and Y. Ebenstein.

Nucleic Acids Res. **43**, e117 (2015).

Rapid identification of intact bacterial resistance plasmids via optical mapping of single DNA molecules

L. K. Nyberg, S. Quaderi, G. Emilsson, N. Karami, E. Lagerstedt, V. Muller, C. Noble, S. Hammarberg, A. N. Nilsson, F. Sjoberg, J. Fritzsche, E. Kristiansson, L. Sandegren, T. Ambjörnsson, and F. Westerlund.

Sci. Rep. **6**, 30410 (2016).

Super-resolution genome mapping in silicon nanochannels

J. Jeffet, A. Kobo, T. Su, A. Grunwald, O. Green, A. N. Nilsson, E. Eisenberg, T. Ambjörnsson, F. Westerlund, E. Weinhold, D. Shabat, P. K. Purohit, and Y. Ebenstein.

ACS Nano **10 (11)**, 9823-9830 (2016).

ABBREVIATIONS

AOM	Acousto-Optic Modulator
BP	Band Pass filter
CCD	Charge-Coupled Device
CNOT	Controlled NOT
DM	Dichroic Mirror
ECDL	External Cavity Diode Laser
EIT	Electromagnetically Induced Transparency
EOM	Electro-Optic Modulator
FWHM	Full Width at Half Maximum
OD	Optical Diode
PBS	Polarizing Beam Splitter
PDH	Pound-Drever-Hall locking technique
PH	Pinhole
PMT	Photomultiplier Tube
SMF	Single Mode Fiber
SPAD	Single Photon counting Avalanche Diode
TC pulse	Two-Color pulse

Ce	Cerium
Eu	Europium
Nd	Neodymium
Pr	Praseodymium
Y_2O_3	Yttrium Oxide
Y_2SiO_5	Yttrium Orthosilicate

CONTENTS

Papers

CHAPTER 1

INTRODUCTION

The human striving for improvement, be it in happiness, power, sports, or manufacturing, leads to an ever-increasing knowledge base of society. During the last few centuries, we have gone through an industrial revolution, the atomic, jet, and space age, and now after the digital revolution, we are in the information age.

As our knowledge increases, it is important to remember why, on a fundamental level, we believe nature behaves as it does. A comprehensive and thought-provoking overview is given in the Feynman Lectures of Physics volume 1 [1], volume 2 [2], and volume 3 [3], which I use throughout my thesis as references for general physical phenomena.

As equipment and techniques became more refined, people were able to probe into the large and small: general relativity and quantum mechanics, respectively. The work presented in this thesis is mainly focused on a subset of the latter: quantum computing, particularly using rare-earth-ion-doped crystals.

This raises the eternal question of why? Why should we invest our time and resources in quantum computing? One simple answer is curiosity. As research progresses, our understanding of the underlying principles improves, and for me that is reason enough. However, a more fruitful answer might be the historical benefits of pursuing new insights, from the ballistic trajectories of Newtonian mechanics [4], to the general relativity-dependent Global Positioning System (GPS) [5]. Similarly, quantum mechanics is the foundation on which modern computers with their transistors and semiconductors are based. In Chapter 6, I briefly provide more arguments as to why one should pursue quantum computing and list several companies that are already investing time and money in solving the problem of building a quantum computer.

Another question might also arise: what is quantum computing? It is the practical engineering of a device capable of controlling its parts in a quantum mechanical way such that it includes superpositions and entanglements, as well as inventing algorithms that use those quantum resources to achieve a (potential, not proven) speed-up compared to classical computers. Algorithms have already been invented for specific problems, but remember that day-to-day usage of a computer would not currently benefit from quantum mechanical effects.

As mentioned earlier, this thesis is primarily about engineering such a quantum computer using rare-earth-ion-doped crystals, but it also contains a fair bit of light-matter interaction, especially in connection with these materials.

1.1 A personal perspective

"Fall in love with some activity, and do it! Nobody ever figures out what life is all about, and it doesn't matter. Explore the world. Nearly everything is really interesting if you go into it deeply enough. Work as hard and as much as you want to on the things you like to do the best. Don't think about what you want to be, but what you want to do. Keep up some kind of a minimum with other things so that society doesn't stop you from doing anything at all."
- Richard Feynman (allegedly).

A few years ago I decided that quantum computing was a topic I wanted to explore further, and so I started as a PhD student in the quantum information group here at Lund University. The mix between light-matter interaction theory and experiments intrigued me as it allowed for the opportunity to increase both my fundamental and my application-based knowledge in a very interesting field. It has also given me time to teach undergraduates the basics of waves and optics, optical pumping, high spectral resolution spectroscopy, light-matter interaction, and quantum computing, which has been a joyful learning experience for me and hopefully my students.

I have always enjoyed mathematics, and my interest in physics has grown to a desire to understand the fundamentals of nature, be it in quantum mechanics, particle physics, astronomy, chemistry, or biology. My work here has taught me about light-matter interaction and quantum mechanics, and it is my sincerest hope that this thesis will convey some of that knowledge to future PhD students and remind me of everything I have learned during this time.

1.2 A brief overview of the work performed

The main goal of my project has been to improve the quantum computing progress in rare-earth-ion-doped crystals. Some effort has been put into generating high fidelity single qubit gates, but this has not yet resulted in any publication. However, qubit-qubit interactions have been studied for ensemble qubits in order to provide useful experience in preparation for the single ion qubit scheme, which has also been investigated through the, unfortunately unsuccessful, attempts to detect a single cerium ion to be used as a dedicated readout ion.

I have not been able to resist the temptation to explore the light-matter interaction topic through wave propagation simulations and slow light applications, which was not my main aim but nevertheless became a large part of my PhD project.

1.3 Outline of the thesis

Since understanding physics is my own personal driving force, this thesis starts off with the basic physical processes and slowly gets into more application-based descriptions. I have therefore chosen to move most of the equipment description to the end of this thesis in Appendix A.

I am a firm believer of the Feynman Technique [6] where learning is an iteration between studying; pretending or actually teaching the topic to a colleague or classroom in simple terms; identifying knowledge gaps, which is made easier by the teaching of the subject; and going back to studying and improving the simplifications and analogues to take the complex subject into the familiar realm in order to further increase knowledge and intuition about the problem. This thesis thus contains some sections that might seem very easy and trivial, but I wanted to include them for the sake of completeness.

Chapter 2 investigates light-matter interaction from the electric field and wave point of view, whereas Chapter 3 discusses quantum phenomena from the perspective of atoms. These two chapters are very general and it is not until Chapter 4 that I introduce the rare-earth-ion-doped crystals, which are so central to this thesis, by discussing their properties. After this theoretical background is given, Chapter 5 presents the results of Papers **I-IV**.

At this point, the thesis shifts focus to quantum computing with a brief overview in Chapter 6 before Chapter 7 presents our efforts in the field and discusses Papers **V-VIII**.

The thesis concludes in Chapter 8 where I try to compress the results of my work during the past four years into a few pages.

CHAPTER 2

UNDERSTANDING LIGHT-MATTER INTERACTION

To understand and appreciate the work of Papers **I**-**IV**, three things are needed: knowledge about atoms and rare-earth-ion-doped crystals, which are discussed in Chapters 3 and 4, respectively, and an intuitive understanding of light-matter interaction, which is presented in this chapter. Note that the discussions are somewhat simplified, as they do not fully consider all quantum mechanical effects.

Section 2.1 aims at giving the reader a qualitative picture of how light interacts with matter, and why it normally slows down when propagating through anything but vacuum, i.e., explaining the refractive index of materials. Starting in Section 2.1.1, an accelerating charge is studied with regard to the light it radiates out. In Section 2.1.2, an atom-swing analogy is presented to provide a more intuitive understanding of how the light field radiated by oscillating charges relates to an incoming field. A mathematical description of how light interacts with a sparse isotropic material, e.g., a gas, in the linear excitation regime is given in Sections 2.1.3 and 2.1.4, which closely follows the Feynman Lectures on Physics [1, chapter 30, 31] but where I use the $e^{-i\omega t}$ convention for the electric field instead of $e^{i\omega t}$. The refractive index and phase velocity concepts are explained in Section 2.1.5.

Section 2.2 discusses dispersion, the change of refractive index as a function of the frequency of light; group velocity, the speed at which a pulse travels; and slow light, the concept of a group velocity that is much lower than the speed of light in vacuum. The effects of strong dispersion and slow light are discussed in Section 2.2.1. The energy density of a pulse that propagates through a slow light material is distributed between the atoms and the electric field, and is investigated in Section 2.2.2.

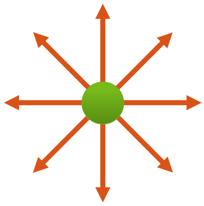

Figure 2.1. *A charge, shown as a green circle, has an electric field, shown as red arrows, associated with it, which points outwards if the charge is positive (as in the figure) and inwards if the charge is negative. The electric field strength decays as* $1/r^2$*, as seen in Equation (2.1).*

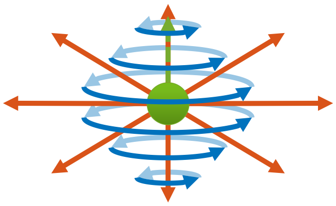

Figure 2.2. *A positive charge, shown in green, is moving with a constant velocity, indicated by the dashed green arrow. Its electric field components (red lines) perpendicular to the movement direction increase compared to the stationary charge seen in Figure 2.1 due to the Lorentz transformation of special relativity [2, chapter 26-3]. This transformation also generates magnetic field lines, shown in blue.*

The refractive index is once more derived in Section 2.3, this time for dense matter instead of gases, while still assuming an isotropic material and the linear excitation regime. Multiple resonances and local field effects are also discussed in this section.

Phonons, vibrations in dense matter, are qualitatively described in Section 2.4 using the framework presented in the previous sections.

While this chapter mostly discusses light-matter interaction from the light's point of view, Chapter 3 goes beyond the linear excitation regime and discusses what happens when the light significantly excites an atom in the quantum picture.

2.1 Refractive index of a sparse material

The main goal of this chapter is to lay the groundwork for the following chapters, but there is much more that can be understood using the knowledge presented here. For example, on a hot summer day you can sometimes see mirror-like puddles on the ground, but as soon as you get closer, they disappear, and when looking above a flame or candle, the view seem distorted. Effects such as these are due to light traveling at different speeds in different materials. More precisely in these two cases, the speed depends on the air temperature or density. We call the ratio of the speed of light in vacuum to the speed in matter the refractive index, and the origin of this is discussed in the following sections.

2.1.1 Radiation induced by an accelerating charge

A stationary point charge has a radial electric field associated with it according to Coulomb's Law [2, chapter 4-2], see Figure 2.1 and the equation below.

$$\mathbf{E}(r) = \frac{1}{4\pi\epsilon_0}\frac{q}{r^2}\mathbf{e}_r \tag{2.1}$$

where ϵ_0 is the vacuum permittivity, q is the charge, r is the distance measured from the charge, and $\mathbf{e}_r$ is a unit vector that points radially outward.

A charge moving with constant velocity has similar electric field lines, but the components perpendicular to the propagation direction are increased due to the Lorentz transformation of special relativity [2, chapter 26-3], as seen in the red lines of Figure 2.2. This transformation also creates a transverse magnetic field, which can be seen in the blue lines, but for now it is disregarded.

When a charge is quickly accelerated from stationary to some velocity it causes changes in the field lines, but they propagate at the speed of light, thus creating an outward moving spherical shell beyond which the field lines still follow Coulomb's Law from the original position, and inside which the field lines are as in Figure 2.2, i.e., following the charge that now moves with constant velocity [7]. Since the field cannot be discontinuous in the free space surrounding the charge, the lines within this shell look approximately as in Figure 2.3(a).

Even from this simple picture, you can draw some remarkable conclusions. First, in the limit of an infinitesimal shell thickness, and thus a very small acceleration, the electric field within the spherical shell is perpendicular to the propagation direction of the shell that radiates outwards, as illustrated in the dashed box that shows a more detailed view of the field within the shell. This agrees with the linear polarization you would expect from an accelerating charge in one dimension. Second, these transverse segments extend the field lines by a factor $r \sin\theta$, where θ is the polar angle that is zero at the top of the figure. This suggests that the long-range radial dependence is no longer the $1/r^2$ from Equation (2.1), but instead $1/r$, such that the electric field induced by accelerating the charge propagates much farther than the normal Coulomb field. Since the intensity of a wave is proportional to the electric field squared, this shell contains a fixed amount of energy that is carried away from the charge (energy $= I{\cdot}A \propto E^2{\cdot}A \propto 1/r^2{\cdot}r^2 =$ constant, where I is the intensity and A is the area over which the intensity is spread, i.e., the surface area of a sphere. Third, similar arguments can be made for the magnetic field lines shown in Figure 2.2, and the strengths of both the electric and magnetic fields induced are proportional to the magnitude of the acceleration, since a larger acceleration shifts the field lines inside more than those beyond the shell. In summary, accelerating a charge a relatively small amount creates a shell of transverse electromagnetic radiation proportional to the retarded acceleration and decays as $1/r$ such that it carries a constant energy away from the charge. [7]

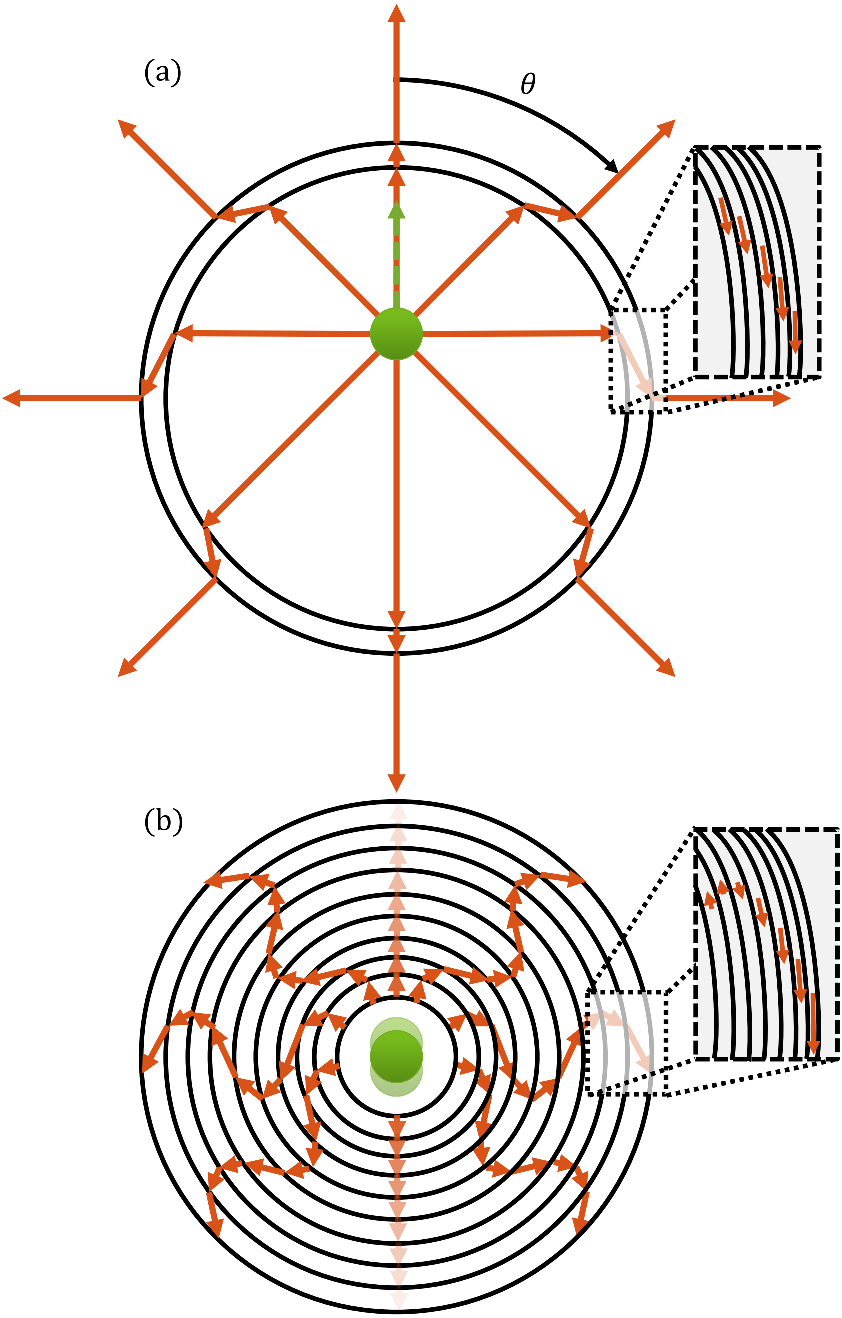

Figure 2.3. *(a) A positive charge (green circle) has rapidly accelerated from stationary to some finite velocity (dashed green arrow). This acceleration forms a spherical shell, denoted by the two black circles, that expand outwards at the speed of light. Beyond this shell, the red electric field lines originate from the original position, whereas inside it, the field lines move with the charge, as in Figure 2.2. In the limit of an infinitesimal shell thickness, the field lines within the shell are orthogonal to the radial direction and connect the internal and external field lines. (b) The charge oscillates back and forth, which generates a similar oscillating behavior for the electric field.*

Before we discuss what makes the charge accelerate in the first place, it is useful to consider a particular acceleration pattern, i.e., an oscillation where the particle is moving back and forth on a line in a sinusoidal manner. The single shell is now replaced by several shells stacked after one another, as seen in Figure 2.3(b). Each shell has fields that are proportional to the retarded acceleration. Since the charge accelerates back and forth, the fields also oscillate at the same frequency. This is called dipole radiation. Just as in the single shell case, the fields have an amplitude with a polar angle dependence of $\sin\theta$ and still exhibit rotational symmetry around the azimuthal angle, as seen in Figure 2.4.

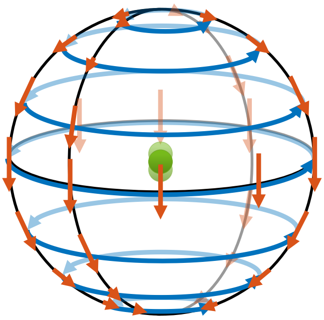

Figure 2.4. *An oscillating charge (green circle) generates a dipole radiation pattern, as seen in the red electric and blue magnetic field lines. The electromagnetic radiation decay as* $1/r$*, exhibits a* $\sin\theta$ *behavior, and is rotationally symmetrical around* ϕ*, the azimuthal angle. The black lines denote the spherical shell that contains the field lines and radiates outwards at the speed of light.*

The results of this section are directly embedded in Maxwell's equations [2, chapter 4-1], where Coulomb's Law is the static case of Gauss's Law for a point charge and where a moving charge, i.e., a current, is related to a magnetic field. Furthermore, a changing electric field induces a magnetic field and vice versa, which correlates perfectly with our results of transverse electromagnetic fields that propagate further than the normal Coulomb field.

The following sections use the concepts presented here to describe how light interacts with a single atom and a plane of atoms, as well as why it seems to travel slower when propagating through materials.

2.1.2 Atom-swing analogy

When light interacts with a material, it shakes the electrons in the atoms that make up the material, causing them to oscillate with the frequency of the incoming field and send out their own radiation, as described in Section 2.1.1. Since the electrons are negatively charged and the nucleus of the atom is positive, a restoring force that tries to bring the electrons back to their original position exists. Energy loss in the form of, e.g., heat or sound can also be present.

This section goes through an analogy to the system described above. A swing plays the part of the electron, and a person steering the swing through the ropes acts as the light that drives it. The nucleus in this analogy is the stationary swing set that is too heavy to move, and gravity is the restoring force trying to drive the swing back to its lowest point. Air resistance and friction slow down the swing as it moves, causing it to lose energy.

As long as the material is sparse, such as a gas, and we are in the linear regime, i.e., the electric field does not substantially alter the excitation of the electron through the interaction, the mathematical treatment of light that interacts with an atom is the same as for the swing system [1, chapter 31-2]. Thus, it is enlightening to study how a swing behaves in different situations since it is directly transferable to how light interacts with electrons.

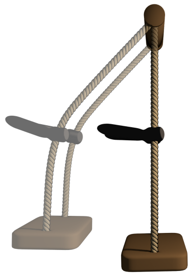

Figure 2.5. *A swing driven at a low frequency; it is in phase (0 degrees) with the hands.*

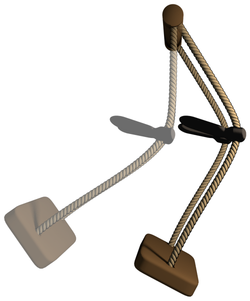

Figure 2.6. *A swing driven at resonance frequency; it is 90 degrees after the hands.*

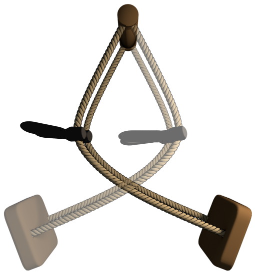

Figure 2.7. *A swing driven at a high frequency; it is opposite in phase (180 degrees) compared to the hands.*

If a swing is pulled back and released, it oscillates back and forth with one frequency that we call the resonance frequency. However, the swing can oscillate at other frequencies if the person steering it holds on to the ropes.

When the swing moves back and forth very slowly in this manner, i.e., with a frequency much lower than the resonance frequency, it moves in phase with the person who steers it. There is a 0 degree phase shift between the swing and the person's hands, as shown in Figure 2.5.

If the swing is driven at its resonance frequency instead, as shown in Figure 2.6, it is a quarter of an oscillation behind the person, i.e., 90 degrees after in phase.

If you oscillate the swing at a frequency much higher than its resonance, it behaves as in Figure 2.7, i.e., being completely out of phase with the driving hands (180 degree phase shift).

The next section offers a mathematical treatment of how light interacts with an atom and causes it to send out its own radiation, which is directly related to the swing described here. The phase relation of the induced electric field that originates from the electron compared to the incoming field is the same as the phase relations explained above for our more intuitive experiments with the swing.

2.1.3 Phase relation between an incoming field and the induced radiation

The system that we analyze in this section can be seen in Figure 2.8. An incoming plane wave, $\mathbf{E}_{\text{in}}(t, \mathbf{r}) = E_0 \mathbf{e}_x e^{-i\omega(t-z/c)}$, traveling in the z direction with a polarization along x and a frequency ω reaches an atom located at $\mathbf{r} = 0$ with a single resonance frequency ω_0. A complex notation is used for the electric field, where it is understood that the field consists only of the real part of $\mathbf{E}_{\text{in}}(t, \mathbf{r})$. Similarly to a swing that oscillates much stronger if driven at its resonance frequency, atoms have transitions, i.e., certain resonance frequencies at which the incoming field is able to excite an atom to another energy state. This is further discussed in Section 3.1.1.

Newton's second law [1, chapter 9-1] can be used to relate the acceleration, $\ddot{x}(t) = \frac{d^2x(t)}{dt^2}$, of the electron with the forces acting on it, $F_{\text{tot}}(t)$. These forces are the restoring harmonic oscillator force proportional to $x(t)$; the damping force proportional to $\dot{x}(t)$; and the force exerted by the light, $F_{\text{l}}(t)$, i.e., the Lorentz force [2, chapter 13-1].

$$m_e \ddot{x}(t) = F_{\text{tot}}(t) = -m_e \omega_0^2 x(t) - m_e \gamma \dot{x}(t) + F_{\text{l}}(t) \tag{2.2}$$

where m_e is the mass of the electron and $\tau = 1/\gamma > 0$ is the exponential damping time. The full Lorentz force is [2, chapter

13-1];

$$\mathbf{F}_{\text{Lorentz}}(t) = q_e(\mathbf{E}_{\text{in}}(t) + \mathbf{v}(t) \times \mathbf{B}_{\text{in}}(t)) \tag{2.3}$$

where $q_e < 0$ and $\mathbf{v}$ are the charge and velocity of the electron, respectively, and $\mathbf{B}_{\text{in}}$ is the magnetic field associated with the incoming electromagnetic wave. Assuming a low electron velocity compared with the speed of light, the magnetic term can be neglected, remembering that $|\mathbf{B}_{\text{in}}| = |\mathbf{E}_{\text{in}}|/c$ for a traveling wave. Assuming the electron is located at $z = 0$, the force in the x-direction can be written as

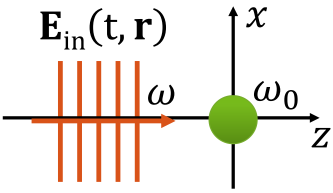

Figure 2.8. *An atom located at* $\mathbf{r} = 0$ *with resonance frequency* ω_0 *interacts with an incoming plane wave with frequency* ω *that is traveling along the* z*-direction with a polarization along* x.

$$F_1(t) = q_e E_0 e^{-i\omega t} \tag{2.4}$$

Solving Equation (2.2) for $x(t)$ yields

$$x(t) = x_0 e^{-i\omega t} = \frac{q_e E_0}{m_e(\omega_0^2 - \omega^2 - i\omega\gamma)} e^{-i\omega t} \tag{2.5}$$

Maxwell's equations says that any accelerating charge sends out its own field [2, chapter 18-4], as explained in Section 2.1.1. In this case where the electron moves in an oscillatory pattern, we can write a simple expression for the induced radiation, $\mathbf{E}_{\text{rad}}(t, \mathbf{r})$, at position $\mathbf{r}$, produced by an electron located at $\mathbf{r} = 0$, as long as we look far off in the z-direction, i.e., $|\mathbf{r}| = r \approx z$;

$$\mathbf{E}_{\text{rad}}(t, \mathbf{r}) \approx \frac{-q_e}{4\pi\epsilon_0 c^2 r} \mathbf{e}_x \ddot{x}(t - r/c) \tag{2.6}$$

In reality the electric field produced has a polarization that is orthogonal to the propagation direction. Thus, if $r \not\approx z$ the polarization would no longer be only along $\mathbf{e}_x$, as explained in Section 2.1.1 and shown in Figure 2.4.

Using the expression for the electron position given in Equation (2.5), the field produced by the oscillating electron can be written as

$$\begin{aligned} \mathbf{E}_{\text{rad}}(t, \mathbf{r}) &\approx \frac{q_e \omega^2}{4\pi\epsilon_0 c^2 r} x_0 \mathbf{e}_x e^{-i\omega(t - r/c)} \\ &\approx \frac{q_e^2 \omega^2}{4\pi\epsilon_0 c^2 r m_e} \frac{1}{\omega_0^2 - \omega^2 - i\omega\gamma} \mathbf{E}_{\text{in}}(t, \mathbf{r}) \end{aligned} \tag{2.7}$$

where the second approximation uses $r \approx z$ to write the induced field as the incoming field multiplied by two factors. Since the first factor is just a positive number, the middle part determines the phase relation of the induced radiation, $\mathbf{E}_{\text{rad}}(t, \mathbf{r})$, and the original field, $\mathbf{E}_{\text{in}}(t, \mathbf{r})$. Thus, the induced field oscillates at the same frequency ω as the driving field but with a phase relation determined by $\frac{1}{\omega_0^2 - \omega^2 - i\omega\gamma}$.

Just as for the swing explained in Section 2.1.2, we can see that if $\omega \ll \omega_0$, this factor is positive and real such that $\mathbf{E}_{\text{rad}}(t, \mathbf{r})$

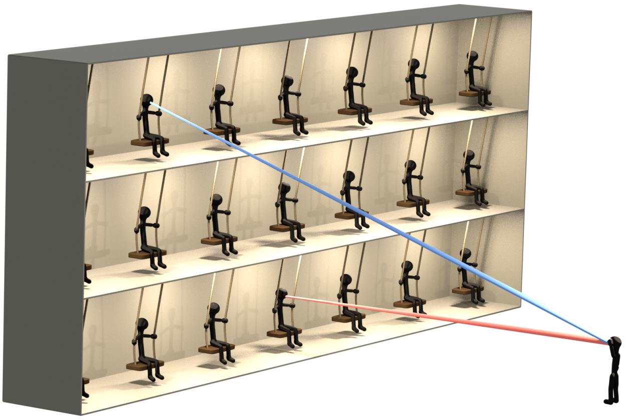

Figure 2.9. *In an analogy to the induced electric field radiated by a plane of oscillating charges, a house filled with people on swings that oscillates in phase where each person shouts simultaneously as they reach the most forward position is examined. For a person standing right in front of the building, the sound from the closest person on a swing traveling along the red line arrives earlier than the sound from a person sitting farther away, such as along the blue line. Thus, the sound experienced by the person in front of the house is an elongated sound with a center that is delayed compared to the sound arriving along the red line.*

oscillates in phase (0 degree phase shift) compared with $\mathbf{E}_{\text{in}}(t, \mathbf{r})$. Similarly, if $\omega = \omega_0$, the fraction is positive and purely imaginary ($\frac{1}{-i} = i$), which corresponds to being 90 degrees after in phase. Lastly, if $\omega \gg \omega_0$, it is negative and real, yielding a 180 degree phase shift between the two fields. Note that γ is assumed to be much lower than ω and ω_0.

Now that we know how light interacts with a single atom, the next step in understanding refractive index is to continue onto a thin plane of atoms, which is the topic of the next section.

2.1.4 Induced radiation from a plane of charges

To explain why light refracts and slows down when propagating through matter, the contribution from one electron to the field is not enough. Instead you have to evaluate the electric field contribution for a plane of electrons, all emitting their own light due to the acceleration induced by the incoming plane wave.

Before continuing with the mathematical treatment of the electrons I will explain the effects using the analogy with the swings.

Imagine a house with several floors filled with swings that all oscillate in phase, as seen in Figure 2.9. Now each person sitting on a swing shouts as they reach their most forward position. Since sound travels at a finite speed (as does light), the sound from the person on the closest swing reaches a person standing in front of the house first; see the red line in the figure. A while later, the sound from a person sitting further away arrives, for example along the blue line in the figure. The collection of sounds from everyone on the swings is an elongated sound whose center is delayed compared to the sound from the person on the closest swing. From this analogy, we can expect the electric field contribution from all electrons to be delayed (later in phase) compared to the field from the closest electron.

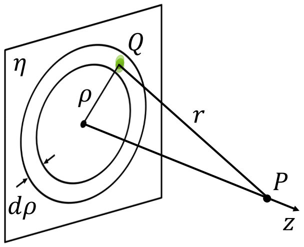

Figure 2.10. *A plane of oscillating charges with a surface density of η generates a field at P that can be evaluated by integrating over infinitesimal rings of thickness $d\rho$ at a distance ρ from the z axis.*

With this information in mind, we can continue with the treatment of light that interacts with electrons in an infinite plane, as in Figure 2.10. The electric field at point P from a charge located at Q is given in the first line of Equation (2.7). Since this depends only on the distance r between P and Q, the total induced field can be evaluated as the integral over infinitesimal rings of surface area $2\pi\rho d\rho$ with the number of charges per unit area equal to η. [1, chapter 30-7]

For symmetry reasons, the only polarization that can be nonzero is along the direction the electrons move in, i.e., the x-direction given by the incoming electric field polarization.

$$\mathbf{E}_{\text{rad,tot}}(t, \mathbf{r}) \approx \int_{\rho=0}^{\rho=\infty} \frac{q_e\omega^2}{4\pi\epsilon_0 c^2} \frac{x_0 \mathbf{e}_x e^{-i\omega(t-r/c)}}{r} \eta 2\pi\rho d\rho \tag{2.8}$$

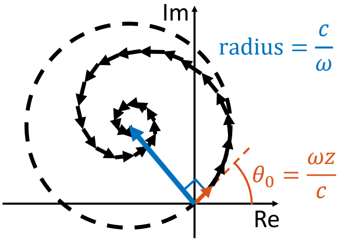

Figure 2.11. *The integral in Equation (2.9) can be interpreted as the sum of infinitesimal arrows with the same phase angle relation, starting at an angle of $\theta_0 = \frac{\omega z}{c}$. For the integral in question, these arrows follow the dashed circle indefinitely. However, in the physically more correct description, the arrows decrease in length and therefore spiral inwards, yielding the solution denoted by the blue arrow.*

Note that the expression is only approximately correct, since we made the assumption that $r \approx z$ in Equation (2.6) before arriving at Equation (2.7).

With the Pythagorean theorem $r^2 = \rho^2 + z^2$, you can eliminate the variable ρ from the integral ($\rho d\rho = r dr$). The new limits are from $r = z$ to $r = \infty$.

$$\mathbf{E}_{\text{rad,tot}}(t, \mathbf{r}) = \frac{q_e\omega^2 \eta x_0 \mathbf{e}_x e^{-i\omega t}}{2\epsilon_0 c^2} \int_{r=z}^{r=\infty} e^{i\omega r/c} dr \tag{2.9}$$

The solution to the integral is $\frac{c}{i\omega}(e^{i\omega\infty/c} - e^{i\omega z/c})$, the first term of which is undefined mathematically.

Returning to the physics of the problem, the integral is just the sum of infinitesimal arrows, all with a slight phase angle difference of $\Delta\theta = \frac{\omega\Delta r}{c}$. For the integral above, these arrows form a perfect circle, which is why it does not have a finite answer, see the dashed circle in Figure 2.11. However, Equation (2.7) was only approximately true for distances $r \approx z$, and this is no longer the case when $\rho \to \infty$. Thus, the electric field contribution from charges far out in the plane diminishes and eventually reaches zero, as in Figure 2.4 for steep θ angles, which results in a spiraling that tends towards the center of the circle as the arrows decrease in length, giving the integral its value of $-\frac{c}{i\omega}e^{i\omega z/c}$, see the blue arrow in Figure 2.11. [1, chapter 30-7]

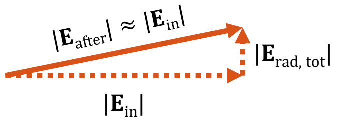

Figure 2.12. *When adding the induced field, $\mathbf{E}_{rad,tot}$, to the incoming field, $\mathbf{E}_{in}$, the resulting field, $\mathbf{E}_{after}$, differs mostly in phase compared to the incoming field.*

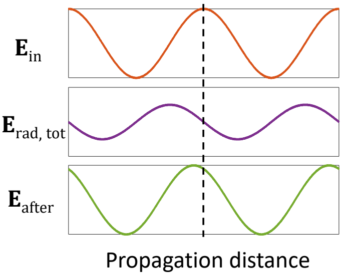

Figure 2.13. *Compared to the incoming field, $\mathbf{E}_{in}$, the induced field from a thin plane of charges, $\mathbf{E}_{rad,tot}$, is 90 degrees later in phase and has much lower amplitude, exaggerated here for visibility. The resulting field after propagating through the thin plane is therefore a small phase delay, as seen when comparing $\mathbf{E}_{after}$ with $\mathbf{E}_{in}$.*

Finally, the total electric field radiated by the oscillating charges in a plane of atoms driven by an incoming plane wave is

$$\mathbf{E}_{\text{rad,tot}}(t, \mathbf{r}) = \frac{q_e^2 \eta}{2\epsilon_0 c m_e} \frac{i\omega}{\omega_0^2 - \omega^2 - i\omega\gamma} \mathbf{E}_{\text{in}}(t, \mathbf{r}) \tag{2.10}$$

Once more, we obtain a relation between the induced field and the incoming field. Two important notes can be made. First, the electric field no longer decreases as a function of r. Second, the phase relations with the incoming field are the same as before except for an additional 90 degree after in phase due to the extra i in the numerator.

The next section ties up the knowledge acquired so far in order to finally explain the refractive index.

2.1.5 Refractive index and phase velocity

Imagine a plane wave that propagates through air, shaking the electrons in the molecules that have resonances at ultraviolet and higher frequencies, amongst other. For visible incoming light, we therefore have $\omega \ll \omega_0$. The field produced by the oscillating charges in a thin plane of air is 90 degrees (i) after in phase compared to the incoming field, as explained in Section 2.1.4 and seen in Equation (2.10).

The total electric field after the plane is the sum of the two contributions: $\mathbf{E}_{\text{after}} = \mathbf{E}_{\text{in}} + \mathbf{E}_{\text{rad,tot}}$. Currently we consider only sparse materials like gases. Thus, η is small, and as a result, $|\mathbf{E}_{\text{rad,tot}}| \ll |\mathbf{E}_{\text{in}}|$. Thus, the total field after the plane has roughly the same magnitude as the incoming field but slightly rotated in phase, as seen in Figure 2.12. The overall effect of passing through a thin slice of air, compared to vacuum where no extra field is induced, is therefore a phase shift, as seen in Figure 2.13. The field looks as though it arrives later. By stacking several such planes after one another, the light appears to travel slower when propagating through the material. It travels at the phase velocity, v_p, which is related to the refractive index by $n = c/v_p$.

Before continuing to a discussion of the implications of light slowing down in matter, we should find an expression for the refractive index.

Once more, we examine the problem of a plane wave incoming perpendicularly towards a thin plane of thickness Δz, made of a material with refractive index n. According to our results above, this should lead to a phase shift or an equivalent time delay. Instead of taking time $\Delta z/c$ to travel through the thickness of the plane, it takes $n\Delta z/c$, i.e., an extra time of $\Delta t = (n-1)\Delta z/c$. Thus, if the field before the plane was described as $\mathbf{E}_{\text{in}}(t,\mathbf{r}) = E_0\mathbf{e}_x e^{-i\omega(t-z/c)}$, after the plane, it is

$$\begin{aligned}
\mathbf{E}_{\text{after}}(t,\mathbf{r}) &= E_0\mathbf{e}_x e^{-i\omega(t-\Delta t-z/c)} \\
&= e^{i\omega(n-1)\Delta z/c} E_0\mathbf{e}_x e^{-i\omega(t-z/c)} \\
&\approx \left(1+\frac{i\omega(n-1)\Delta z}{c}\right) E_0\mathbf{e}_x e^{-i\omega(t-z/c)} \\
&= \mathbf{E}_{\text{in}}(t,\mathbf{r}) + \mathbf{E}_{\text{rad, tot}}(t,\mathbf{r})
\end{aligned} \tag{2.11}$$

where the approximation on the third line is made by assuming that Δz is small and therefore $e^{i\omega(n-1)\Delta z/c} \approx 1 + i\omega(n-1)\Delta z/c$. The field that causes the time delay is $\mathbf{E}_{\text{rad, tot}}$ in Equation (2.10), obtained in Section 2.1.4, which yields the fourth line of the equation. Since the surface density of charges, η, is the volume charge density N of the material multiplied by the thickness of the plane Δz, we can, after simple algebra, write out an expression for the refractive index [1, chapter 31-2].

$$n_{\text{sparse}} \approx 1 + \frac{1}{2}\frac{q_e^2 N}{\epsilon_0 m_e}\frac{1}{\omega_0^2 - \omega^2 - i\omega\gamma} \tag{2.12}$$

The approximation sign and the subscript remind us that our expression for the refractive index is valid only for a sparse media such as a gas. The reason is that we have assumed that only the incoming electric field shakes the electrons, whereas in reality the total field, including the field induced by other charges, can cause electrons to oscillate. In sparse materials, the field induced by other charges is smaller than the incoming field which is why our approximation is valid for cases where $n \approx 1$. Later in Section 2.3 a more correct expression that also works for dense matter is derived.

As in our example with air at the beginning of this section, if $\omega \ll \omega_0$, we obtain a positive contribution to the refractive index, i.e., a delay in time of the propagating field that is equivalent to a reduced phase velocity, $v_p = c/n$.

If the incoming light is instead much closer to resonance, $\omega \approx \omega_0$, we can see from Equation (2.10) that the overall phase shift of the induced field is 180 degrees, i.e., out of phase, such that it cancels a part of the incoming field. The light energy is absorbed in the oscillation of the electrons, just as a swing goes higher if driven at its resonance frequency by efficiently taking energy from the person pushing it. In Equation (2.12), $\omega \approx \omega_0$ yields a positive imaginary contribution to the refractive index, which, if inserted in the second line of Equation (2.11), yields

$$\begin{aligned}
\mathbf{E}_{\text{after}}(t,\mathbf{r}) &= \exp\left[-\frac{q_e^2 N}{2\epsilon_0 m_e \gamma c}\Delta z\right]\mathbf{E}_{\text{in}}(t,\mathbf{r}) \\
&= \exp\left[-\frac{\alpha}{2}\Delta z\right]\mathbf{E}_{\text{in}}(t,\mathbf{r})
\end{aligned} \tag{2.13}$$

where we have defined the absorption coefficient α with dimension $[\text{m}^{-1}]$. In conclusion, if the incoming light is resonant with an atomic transition, the electric field amplitude decays exponentially when traveling through the material. Furthermore, the energy lost from the field is gained by the atom, as discussed further in Section 3.2.

The refractive index can be written as a real and imaginary part, $n = n_{\mathrm{Re}} + in_{\mathrm{Im}}$. A schematic graph of how these parts change as a function of frequency can be seen in Figure 2.14. A strong absorption, positive imaginary refractive index, is only obtained close to resonance.

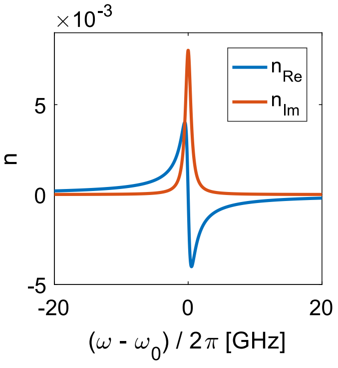

Figure 2.14. *A schematic graph of how the real (blue) and imaginary (red) refractive index change as a function of frequency over a resonance located at ω_0. Note that a positive imaginary part corresponds to absorption.*

We have finally found the reasons why light slows down and sometimes is absorbed during propagation in a material. Without going into detail, light that passes between materials with different refractive indices bends or refracts and can be summed up by Snell's Law [1, chapter 26-2];

$$n_1 \sin\theta_1 = n_2 \sin\theta_2 \tag{2.14}$$

where light travels from refractive index n_1 into n_2 with an incidence angle of θ_1 and refracts to an outgoing angle of θ_2, both measured from the normal to the interface.

From Equation (2.12), we see that the refractive index depends on the charge density N. Since the density of gases depends on temperature, so does the refractive index. The distortion above a candle is light bending back and forth, since the refractive index changes due to temperature changes in the air. The mirages on a road can be explained by light from the sky gradually bending due to a temperature gradient from the very hot road to the slightly cooler air and eventually propagating up to the beholder's eyes.

Using this knowledge, you can explain all kinds of effects. In the next section, we explore something exotic: slow light.

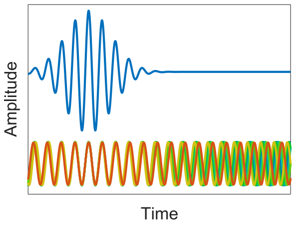

Figure 2.15. *The upper graph shows the electric field oscillations within a pulse of finite duration. The pulse can also be visualized with monochromatic waves, some of which are shown in the lower graph. When these components oscillate in phase, they give rise to the pulse, whereas they cancel each other out when they oscillate out of phase.*

2.2 Dispersion, group velocity, and slow light

In Figure 2.14, you can see how the complex refractive index behaves as a function of frequency when it crosses a resonance. The phase velocity thus changes as a function of frequency, referred to as dispersion. In particular, when the refractive index increases with frequency, it is called normal dispersion. As explained above, light with a specific frequency travels at its phase velocity, $v_p(\omega)$.

When thinking about a light pulse with a finite duration, you can imagine it as a distribution of single frequency light waves that propagate together. The pulse is created through interference of these different frequencies, which at some places is constructive, giving rise to a strong amplitude, whereas it in other places is destructive, i.e., canceling each other out, as in Figure 2.15.

In a vacuum, all frequency components move at the speed of light and therefore travel together. However, in a material with dispersion, the waves shift relative to one another due to the differences in phase velocities. Thus, the speed at which a pulse travels, i.e., the speed at which the place where the individual components constructively interfere moves, can be very different from the phase velocity. It is called the group velocity, $v_g(\omega)$. The following sections examine the slow light effect in which the group velocity is much lower than the phase velocity and the speed of light in vacuum. This effect occurs when light propagates through a medium with strong normal dispersion.

2.2.1 Slow light

To explain the slow light effect, I first present an analogy that uses combs. The different frequency components of a light pulse are each represented by a comb, where the tooth separation is related to the frequency, an example of which can be seen in Figure 2.16(a).

That a light pulse is built from several frequencies is illustrated by several combs stacked behind one another. The location of the pulse is where you can see through all the combs, see Figure 2.16(b), where it is also indicated by a blue arrow.

Two yellow teeth are used to track how far the individual combs move, i.e., the phase velocity, whereas how fast the place where you can see through all combs moves corresponds to the group velocity. At the beginning, the yellow markers are in the same place as the pulse.

In Figure 2.16(c), no dispersion is present and all combs move exactly the same amount. The phase and group velocities are the same, since you can see through the combs at the same place as where the yellow teeth are located.

In the case of strong normal dispersion shown in Figure 2.16(d), the combs move slightly differently, as shown by the small spread of the yellow markers. Note, however, that this difference is small compared to the absolute speed, since all the yellow teeth almost line up with those in Figure 2.16(c). Finally, you can see that the group velocity is much lower than the phase velocity, as the part where you see through the combs have only traveled roughly half the distance as the individual combs.

This is the explanation of slow light. The individual frequency components that make up a light pulse travel at slightly different velocities due to dispersion, but the speed at which the constructive interference moves is greatly reduced. Later in Sections 5.3 and 5.4, and Papers **III** and **IV**, slow light is used to reduce the group velocity of pulses to about $v_g = 1.5$ km/s, which is 200 000 times slower than the speed of light in vacuum, $c \approx 300\,000$ km/s, and slower than the speed of sound in the material.

The mathematical expression for the group velocity is

$$v_g(\omega) = c/n_g(\omega) \qquad n_g(\omega) = n(\omega) + \omega\frac{\partial n(\omega)}{\partial \omega} \tag{2.15}$$

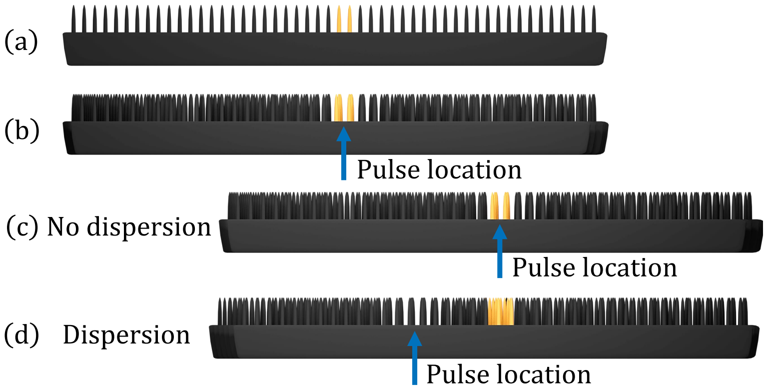

Figure 2.16. *A slow light analogy using combs. (a) Each comb has a frequency, as represented by the distance between its teeth. (b) A light pulse is built by stacking combs with slightly different frequencies after one another, as visualized by being able to see through the combs, also shown by the blue arrows in the figure. The yellow teeth are used as markers to show how far each comb moves. (c) In the case with no dispersion, all combs move exactly the same amount, which leads to a group velocity equal to the phase velocity. (d) In the case of strong normal dispersion, the combs move slightly differently, which leads to a group velocity that is much lower than the phase velocity.*

where n_g is the group refractive index. If a material has a steep normal dispersion curve ($\omega\frac{\partial n}{\partial \omega} \gg n$), the group velocity can be much lower than the speed of light in vacuum, as explained above.

2.2.2 Energy temporarily stored in the medium

When light is slowed down by passing through a material, some of its energy is temporarily stored in the atoms. The more energy that is stored compared to the total energy of the pulse, the slower it travels.

In Papers **III** and **IV** slow light is discussed and simulated for rare-earth-ion-doped crystals, the topic of Chapter 4. Thus, it is advantageous to split the atoms of the material into two parts. The first part is called the host, which includes all contributions to the refractive index from the crystal host atoms and is assumed not to contribute to the dispersion of the material, i.e., it is a constant addition to the refractive index for all relevant frequencies. The second part consists of the dopant ions, which this section refers to as resonant centers. This part heavily influences the dispersion for frequencies close to resonance. As a result, the energy density of the system can be split into three parts, U_{host}, U_{res}, and U_{vac}, for the host, resonant centers, and energy density of the electromagnetic field, which is the same in the crystal as in a vacuum.

The energy flow per cross section and time of a pulse traveling in a vacuum is cU_{vac}, where c is the speed of light in vacuum. When inside a material, such as the crystal described above, the speed at which the pulse travels is reduced to the group velocity, v_g [8, 9]. However, the energy flow into the crystal from a vacuum must be the same as the flow inside the material (light + host + resonant centers):

$$\begin{aligned} cU_{\text{vac}} &= v_g(U_{\text{vac}} + U_{\text{host}} + U_{\text{res}}) \\ v_g &= \frac{c}{1 + \frac{U_{\text{host}}+U_{\text{res}}}{U_{\text{vac}}}} \end{aligned} \tag{2.16}$$

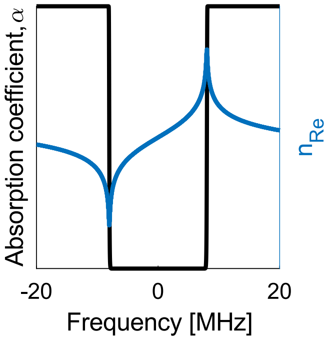

Figure 2.17. *A schematic view of a spectral hole (black) and the real part of the refractive index curve (blue) that it generates. There is a strong normal dispersion inside the transmission window, which slows down any light propagating through it.*

For frequencies far from the absorption of the resonant centers $U_{\text{res}} = 0$ and since we assume that the host does not have any dispersion, the group velocity is equal to the phase velocity, $v_g = v_p = c/n$. Thus, the phase refractive index n is

$$n = 1 + \frac{U_{\text{host}}}{U_{\text{vac}}} \tag{2.17}$$

i.e., 1 + the energy density in the host compared to the energy density of the light wave inside the crystal, which is the same as for the light in a vacuum.

On the other hand, a strong slow light effect can be achieved when the resonant centers make up a spectral hole, i.e., a transmission window, in an otherwise strongly absorbing region, see Figure 2.17. In such a case, where the energy is stored mostly in the resonant centers, an approximate expression of the group velocity can be used [10–12];

$$v_g \approx \frac{2\pi\Gamma}{\alpha} \tag{2.18}$$

where Γ is the frequency width of the transmission window and α is the absorption coefficient outside the hole.

2.3 Refractive index of a dense material

The experiments performed in this thesis are based on light that propagates in solids, not gases. Thus, it is useful to extend the framework in Section 2.1 to be valid for dense matter as well. Note, however, that the intuitive picture is still correct. The only addition needed is to let the fields induced by the atoms interact with other atoms. [2, chapter 32]

Still using the harmonic oscillator model from Section 2.1.3 for the movement of an electron, we arrive at Equation (2.5). This time, however, we do not directly relate it to an electric field as in Equation (2.6). Instead we calculate the induced dipole moment of all atoms, denoted by the polarization of the material, $P = Nq_e x$, where N is the number of atoms per unit volume.

$$\mathbf{P}(t,\mathbf{r}) = \frac{Nq_e^2}{m_e(\omega_0^2 - \omega^2 - i\omega\gamma)}\mathbf{E}_{\text{local}}(t,\mathbf{r}) = N\alpha_{\text{pol}}(\omega)\epsilon_0\mathbf{E}_{\text{local}}(t,\mathbf{r}) \tag{2.19}$$

where $\alpha_{\text{pol}}(\omega)$ is the atomic polarizability (not to be confused with the absorption coefficient introduced in Sections 2.1.5 and 2.2.2), and $\mathbf{E}_{\text{local}}$ is the local electric field felt by the atoms, which is related to the average field in the crystal, $\mathbf{E}_{\text{avg}}$, by $\mathbf{E}_{\text{local}} = \mathbf{E}_{\text{avg}} + \frac{\mathbf{P}}{3\epsilon_0}$ [2, chapter 11-4]. For the sparse description used in Section 2.1, $\mathbf{E}_{\text{local}} = \mathbf{E}_{\text{avg}}$ since the effect of atoms interacting with the induced fields of other atoms was neglected.

Writing the induced polarization as a function of $\mathbf{E}_{\text{avg}}$ yields:

$$\mathbf{P}(t,\mathbf{r}) = \frac{N\alpha_{\text{pol}}(\omega)}{1-(N\alpha_{\text{pol}}(\omega)/3)}\epsilon_0\mathbf{E}_{\text{avg}}(t,\mathbf{r}) \tag{2.20}$$

Furthermore, real materials have more than one resonance frequency with different damping factors, γ_k, and transition strengths, f_k, which are numbers in the order of 1 that take into consideration the fact that some transitions are more difficult to excite. Thus, we can add up the contribution from each transition:

$$\alpha_{\text{pol}}(\omega) = \frac{q_e^2}{\epsilon_0 m_e}\sum_k \frac{f_k}{\omega_{0k}^2 - \omega^2 - i\omega\gamma_k} \tag{2.21}$$

In order to relate this to the refractive index, you need to study Maxwell's equations, which can be written as [2, chapter 18-1];

$$\begin{aligned} \nabla\cdot\mathbf{E} &= \frac{\rho}{\epsilon_0} \\ \nabla\cdot\mathbf{B} &= 0 \\ \nabla\times\mathbf{E} &= -\frac{\partial\mathbf{B}}{\partial t} \\ c^2\nabla\times\mathbf{B} &= \left(\frac{\mathbf{j}}{\epsilon_0} + \frac{\partial\mathbf{E}}{\partial t}\right) \end{aligned} \tag{2.22}$$

where ρ is the total charge density, $\mathbf{j}$ is the total current, and $\nabla = \left(\frac{\partial}{\partial x}, \frac{\partial}{\partial y}, \frac{\partial}{\partial z}\right)$ is the nabla operator.

The charge density can be split up into two parts, $\rho = \rho_{\text{pol}} + \rho_{\text{other}}$. ρ_{pol} describes the charges in the material that have been displaced due to the electric field, and ρ_{other} represents all other charges. Similarly, $\mathbf{j} = \mathbf{j}_{\text{pol}} + \mathbf{j}_{\text{other}}$. They can be related to the material polarization through $\rho_{\text{pol}} = -\nabla\cdot\mathbf{P}$ and $\mathbf{j}_{\text{pol}} = \frac{\partial\mathbf{P}}{\partial t}$.

When no other charges or currents except those induced in the material exist, Maxwell's equations can be rewritten as

$$\begin{aligned} \nabla \cdot \mathbf{E} &= -\frac{\nabla \cdot \mathbf{P}}{\epsilon_0} \\ \nabla \cdot \mathbf{B} &= 0 \\ \nabla \times \mathbf{E} &= -\frac{\partial \mathbf{B}}{\partial t} \\ c^2 \nabla \times \mathbf{B} &= \frac{\partial}{\partial t}\left(\frac{\mathbf{P}}{\epsilon_0} + \mathbf{E}\right) \end{aligned} \tag{2.23}$$

Assuming that the average electric field is polarized along x and propagates in the z-direction with a wave vector $k = \omega/v_p = n\omega/c$, i.e., $\mathbf{E}_{\mathrm{avg}}(t, \mathbf{r}) = E_0 \mathbf{e}_x e^{-i(\omega t - kz)}$, and assuming an isotropic material, we can use Equation (2.20) where both $\mathbf{E}_{\mathrm{avg}}$ and $\mathbf{P}$ have only an x component. Solving Maxwell's equations under these conditions, we arrive at the following expression that relates the electric field to the polarization of the material:

$$\begin{aligned} k^2 E_{\mathrm{avg}} &= \frac{\omega^2}{c^2} E_{\mathrm{avg}} + \frac{\omega^2}{\epsilon_0 c^2} P \\ k^2 &= \frac{\omega^2}{c^2}\left(1 + \frac{N\alpha_{\mathrm{pol}}(\omega)}{1 - (N\alpha_{\mathrm{pol}}(\omega)/3)}\right) \end{aligned} \tag{2.24}$$

The last expression can be related to the refractive index through $n = ck/\omega$;

$$n^2 = 1 + \frac{N\alpha_{\mathrm{pol}}(\omega)}{1 - (N\alpha_{\mathrm{pol}}(\omega)/3)} \tag{2.25}$$

where an expression for the atomic polarizability can be found in Equation (2.21).

Note that for a sparse material where $N\alpha_{\mathrm{pol}}(\omega) \ll 1$ the second term in Equation (2.25) is small and $n \approx 1 + \frac{1}{2}N\alpha_{\mathrm{pol}}(\omega)$, which, if we only include one resonance frequency with strength $f_k = 1$, is the same expression that we arrived at in Section 2.1.5 and Equation (2.12) for a sparse material.

You should also be aware that the resonance frequencies, damping coefficients, and transition strengths are generally different for an atom in a solid compared to a free atom, since they are affected by other nearby atoms.

Because a solid can be made up of different atoms, you need to sum over the different densities N_j of the atoms, each with their own set of resonances, resulting in a collection of $\alpha_{\mathrm{pol,\,j}}(\omega)$. Including this in Equation (2.25) and writing it in another form known as the Clausius-Mossotti equation [2, chapter 32-3], you arrive at:

$$3\left(\frac{n^2 - 1}{n^2 + 2}\right) = \sum_j N_j \alpha_{\mathrm{pol,\,j}}(\omega) \tag{2.26}$$

We have finally obtained an expression for the refractive index that works for a dense isotropic material in the linear excitation regime. Even though we have only examined a simple model and the real case is a bit different, the overall idea and intuitive sense will help when discussing Papers **I-IV** in Chapter 5. In a more complex model, the transitions can also depend on the polarization of light. For example, some polarizers are made of materials for which electrons can easily oscillate and absorb light in one direction, but not perpendicular to it. Thus, light polarized along the second direction is transmitted through the polarizer. This also means that the index of refraction can vary for different polarizations and propagation directions, which is the case for a birefringent (or anisotropic) material.

2.4 Relation to phonons

This chapter has covered how light interacts with atoms in a way that makes the electrons oscillate, but our model can also describe how infrared radiation interacts with phonons, which essentially are just oscillations of atoms instead of electrons. For a simple vibration, the mathematical treatment is the same, only that ω_{0k} now represents a resonance in the crystalline structure.

As a side note, it is not only your eyes that can see electromagnetic radiation, your whole body is a sensor of heat radiation, which is part of the electromagnetic spectrum with lower frequencies than visible light.

CHAPTER 3

UNDERSTANDING THE QUANTUM MECHANICAL NATURE OF ATOMS

"... I think I can safely say that nobody understands quantum mechanics." - Richard Feynman [13].

This quote should be interpreted in the way that nobody understands quantum mechanics in terms of their common sense of reality. I write it here since quantum mechanics is a complex subject where not even leading physicists agree on everything. Some of the discussions I present in this chapter therefore only represent my own thoughts on the subject.

The quantum mechanical picture of a particle is introduced in Section 3.1, where I also compare it with classical physics to highlight the similarities and differences. A simple quantum system, the infinite well, is solved in Section 3.1.1 and the relationship between position and momentum in quantum mechanics is also discussed.

Section 3.2 returns to the light-matter interaction topic, this time focusing on the atom. A useful depiction of a two level quantum system is described in Section 3.2.1. Following this, Section 3.2.2 connects the superposition of an atom to the oscillation of a charge and the induced field it creates. Finally, Section 3.2.3 links the description of this chapter to the results of Chapter 2. These sections are especially important for the quantum computation results discussed in Chapter 7.

Two important time scales for an atom are described in Section 3.3, where Section 3.3.1 describes phase decay and coherence time, while Section 3.3.2 explains the decay of excitation and lifetime.

Finally, Section 3.4 describes the DC Stark effect, which is the shift of energy levels due to a static electric field, and is used in both Chapters 5 and 7.

3.1 Classical versus quantum picture

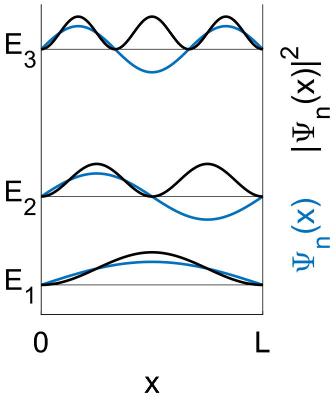

Figure 3.1. *Shows the three lowest energy states, $E_1 \rightarrow E_3$, for the infinite well discussed in Section 3.1.1. The wave functions, $\Psi_n(x)$, are shown in blue and the probability densities, $|\Psi_n(x)|^2$, in black.*

To describe quantum mechanics, I first go through an example of classical physics so that the similarities and differences can be seen more easily.

Imagine a football in the physical system of a field with two goals. At a specific time, the ball can be located at any position $\mathbf{r}$ with a momentum $\mathbf{p} = m\mathbf{v}$, where m and $\mathbf{v}$ are the ball's mass and velocity, respectively. In this non-relativistic example of classical physics, Newton's second law [1, chapter 9-1] applies and the acceleration is determined by the forces acting on the ball through:

$$\mathbf{F} = m\mathbf{a} \tag{3.1}$$

where $\mathbf{a}$ is the acceleration and $\mathbf{F}$ is the total resultant force.

Given that the physical system is already determined, for example the field is located on Earth with a gravitational constant of $g = 9.81\ \mathrm{m/s^2}$, normal air pressure, temperature, and a certain wind speed, the forces are explicitly determined by the system itself but depend on where the ball is positioned and how it travels, i.e., $\mathbf{r}$ and $\mathbf{p}$. Thus, $\mathbf{r}$, $\mathbf{p}$, $\mathbf{a}$, and $\mathbf{F}$ cannot be chosen independently in classical physics, since $\mathbf{F}$ determines $\mathbf{a}$.

Furthermore, not all ball positions are allowed. For example, since the physical system of the football field, including two goals, were taken as the starting point, the ball cannot be placed at the already occupied position of a goalpost.

In classical physics the football is at one specific location, $\mathbf{r}$, but in quantum mechanics we learn that this view is not always possible for elementary particles (for a deeper discussion of wave-particle duality, see reference [3, chapter 1, 2]). Instead the best you can do is specify a probability of where the particle may be found. We describe this through a complex wave function (probability amplitude), $\Psi(t, \mathbf{r})$, which is related to the actual probability of where the particle may be found through $P(t, \mathbf{r}) = |\Psi(t, \mathbf{r})|^2$, see Figure 3.1 for an example.

Instead of following Newton's Law, the wave function evolves according to the Schrödinger equation [14, p. 97-98]:

$$i\hbar \frac{\partial \Psi(t, \mathbf{r})}{\partial t} = \hat{H}(t, \mathbf{r})\Psi(t, \mathbf{r}) \tag{3.2}$$

where $\hbar$ is the reduced Planck constant, and $\hat{H}(t, \mathbf{r})$ is the Hamiltonian that is related to the energy of the system. The Hamiltonian takes the place of the forces in the classical description in the sense that it is determined by the physical system. It is also a Hermitian operator such that its eigenvalues are real. As a result, for a static problem where the Hamiltonian does not change with time, i.e., $\hat{H}(t, \mathbf{r}) = \hat{H}_0(\mathbf{r})$, the wave function must depend on time in the form of a complex exponential function:

$$\Psi(t, \mathbf{r}) = \Psi_n(\mathbf{r})e^{-i\omega_n t} \tag{3.3}$$

When plugged into Equation (3.2) we arrive at the time-independent Schrödinger equation [14, p. 98-100]:

$$\hbar\omega_n \Psi_n(\mathbf{r}) = E_n \Psi_n(\mathbf{r}) = \hat{H}_0(\mathbf{r})\Psi_n(\mathbf{r}) \tag{3.4}$$

This is an eigenvalue problem. For a given Hamiltonian, it results in a set of eigenvalues or energies $E_n = \hbar\omega_n$ with corresponding wave functions $\Psi_n(\mathbf{r})$ that evolve with time in phase space at frequency ω_n according to Equation (3.3).

Regardless of whether the Hamiltonian is time-dependent or not, the wave function evolves deterministically according to the Schrödinger equation, Equation (3.2). Furthermore, when performing a measurement of the particle's position, Born's rule states that the result is given with a probability $|\Psi(t, \mathbf{r})|^2$ [15]. Measurements are therefore completely random in quantum mechanics, but the evolution of a particle's probability function is not.

The Copenhagen interpretation of quantum mechanics states that the wave function randomly collapses to one of the possible positions when a measurement is performed [16].

Analogously to the football that cannot be located at the goalposts, the physical system described in the Hamiltonian does not allow the wave function to be arbitrarily chosen. This is seen explicitly in the next section where the Hamiltonian of an infinite well is examined.

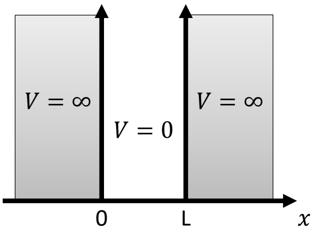

Figure 3.2. *An infinite well where the potential is infinite outside the area* $0 \to L$ *and zero inside.*

3.1.1 Analyzing the infinite well potential

This section solves the one-dimensional time-independent Schrödinger equation for an electron inside the infinite well potential, $V(x)$, seen in Figure 3.2. The potential energy outside the area $0 < x < L$ is infinite, whereas it is zero if x is inside the well.

The Hamiltonian of the system is:

$$\hat{H}_0 = \frac{-\hbar^2}{2m}\frac{\partial^2}{\partial x^2} + V(x) \tag{3.5}$$

where the first term is related to the non-relativistic kinetic energy of the electron, $E_K = \frac{1}{2}mv_x^2 = \frac{1}{2}\frac{p_x^2}{m}$, where p_x is the classical momentum related to the quantum operator $\hat{p}_x = -i\hbar\frac{\partial}{\partial x}$.

Since the particle cannot have infinite energy, the wave function must be zero outside and at the boundary of the well. Possible solutions to the time-independent Schrödinger equation are:

$$\begin{aligned} \Psi_n(x) &= A\sin\left(\frac{\pi n}{L}x\right) && 0 < x < L \qquad (3.6)\\ \Psi_n(x) &= 0 && x \leq 0,\ x \geq L \end{aligned}$$

where $A = \sqrt{2/L}$ is a normalization constant to ensure that the probability of finding the electron somewhere inside the well is 1, and n is a positive integer $1, 2, 3....$

When inserting this into Equation (3.4), you arrive at:

$$E_n = \frac{\hbar^2}{2m}\frac{\pi^2 n^2}{L^2} \tag{3.7}$$

In Figure 3.1 the first few solutions for $n = 1 \rightarrow 3$ are shown. As can be seen, the physical system characterized by the Hamiltonian, $\hat{H}_0$, limits the wave function to certain states, $\Psi_n(x)$, that are related to the probability of finding the electron at a position x through $P(x) = |\Psi_n(x)|^2$. These states have specific energies, E_n. Note that in our current simple model, if the electron is in an eigenstate, it stays there indefinitely.

The splittings between these energy levels divided by $\hbar$ are the resonance frequencies discussed in Chapter 2, where the strength of the interaction, f_k in Section 2.3, is set by the transition dipole moment discussed later in connection with Equation (3.18).

In quantum mechanics, the position and momentum wave functions are related through a Fourier transform [14, p. 53-55], i.e., by knowing the wave function in space $\Psi_n(x)$, you also know the wave function in momentum, $\Phi_n(p_x)$, where $|\Phi_n(p_x)|^2$ is the probability of the electron having a certain momentum p_x.

$$\Phi_n(p_x) = \frac{1}{\sqrt{2\pi\hbar}} \int \Psi_n(x) e^{-\frac{i}{\hbar}p_x x} dx \tag{3.8}$$

Since time and frequency are also related by a Fourier transform, the description of how a pulse with finite duration is created by a distribution of frequencies described in Section 2.2 is valid here as well. The wave function in space, $\Psi_n(x)$, is created by a distribution of the spatial frequencies or momenta, $\Phi_n(p_x)$. Thus, to make the position more local, the distribution in momentum space must become wider, or vice versa. This leads to the Heisenberg uncertainty principle [14, p. 33-35, 45-46]:

$$\Delta x \Delta p_x \geq \frac{\hbar}{2} \tag{3.9}$$

$$\Delta t \Delta E \geq \frac{\hbar}{2} \tag{3.10}$$

where Δ denotes the spread, or uncertainty, of the position, momentum, time, or energy. In other words, the Heisenberg uncertainty principle is a mathematical consequence of the particle being described as a wave that exhibits Fourier relations between position and momentum or, alternatively, time and energy.

In conclusion, from the classical point of view, $\mathbf{r}$, $\mathbf{v}$, and $\mathbf{F}$ can initially be chosen independently whereas $\mathbf{a}$ depends on $\mathbf{F}(\mathbf{r}, \mathbf{v})$ per Newton's second Law and is therefore already determined and cannot be chosen arbitrarily. In quantum mechanics, you can choose only the initial $\Psi_n(x)$ and $\hat{H}$ independently, i.e., the position probability and the physical system, since the momentum wave function, $\Phi_n(p_x)$, is related to the position through Equation (3.8).

3.2 Light-matter interaction in quantum mechanics

Let us now return to light-matter interaction, but this time study it from the perspective of matter.

Consider an electron that surrounds an atom, and for the sake of simplicity, neglect all states except the ground and first excited state, with energies E_g and E_e, and wave functions $|g\rangle = \Psi_g(x)$ and $|e\rangle = \Psi_e(x)$, where Dirac notation is used [14, p. 10-23].

When light disturbs the atom, an interaction term, $\hat{H}_I(t)$, must be added to the Hamiltonian. The electron oscillates due to the field and can be described as a dipole $q_e\mathbf{r}$, where $\mathbf{r}$ is the displacement with respect to the electron's center of mass. The interaction term should therefore correspond to the energy of a dipole in an electric field, $\mathbf{E}(t) = \frac{1}{2}\mathbf{E}_0 e^{-i\omega t} + \text{c.c.}$, where c.c. denotes the complex conjugate of what was written before. The electric field is now described in its real instead of complex form, as in the previous chapter where it was understood that only the real component yielded the actual field. The reason is that quantum mechanics is already a complex theory. Note however, that $\mathbf{E}_0$ is still complex in order to describe all possible incoming fields, i.e., combinations of $\cos(\omega t)$ and $\sin(\omega t)$. The interaction term of the Hamiltonian is

$$\hat{H}_I(t) = -\frac{1}{2} q_e \hat{\mathbf{r}} \cdot \mathbf{E}_0 e^{-i\omega t} + \text{c.c.} \tag{3.11}$$

This interaction couples the ground state, $|g\rangle$, with the excited state, $|e\rangle$, such that the wave function can transition between or into a superposition of the two states:

$$\begin{aligned} |\Psi\rangle &= \alpha|e\rangle + \beta|g\rangle \\ |\alpha|^2 + |\beta|^2 &= 1 \end{aligned} \tag{3.12}$$

where α and β are complex coefficients and the second expression normalizes the wave function to 1. Alternatively, it can be written as a function of two angles, θ and ϕ, which will be useful in Section 3.2.1.

$$|\Psi\rangle = \cos\frac{\theta}{2}|e\rangle + e^{i\phi}\sin\frac{\theta}{2}|g\rangle \tag{3.13}$$

The wave function can also be described as a density matrix [14, p. 180-185]:

$$\rho = |\Psi\rangle\langle\Psi| \tag{3.14}$$

In matrix form, where $|e\rangle = \begin{pmatrix}1\\0\end{pmatrix}$ and $|g\rangle = \begin{pmatrix}0\\1\end{pmatrix}$, this becomes

$$\rho = \begin{pmatrix}\alpha\\ \beta\end{pmatrix}\begin{pmatrix}\alpha^* & \beta^*\end{pmatrix} = \begin{pmatrix}|\alpha|^2 & \alpha\beta^* \\ \alpha^*\beta & |\beta|^2\end{pmatrix} = \begin{pmatrix}\rho_{ee} & \rho_{eg} \\ \rho_{ge} & \rho_{gg}\end{pmatrix} \tag{3.15}$$

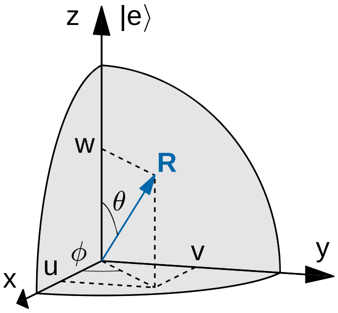

Figure 3.3. *The blue arrow represents the Bloch vector, $R = (u, v, w)$, shown here in the positive octant of the Bloch sphere together with the definition of θ and ϕ from Equation (3.13). $|e\rangle$ and $|g\rangle$ are located at $z = 1$ and $z = -1$, respectively.*

This can be rewritten to form three new real variables: u and v that relate to the phase of the wave function, and w that corresponds to the excitation:

$$\begin{aligned} u &= \rho_{eg} + \rho_{ge} \\ v &= i(\rho_{eg} - \rho_{ge}) \\ w &= \rho_{ee} - \rho_{gg} \end{aligned} \tag{3.16}$$

The evolution of these variables under the interaction Hamiltonian $\hat{H}_I(t)$ can be described by the Bloch equations [17, 18]:

$$\begin{aligned} \dot{u} &= -\frac{u}{T_2} - \delta v + \Omega_{\mathrm{Im}} w \\ \dot{v} &= \delta u - \frac{v}{T_2} + \Omega_{\mathrm{Re}} w \\ \dot{w} &= -\Omega_{\mathrm{Im}} u - \Omega_{\mathrm{Re}} v - \frac{w+1}{T_1} \end{aligned} \tag{3.17}$$

where T_1 and T_2 are the life and coherence times that determine how fast the atom decays, as discussed further in Sections 3.2.1 and 3.3. δ is the detuning between the transition (resonance) frequency, $\omega_0 = (E_e - E_g)/\hbar$, and the light frequency, ω, i.e., $\delta = \omega_0 - \omega$.

Ω_{Re} and Ω_{Im} are the real and imaginary parts of the Rabi frequency, Ω, which describes how rapidly the transition is driven, i.e., how fast it oscillates between the two states. It is related to the transition dipole moment and electric field through

$$\Omega = \frac{\boldsymbol{\mu}_{eg} \cdot \mathbf{E_0}}{\hbar} \tag{3.18}$$

where the transition dipole moment, $\boldsymbol{\mu}_{eg} = \langle e|q_e\hat{\mathbf{r}}|g\rangle$, is the overlap of the two states with respect to the dipole operator $q_e\hat{\mathbf{r}}$. Whether the Rabi frequency is real, imaginary, or complex, is set by the complex electric field amplitude $\mathbf{E}_0$, and can therefore easily be controlled by experimentalists.

Now that the mathematical description is complete, the next three subsections go through an intuitive way of describing the evolution of a two level atom interacting with light, the connection between a superposition and the oscillation of a charge, as well as how to relate this view to what was described in Chapter 2.

3.2.1 Bloch sphere

A two-level superposition state can, according to Equation (3.13), be written as a function of two angles and therefore be pictured as lying on a sphere with radius 1, referred to as the Bloch sphere, the positive octant of which is shown in Figure 3.3. The ground, $|g\rangle$, and excited, $|e\rangle$, states are placed at the bottom and top of the sphere, respectively, and any state can be depicted by a Bloch vector, $\mathbf{R}$, that points from the center towards the surface of the sphere. Conveniently, the variables u, v, and w introduced in Equation (3.16) are the components of the Bloch vector along the axes x, y, and z, i.e., $\mathbf{R} = (u, v, w)$.

The lifetime, T_1 in Equation (3.17), determines how quickly the atom relaxes toward the ground state at $w = -1$, and the coherence time, T_2, sets how long phase knowledge, described in u and v, can be kept. Both of these effects can reduce the length of the Bloch vector, $|\mathbf{R}| = R$, to be less than 1, which describes incomplete knowledge about the state.

When the life and coherence times are long compared to an interaction, the T_1 and T_2 terms can be neglected in Equation (3.17). If the interacting electric field also has a constant frequency, the evolution of the Bloch vector is a rotation, using the right-hand rule, around the vector $\mathbf{W} = (-\Omega_{\text{Re}}, \Omega_{\text{Im}}, \delta)$, since the Bloch equations can then be written as

$$\dot{\mathbf{R}} = \mathbf{W} \times \mathbf{R} \tag{3.19}$$

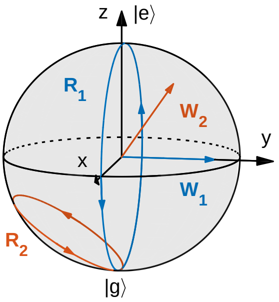

Figure 3.4. *The evolution of the Bloch vector* $\mathbf{R}$ *for starting state* $|g\rangle$ *is shown for the resonant case in blue with subscript 1, and in red for a detuned case with subscript 2. The state vectors rotate around the driving vectors* $\mathbf{W}$.

See Figure 3.4 for two examples where the initial state is $|g\rangle$, Ω is purely imaginary, and for the blue line $\delta = 0$ whereas for the red line $\delta > 0$. The angular velocity at which the state vector revolves around the Bloch sphere is given by the generalized Rabi frequency, $\Omega_G = \sqrt{|\Omega|^2 + \delta^2}$. Since all decays are neglected, the Bloch vectors trace out perfect circles as time goes on.

Resonant interaction with light therefore causes a two level atom to absorb energy and be put into, first, a superposition and eventually the excited state. If the interaction continues, the atom starts to deexcite towards the ground state once more, but now on the opposite side of the Bloch sphere.

Since the z component, w, describes the excitation (energy) of the atom, and the evolution is driven at a constant angular speed given by Ω_G, the atom does not absorb the same amount of energy in each time interval. For the resonant case, the absorption per time interval starts low and increases to a maximum when the Bloch vector reaches the equatorial plane before once more decreasing until it reaches the top pole. If the atom is driven even farther, the excitation decreases such that it gives off energy to the electric field, i.e., stimulated emission.

Even though Chapter 2 only discussed absorption in the linear regime, i.e., very close to the bottom pole, it is also valid for the linear regime of gain at the top pole by changing the sign of the decay parameter γ to negative instead of positive. The phases described in Section 2.1.3 therefore switch signs and, when adding the 90 degree phase shift due to the sum of all induced fields from a plane of electrons as described in Section 2.1.4, the total phase changes from $90 + 90 = 180$ degree for the resonance case, which caused absorption, to $-90 + 90 = 0$ degree, such that the induced electric field constructively add to the incoming field, as described above.

3.2.2 Connection between superpositions and light radiation

According to Equation (3.3) each eigenstate of the Hamiltonian evolves with a phase factor $e^{-i\omega_n t}$, where $\omega_n = E_n/\hbar$ is related to the energy of the state. For the superposition seen in Equation (3.12), the two terms therefore evolve differently as a function of time. Any global phase factor of the wave function can be neglected, since taking the absolute square to arrive at the probability density makes it 1. However, as discussed below, the relative phase matters.

The time evolution of such a superposition can be written as:

$$|\Psi(t)\rangle = \alpha|e\rangle + \beta e^{i\omega_0 t}|g\rangle \tag{3.20}$$

where $\omega_0 = \omega_e - \omega_g$, and $|\alpha|^2 + |\beta|^2 = 1$ to keep the state normalized.

The wave function, $\Psi(x,t)$, and probability density, $|\Psi(x,t)|^2$, are shown in Figure 3.5 for four different superpositions of the two lowest infinite well states, described by Equation (3.6) for $n = 1$ and 2, at three different times. In case 1: $\alpha = 0$, $\beta = 1$; case 2: $\alpha = \sqrt{1/8}$, $\beta = \sqrt{7/8}$; case 3: $\alpha = 1/\sqrt{2}$, $\beta = 1/\sqrt{2}$; and case 4: $\alpha = 1$, $\beta = 0$. As can be seen, the probability density does not change with time in case 1 or 4 where the system is in a pure state, but in case 2 and 3 the probability of where to find the electron oscillates back and forth. Using the knowledge of Chapter 2, we expect the electron to induce its own field that, depending on phase relations, can destructively or constructively interfere with the incoming electric field and absorb or release energy to the field. This oscillation is highest in case 3 where $\alpha = \beta = 1/\sqrt{2}$, which again shows that the induced electric field and absorption are strongest for states at the equator.

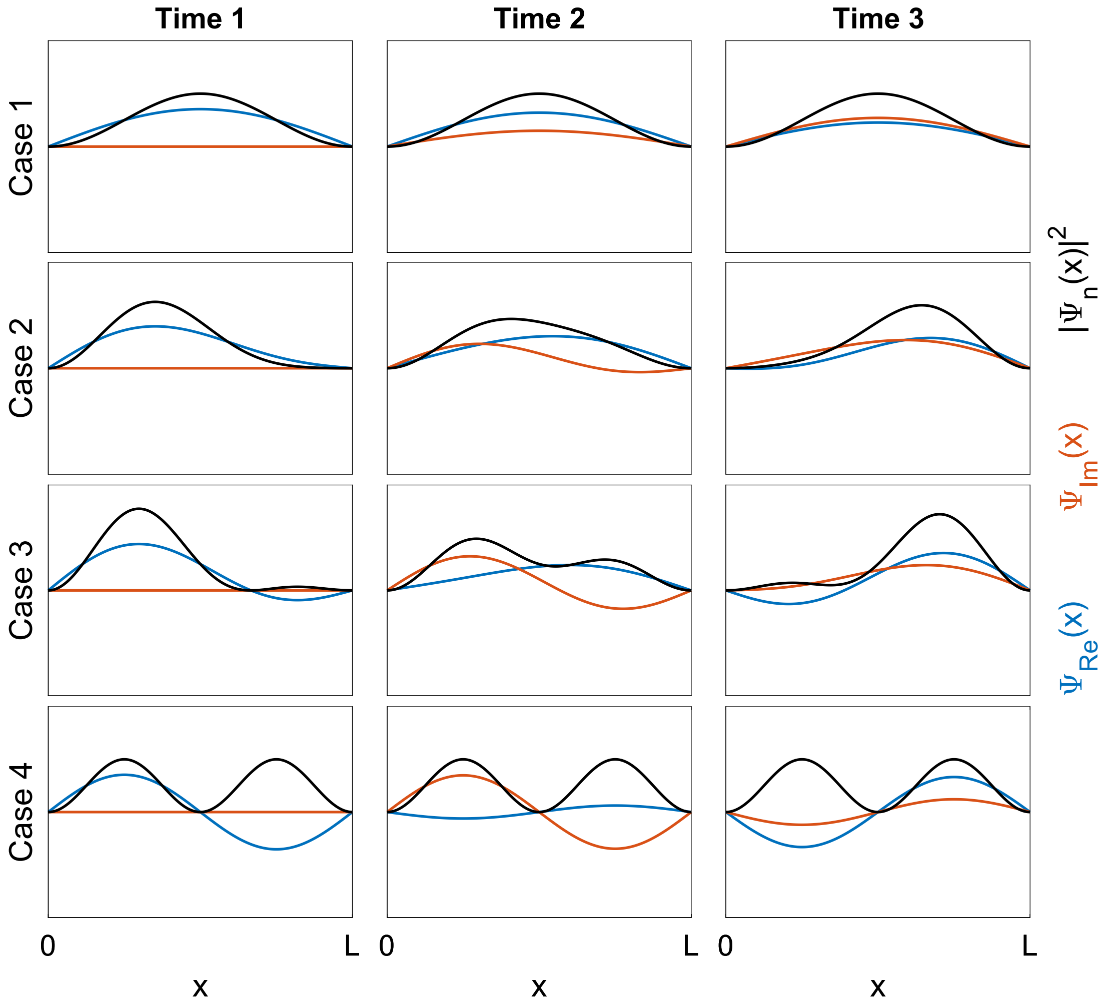

Figure 3.5. *Shows the evolution of four different superposition cases, written in the form of Equation (3.20), at three different times. The wave function's real and imaginary parts are shown in blue and red, respectively, and the probability density is shown in black. Case 1:* $\alpha = 0$, $\beta = 1$; *case 2:* $\alpha = \sqrt{1/8}$, $\beta = \sqrt{7/8}$; *case 3:* $\alpha = 1/\sqrt{2}$, $\beta = 1/\sqrt{2}$; *and case 4:* $\alpha = 1$, $\beta = 0$.

3.2.3 Relation between the Bloch sphere and the wave description

In this subsection the Bloch sphere introduced in this chapter is connected with the wave description presented in Chapter 2. For these equations to be directly applicable to rare-earth-ion-doped crystals, which are discussed in Chapter 4, I assume that, in addition to the interaction with the atoms discussed here, the light interacts with background atoms, such as the host crystal atoms, which generates a background refractive index of n that is also incorporated into the wave vector $k = n\omega/c$.

Once more the incoming electric field is defined as $\mathbf{E}_{\text{in}}(t,\mathbf{r}) = \frac{1}{2}\mathbf{E}_0 e^{-i(\omega t - kz)} + \text{c.c.}$, i.e., the same convention as in the previous chapter but now written in its real form. Alternatively, it can be written as

$$\begin{aligned}
\mathbf{E}_{\text{in}}(t,\mathbf{r}) &= \mathbf{E}_0^{\text{Re}} \cos\left(\omega t - kz\right) + \mathbf{E}_0^{\text{Im}} \sin\left(\omega t - kz\right) \\
\mathbf{E}_0 &= \mathbf{E}_0^{\text{Re}} + i\mathbf{E}_0^{\text{Im}} \\
\mathbf{E}_{\text{in}}(t,\mathbf{r}) &= \frac{\hbar \mathbf{e}_x}{|\boldsymbol{\mu}_{eg}|} \left(\Omega_{\text{Re}} \cos\left(\omega t - kz\right) + \Omega_{\text{Im}} \sin\left(\omega t - kz\right)\right)
\end{aligned} \tag{3.21}$$

where it in the last line has been related to the complex Rabi frequency, $\Omega = \Omega_{\text{Re}} + i\Omega_{\text{Im}}$, through Equation (3.18), where I assume that the field polarization direction, $\mathbf{e}_x$, is aligned with the transition dipole moment.

In order to see how the atom affects the light, the Bloch equations shown in Equation (3.17) are expanded into Maxwell-Bloch equations, which include the following additions [19, 20]:

$$\begin{aligned}
\left(\frac{\partial}{\partial z} + \frac{n}{c}\frac{\partial}{\partial t}\right)\Omega_{\text{Re}} &= \frac{\alpha_0}{2\pi}\int_{-\infty}^{+\infty} g(\delta) v d\delta \\
\left(\frac{\partial}{\partial z} + \frac{n}{c}\frac{\partial}{\partial t}\right)\Omega_{\text{Im}} &= \frac{\alpha_0}{2\pi}\int_{-\infty}^{+\infty} g(\delta) u d\delta
\end{aligned} \tag{3.22}$$

where n is the background refractive index, and $g(\delta)$ is the absorption distribution as a function of the detuning, $\delta = \omega_0 - \omega$, normalized such that it equals one where α_0, the absorption coefficient, is measured. This back action from the atoms to the light is based on a macroscopic polarization and should qualitatively yield the same results as in Section 2.1.5, i.e., it includes the additional 90 degree phase shift originating from summing over a plane of oscillating atoms, as described in Section 2.1.4. Note that u, v, w, Ω_{Re}, and Ω_{Im} now also varies with the spatial variable z, and not just with time.

The $\frac{n}{c}\frac{\partial}{\partial t}$ term can be neglected in our experiments since it contributes only when changes are fast, i.e., on a timescale of $\frac{nL}{c}$, where L is the crystal length.

In order to more easily examine a small change in the Rabi frequency, or electric field, as it propagates through the material, and obtain the same phase relations between the incoming and induced fields as in Chapter 2, the equations are rewritten as follows:

$$\begin{aligned} \Delta\Omega_{\mathrm{Re}} &= \frac{\alpha_0}{2\pi} v \cdot \Delta\delta \cdot \Delta z \\ \Delta\Omega_{\mathrm{Im}} &= \frac{\alpha_0}{2\pi} u \cdot \Delta\delta \cdot \Delta z \end{aligned} \tag{3.23}$$

where the integration over all detunings is assumed to give $v \cdot \Delta\delta$ and $u \cdot \Delta\delta$, respectively, and Δ is used to denote a small change or interval for the parameter in question.

In Figure 3.6, three examples are given where the incoming Rabi frequency is always purely imaginary, $\Omega_{\mathrm{Im}} > 0$, but the detuning is varied. In Figure 3.6(a), the detuning is positive and $|\delta| > |\Omega_{\mathrm{Im}}|$, but in order to show the effect, it is not made much larger. Using the right-hand rule to rotate the Bloch vector $\mathbf{R} = (u, v, w)$ around the driving vector $\mathbf{W} = (-\Omega_{\mathrm{Re}}, \Omega_{\mathrm{Im}}, \delta)$, the Bloch vector first gains a negative u component, then a negative v component, and finally a positive u component before it returns to the ground state. From Equation (3.23), this corresponds to Rabi frequency changes of $\Delta\Omega_{\mathrm{Im}} < 0$, $\Delta\Omega_{\mathrm{Re}} < 0$, and $\Delta\Omega_{\mathrm{Im}} > 0$, respectively. Since the incoming Rabi frequency was $\Omega_{\mathrm{Im}} > 0$, the first and last parts correspond to absorption and gain, respectively. A negative real Rabi frequency is a factor of i, 90 degree after in phase, compared to the incoming field $\Omega_{\mathrm{Im}} > 0$. Thus, the middle part corresponds to a delayed light field. In summary, light is first absorbed, then delayed, and finally re-emitted as gain. The rotational speed of the Bloch vector is set by the magnitude of the driving vector, $|\mathbf{W}|$. For large detunings, it processes on a timescale of $1/|\delta|$. Since the absorption and gain parts cancel each other out, the overall effect is a delay of the incoming field, i.e., an increase in the refractive index, just as obtained in Section 2.1.5.

The detuning is zero in Figure 3.6(b), i.e., showing the resonant interaction case. The Bloch vector gains a positive and then negative u component, corresponding to absorption and gain, respectively, according to similar logic as discussed in the previous paragraph. This agrees with a positive imaginary part of the refractive index for absorption using $\gamma > 0$, or a negative part for gain when $\gamma < 0$.

In Figure 3.6(c), the detuning is negative, which results in Bloch vector changes of negative u, positive v, and positive u. A $v > 0$ corresponds to $\Delta\Omega_{\mathrm{Re}} > 0$, i.e., -90 degree $(-i)$ earlier in phase or a reduction of the refractive index, which is also obtained using Equations (2.12) or (2.25).

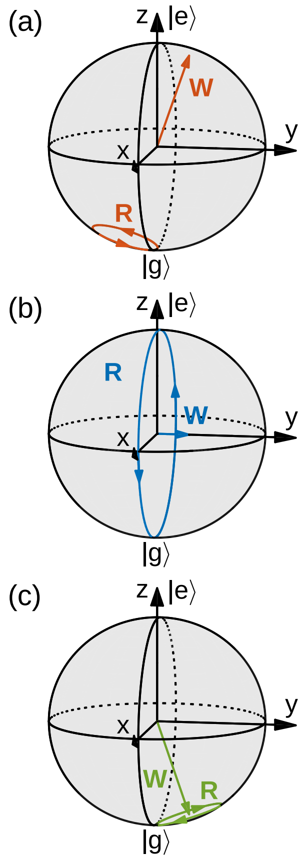

Figure 3.6. *Driving of the Bloch vector* $\mathbf{R}$ *around the driving vector* $\mathbf{W}$ *using a positive imaginary Rabi frequency,* $\Omega_{Im} > 0$*, for three different detunings: (a)* $\delta > 0$ *and* $|\delta| > |\Omega_{Im}|$*, (b)* $\delta = 0$*, and (c)* $\delta < 0$ *and* $|\delta| > |\Omega_{Im}|$*. See the main text for further description.*

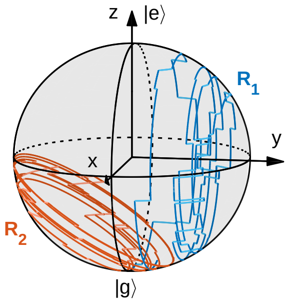

Figure 3.7. *When dephasing is present at random intervals and magnitudes, it alters the phase angle ϕ of the Bloch vector, lighter-colored segments. Thus, the evolution of the resonant, blue line, and detuned, red line, cases no longer trace perfect circles, as in Figure 3.4. In this figure it is assumed that each dephasing event occurs on a time scale much shorter than 1 over the Rabi frequency.*

3.3 Decays

The interaction that we added in Section 3.2, $\hat{H}_I(t)$, was used to describe a field controlled by the experimentalists, but any field (both electric and magnetic) in the presence of the atom adds similar terms to the Hamiltonian, as do phonon interactions. Thus, it is not surprising that the atom may be disturbed and change its phase or excitation without the knowledge of the experimentalists. These decays are described by their exponential time dependence through the coherence time, T_2, and lifetime, T_1. Much work goes into isolating systems such that these interactions are kept to a minimum [21–23].

3.3.1 Coherence time

If an interaction between an atom and its environment causes only phase changes, it shortens the coherence time, T_2, of the atom. Such a decoherence process results in a difference between the phase of the atom and, e.g., a laser controlled by the experimentalists. As a result, the path in the resonant case, blue lines, does not evolve as in Figure 3.4 but as in Figure 3.7, where the dephasing events, lighter-colored segments, are seemingly random in both direction and size, and occur on a time scale much shorter than 1 over the Rabi frequency. This lack of knowledge leads to a perceived shortening of the Bloch vector as the final state becomes more uncertain each time a random dephasing event occurs.

This decoherence also allows an atom to more easily absorb light that is slightly detuned, red lines, since instead of keeping its rotation close to the bottom part of the Bloch sphere as in Figure 3.4, it can reach a higher excitation due to these phase disturbances, see Figure 3.7. Thus, incoming light needs only to be sufficiently close to the resonance frequency of the atom in order to be absorbed. The frequency width of where the atom absorbs, referred to as the homogeneous linewidth, Γ_{hom}, is inversely related to the coherence time:

$$\Gamma_{\text{hom}} = \frac{1}{\pi T_2} \tag{3.24}$$

To understand another effect of decoherence, picture a laser that partly excites N atoms situated in a crystal. Since the laser beam travels at a finite speed, its phase evolves during propagation and the first atom has a different phase compared to the last atom of the crystal. However, the field induced by the first atom that travels in the same direction as the laser reaches each new atom in phase with its oscillations, since the phase of this induced field evolves at the same rate during propagation as the phase of the initial laser field. As a result, all atoms oscillate such that their fields add constructively in the forward direction, creating

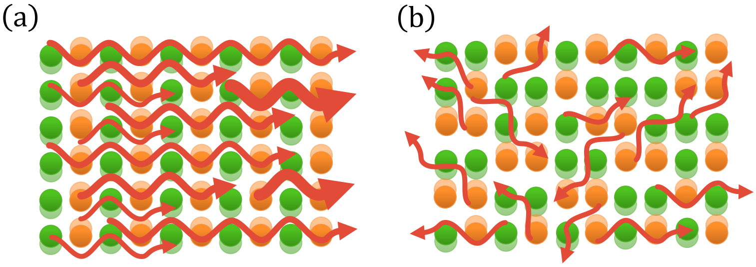

Figure 3.8. *Oscillating atoms, green moving upwards and orange downwards, induce fields that in (a) add coherently in the forward direction as the atoms oscillate in phase, whereas in (b) the intensities are spread out over all directions due to the random phases of the atoms.*

a formidable intensity scaling as N^2, see Figure 3.8(a). In other directions, the resulting field is much lower due to the phase differences of the atoms. However, if decoherence processes target each atom randomly, the constructive interference in the forward direction quickly dies off. The atoms are still excited but with random phase relations. Thus, the induced field radiates in all directions and its intensity is proportional to N, i.e., the net result is as though we were adding intensities instead of fields for incoherent processes, see Figure 3.8(b).

Sometimes you can compensate for the interactions that cause the decoherence. For example, if the dephasing occurs gradually over some time t_{de} and the experimentalist can alter the direction of the phase shift on a time scale $t_{\mathrm{alt}} \ll t_{\mathrm{de}}$, the overall dephasing can be made almost negligible as the phase first evolves in, e.g., the positive direction but is then switched by the experimentalist after a time t_{alt} to evolve in the negative direction, thereby canceling out the previously gained positive phase. Such interactions can therefore be disregarded and a longer coherence time can once more be obtained. This method of increasing the coherence time is called dynamic decoupling [24, 25].

In conclusion, coherence time is a measure of how long two or more systems can remain in phase, and can sometimes be compensated for by clever tricks that utilize our knowledge of the processes that cause the decoherence [26].

3.3.2 Lifetime

Whereas coherence time, T_2, measures the decay of phase, lifetime, T_1, describes the decay of excitation. T_1 interactions are similar to the ones described in the previous section but change θ instead of ϕ in Equation (3.13) and Figure 3.3, and can only move the Bloch vector towards the ground state.

The lifetime also limits the longest possible coherence time by $T_2 \leq 2T_1$, since the state eventually decays to the ground state where no phase exists. A factor of 2 is needed, since lifetime measures decay of excitation, i.e., energy, whereas coherence time measures decay of phase, i.e., amplitude, and energy $\propto$ amplitude^2.

Even an isolated atom decays from excited states. This is called spontaneous emission and gives rise to the finite lifetime of excited levels. The exact reason for the decay is still being discussed. The general consensus is that it relates to interactions with vacuum field fluctuations and/or self-reaction (also known as the radiation reaction field), i.e., interaction with its own induced field. However, the degree to which these effects come into play is debated. In reference [27], Milonni offers an overview of the discussion and emphasizes the fluctuation-dissipation connection between the two effects [28]: one cannot exist without the other. These effects cancel each other out for the ground state, thus rendering it stable [27]. Puri later argued that the vacuum field fluctuations could be mathematically removed and therefore made no real contribution to the spontaneous emission [29], but Milonni quickly refuted him and once more emphasized the importance of the connection between the two [30]. Very recently, Pollnau has suggested that for each frequency there exist two counter-propagating modes, each carrying a zero-point energy of 1/2 vacuum photon, that project their vacuum energy onto each other, since the modes are not orthogonal but anti-parallel, and vacuum fluctuations can, therefore, alone quantitatively describe spontaneous emission [31].

Aware of this debate, I will anyway try my best to explain the physical reason for spontaneous emission, with the precaution that the rest of the section may be open to question. First, I present a semiclassical hypothesis for spontaneous emission. Second, I discuss statistical properties of the process.

Consider a two level atom in the excited eigenstate at time t_0. Due to the vacuum field fluctuations, the Hamiltonian, and therefore the eigenstates, changes such that at time $t_0 + \Delta t$, the atom is in a tiny superposition between the new ground and excited eigenstates. As explained in Section 3.2.2, this superposition radiates light. According to our present understanding, this should start off slowly, but as more and more energy is radiated away, the ground state probability increases and the Bloch vector turns towards the equator, where the oscillation and radiation are strongest. The process slows down again as the ground state population becomes larger than that of the excited state, which results in an exponential tail of the decay process. This dissipation of energy due to the oscillation of the charge can be seen as self-reaction [27]. In reality, the decay is exponential from the beginning (disregarding small- and long-time deviations [32–34]) which this semiclassical model does not capture, but the vacuum fluctuations might be responsible for this initial increase of the decay.

The decay process is seemingly irreversible, i.e., the probability that the atom reabsorbs the spontaneously emitted photon is negligible (disregarding quantum revival [35] for now as we consider an isolated atom). This may be seen as a statistical property, since the photon can be created in an infinite number of modes, each corresponding to sending it out in different directions or polarizations, whereas the atom can only be excited or not. Thus, it is statistically much more likely for an atom to decay from the excited state and never reabsorb the emitted photon, resulting in an apparent spontaneous decay [36]. However, as hinted above, the process can be made unitary and reversible if you keep track of the vacuum modes, see cavity quantum electrodynamic [37] and quantum revival [35], and spontaneous emission is thus stimulated but from an unknown source, such as the vacuum field fluctuations.

This also indicates that incident light covering only a few modes is much more likely to scatter from one mode to another compared to being absorbed. In order to achieve significant absorption, i.e., a large percentage of the incoming photons are absorbed, many modes must be covered by the incoming light, for example by focusing on the atom or with induced fields generated by other atoms that oscillate together, as described in Section 2.1.4. This is understandable, since as the atom oscillates, it radiates out in a dipole pattern, see Section 2.1.1, which should at least partly cancel out the incoming light if any significant absorption is to be achieved. Thus, the larger the fraction of the dipole pattern modes that are covered by the incoming light, the higher the absorption can be.

3.4 DC Stark effect

If the external electric field is static instead of oscillating as described previously in Section 3.2, the energy levels of an atomic system shift due to the additional term in the Hamiltonian. This is called the (DC) Stark effect and occurs since a static field has a definite positive and negative side, and the electron wave functions that are shifted towards the positive side have lower energy than wave functions that are shifted towards the negative side. Furthermore, electrons in outer shells are more loosely bound to the nucleus and are therefore generally more affected by the external field, since they can move more easily.

Because each energy level has its own wave function, the energy splitting between levels generally changes when an external field is applied, which is used in Papers **III** and **IV**, as described in Sections 5.3 and 5.4.

Chapter 4

Rare-earth-ion-doped crystals

This chapter provides an overview of the properties of rare-earth elements doped into a crystal. For more detailed information see, e.g., Sun [38] or Macfarlane et al. [39].

In the growth process used for the crystals in this thesis, the Czochralski method, the desired rare-earth element is added to a melt of pure crystal ingredients and the crystal is slowly grown from this melt. The goal is to minimize defects, such as oxygenation centers, vacancies, imperfect crystal structure, and other atomic impurities, while attaining the desired doping concentration.

This chapter begins with Section 4.1, which describes the rare-earth elements, then Sections 4.1.1 and 4.1.2 discusses the benefits of 4f-4f transitions, and the hyperfine energy level structure of Pr^{3+}:Y_2SiO_5 and Eu^{3+}:Y_2SiO_5, respectively.

The host crystal, Y_2SiO_5 in this thesis, is discussed in Section 4.2. Following this, Section 4.3 discusses transition and static dipole moments, after which some properties of Pr^{3+}:Y_2SiO_5 and Eu^{3+}:Y_2SiO_5 are provided in Section 4.4.

Finally, the absorption profile of a rare-earth-ion-doped crystal is discussed in Section 4.5, using Pr^{3+}:Y_2SiO_5 as an example.

4.1 Rare-earth elements

The rare-earth elements are the 15 lanthanides, scandium, and yttrium, shown in the periodic table in Figure 4.1. This thesis involves mostly praseodymium (Pr), europium (Eu), and cerium (Ce) doped in yttrium orthosilicate (Y_2SiO_5). Thus, the discussions in this chapter are based on their properties.

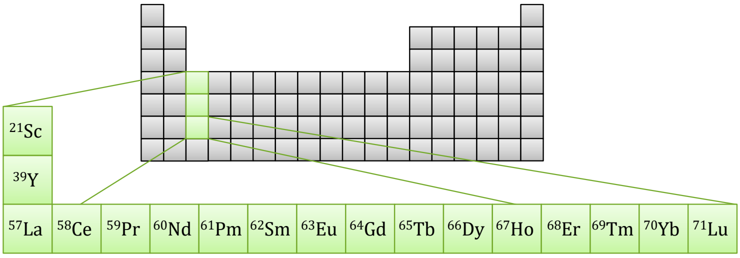

Figure 4.1. *Placement of the rare-earth elements, scandium, yttrium and the 15 elements in the lanthanides series in the periodic table.*

4.1.1 4f-4f transitions

The electron configurations of the lanthanides are based on the noble gas Xenon, which has filled 5s and 5p states but an empty 4f shell. For triply ionized (trivalent) lanthanides, which is the predominant oxidation state for the majority of them, the elements have 0-14 filled 4f states, starting from Lanthanum (La) and ending in Lutetium (Lu).

The filled 5s and 5p states are spatially extended farther out than the 4f electrons, see Figure 4.2, and therefore interact more with the surroundings, causing the chemical properties of the lanthanides to be roughly the same. This extension also causes them to act as a Faraday cage that protects the inner-lying 4f electrons from surrounding disturbances.

For a free atom, dipole transitions require a change of parity in the final state compared to the initial one. However, when doped into a crystal, which is the main topic of this thesis, the atom may sit in a site that is no longer inversion symmetric. Thus, parity is not a very good quantum number and forbidden transitions can become weakly allowed. This is the case for 4f-4f transitions in rare-earth elements doped into non-centrosymmetric crystals. Since these transitions are weak and shielded by the outer lying states, the life and coherence times can be long, but require cryogenic temperatures of around 4 K to eliminate phonon interactions.

Phonons follow Bose-Einstein statistics such that the probability of finding phonons in a given state with a certain frequency ω_p is:

$$P(\omega_p) = \frac{1}{\exp\left(\frac{\hbar\omega_p}{k_B T}\right) - 1} \tag{4.1}$$

where k_B is the Boltzmann constant and T is the temperature in Kelvin. Phonons generally scatter and cause decoherence, but the probability of this process scales as T^7 [41–43], for tempera-

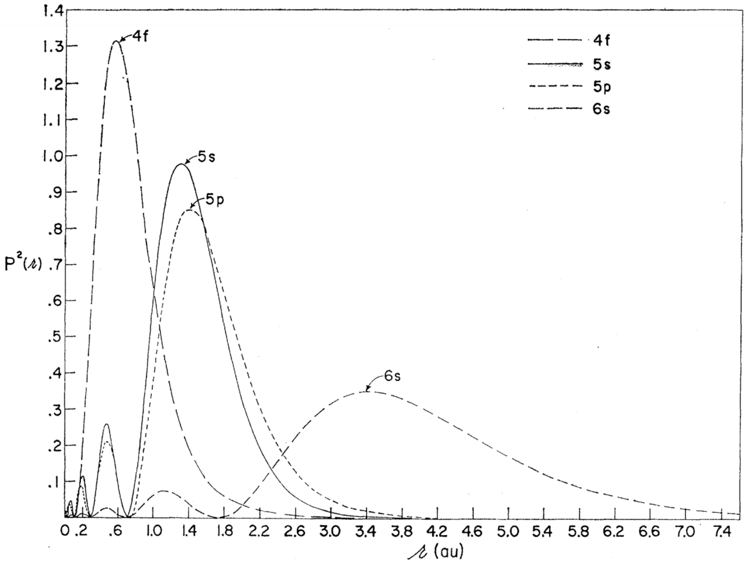

Figure 4.2. *Radial distribution of 4f, 5s, 5p, and 6s electron orbitals in Gadolinium (Gd). The 4f orbital is shielded from the environment by the energetically favorable outer-lying orbitals. The figure is reprinted with permission from [40].*

tures $T < 0.084T_D$, where T_D is the Debye temperature, which is equal to 580 K for Y_2SiO_5 [44]. Hence, at low temperatures (≤ 4 K), phonons no longer significantly disturb the properties of the 4f states.

Phonons can also cause non-radiative decay that reduces the lifetime of states, but these processes are considered unlikely if the transition require 5 or more phonons. For Y_2SiO_5, the maximum phonon energy is about 12 THz, and so transitions above 60 THz are mostly unaffected [44, 45].

Figure 4.3 shows an overview of calculated $4f^n$ energy levels of trivalent rare-earth ions doped into Lanthanum trifluoride (LaF_3). Even if the host material is different from Y_2SiO_5, the placements of the energy levels are similar.

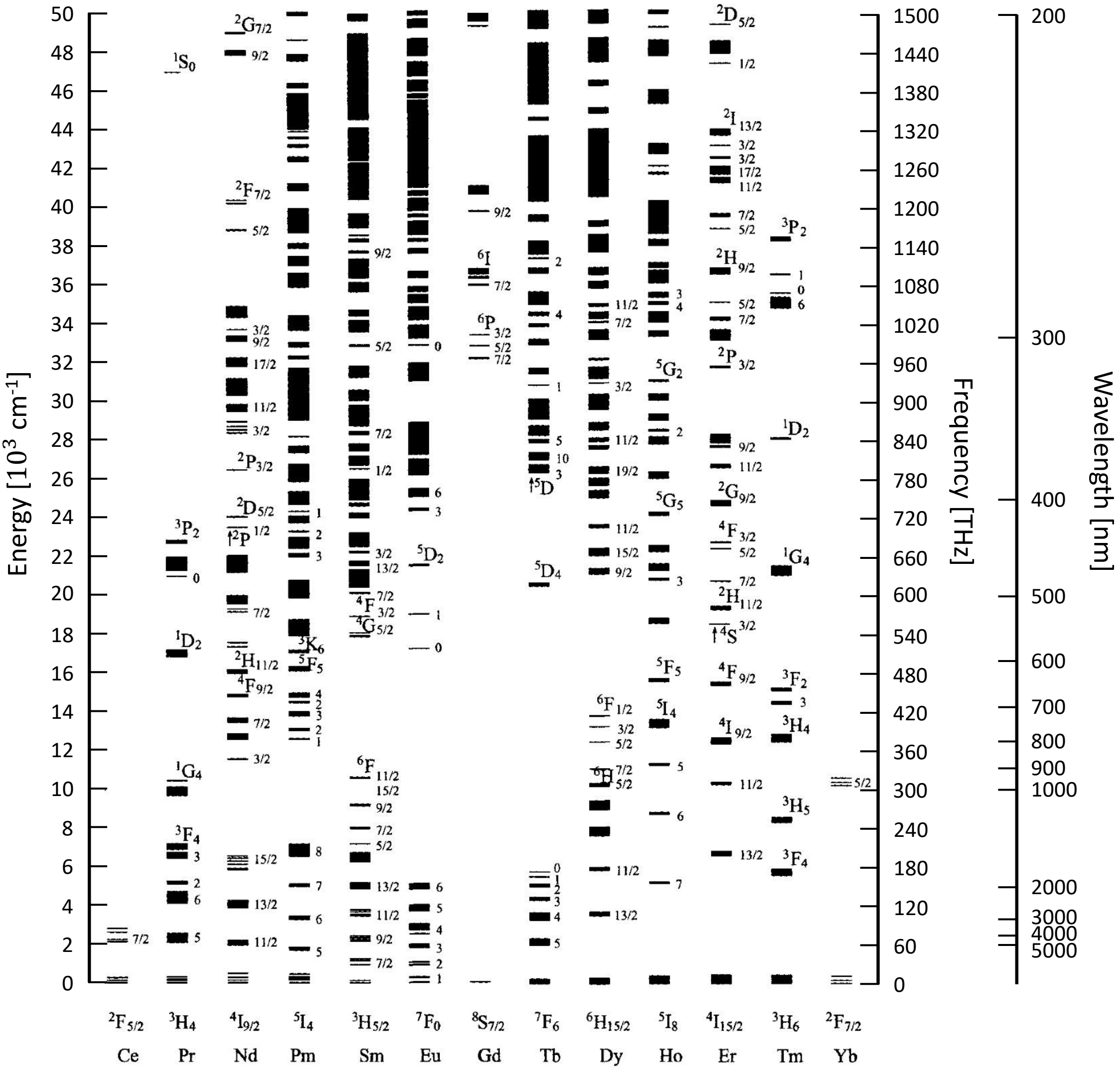

Figure 4.3. *Calculated 4f^n energy levels of most trivalent rare-earth elements doped into LaF$_3$. The levels also have similar positions in other host crystals, such as Y$_2$SiO$_5$, since the electrostatic interaction of the electron and nucleus, as well as the spin-orbital interaction, mostly determine the energies. The first figure, which shows the 4f^n energy levels in this way, referred to as a Dieke diagram, was originally printed in reference [46] for Lanthanum trichloride (LaCl$_3$) but has been reprinted several times since. I slightly modified this version from reference [47] and reprinted it here with permission.*

4.1.2 Hyperfine energy level structures

The transition used for Pr^{3+}:Y_2SiO_5 throughout this thesis is the $^3H_4 \rightarrow {}^1D_2$ located at 606 nm (495 THz), see Figure 4.3. Its hyperfine energy level structure can be seen in Figure 4.4.

The first-order hyperfine interaction in Pr^{3+}:Y_2SiO_5 (also Eu^{3+}:Y_2SiO_5) vanishes, since the orbital angular momentum is quenched [39]. A second-order interaction does however exist and depends on the square of the nuclear spin, causing all energy levels to be doubly degenerate at zero magnetic field. The levels in Figure 4.4 are denoted by the hyperfine quantum numbers $m_f = \pm 1/2$g, $\pm 3/2$g, $\pm 5/2$g for the ground states and similarly for the excited ones. However, as mentioned in the previous section, the ion interacts with the crystal and these quantum numbers are not "good". Thus, caution is warranted when, e.g., applying rules for transitions.

The transition of interest in Eu^{3+}:Y_2SiO_5 is $^7F_0 \rightarrow {}^5D_0$ located at 580 nm (517 THz). Eu has a similar energy level structure as Pr, i.e., three ground and excited hyperfine states, but with slightly larger energy splittings ranging from around 30 MHz to almost 300 MHz [38]. Furthermore, it has two isotopes, ^{151}Eu and ^{153}Eu, which differ in energy splittings.

Finally, any dopant is doped into both sites of yttrium by replacing one of the two possible Y in Y_2SiO_5, and have transitions at two slightly different wavelengths. For Eu, this means a total of four different combinations of isotope and site locations in Y_2SiO_5, but the complexity can be reduced by doping with isotopically pure Eu.

Ce^{3+} does not have any optical 4f-4f transition available, instead the 4f-5d zero-phonon transition at 371 nm (site 1) is used throughout this thesis. The excited state lifetime is only 40 ns [50] and the transition can be cycled many times with continuous excitation, making Ce a good candidate for single ion detection. This is discussed further in Sections 7.4 and 7.5.

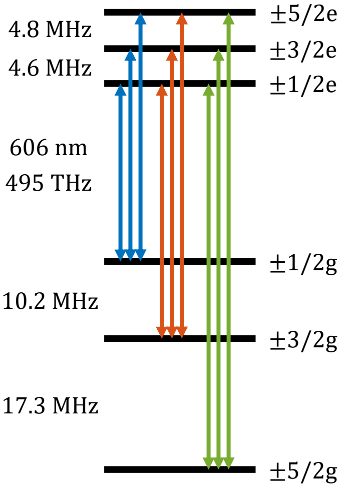

Figure 4.4. *Energy structure of Pr^{3+}:Y_2SiO_5 (site 1) [48, 49]. The arrows show the possible optical transitions, also seen in Figure 4.7, whose relative oscillator strengths are printed in Table 4.3.*

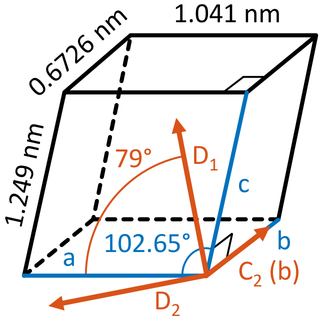

Figure 4.5. *The monoclinic Y_2SiO_5 crystal is shown with crystal axes a, b, and c, as well as principal axes D_1, D_2, and C_2 (often denoted by b instead since they are parallel).*

4.2 Yttrium orthosilicate (Y_2SiO_5) host crystal

Y_2SiO_5 crystals are monoclinic with eight molecules per cell, see Figure 4.5, where a, b, and c are the crystal axes. It is birefringent and therefore has three principal axes with slightly different refractive indices. These are called D_1, D_2, and C_2 (often denoted with b instead since they are parallel), with indices $n_{D_1} = 1.7881$, $n_{D_2} = 1.809$, and $n_{C_2} = n_b = 1.7851$ (for 606 nm) [51]. The Y_2SiO_5 crystal is frequently used as a host due to its low magnetic moments; silicon and oxygen have no nuclear spin and yttrium has spin 1/2 but with a low magnetic moment of $-0.137\mu_N$, where μ_N is the nuclear magneton [41]. Low magnetic moments are good, since they minimize the effect of spin flips that otherwise disturb the coherent properties of the dopants.

4.3 Transition and static dipole moments

A strong interaction with the environment generally result in short life and coherence times. However, a transition with a strong interaction, i.e., a large oscillator strength (proportional to the square of the transition dipole moment [52]), allows for easier control since the ions interact more with the laser light. The oscillator strength of Pr (site 1) is about $20-60$ times as strong as Eu, which lowers the requirements for available laser power in experiments [53, 54].

When Pr is used as a dopant in Y_2SiO_5 its transition dipole moment, $\boldsymbol{\mu}_{eg}$, have a direction that lies mostly in the D_1-D_2 plane, with a 74.6 ± 1.9 degree tilt from the D_1 axis [38]. In order to excite the ions, incoming light must have a polarization component along this direction. Fortunately, due to the phase retardation caused by the different refractive indices of the host crystal, absorption of light can be achieved regardless of polarization in the D_1-D_2 plane, since the polarization changes during propagation through the crystal. The strongest absorption is, however, achieved if the incoming polarization is aligned along the D_2 axis, see Paper **I**.

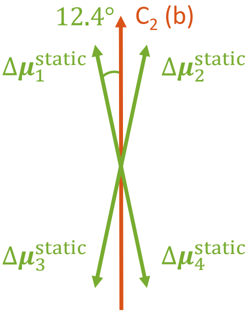

Figure 4.6. *The four possible static dipole moments, $\Delta\boldsymbol{\mu}_i^{\text{static}}$, in Pr^{3+}:Y_2SiO_5. They all form a 12.4 degree angle with the b axis [55], and lie in a plane that is tilted 35 degrees from the D_2 axis [56, 57].*

Furthermore, the static dipole moment of the ground and excited states are different due to differences in their wave functions, see Section 3.4, such that an external electric field can Stark shift the resonance frequency of the ions by $\Delta\omega$;

$$\Delta\omega = \frac{(\boldsymbol{\mu}_e^{\text{static}} - \boldsymbol{\mu}_g^{\text{static}}) \cdot \mathbf{E}}{\hbar} = \frac{\Delta\boldsymbol{\mu}^{\text{static}} \cdot \mathbf{E}}{\hbar} \tag{4.2}$$

where $\boldsymbol{\mu}_g^{\text{static}}$ and $\boldsymbol{\mu}_e^{\text{static}}$ are the static dipole moments of the ground and excited states respectively, and $\mathbf{E}$ is the external electric field at the location of the ion. This effect is used in Papers **III** and **IV**, where absorption structures are altered by shifting the resonance frequencies of absorbing ions, using an external electric field. In Pr^{3+}:Y_2SiO_5, four different possible directions exist for the static dipole moment difference, $\Delta\boldsymbol{\mu}^{\text{static}}$, which all make a 12.4 degree angle with the b axis [55], see Figure 4.6.

Since the static dipole moment of an ion is state dependent, it alters the surrounding electric field if the ion is excited, which in turn DC Stark shifts other nearby ions. This leads to instantaneous spectral diffusion, where the excitation of some ions causes dephasing or detuning of nearby ions. Usually this is problematic and is avoided by going to ever lower excitation populations. However, as discussed in Sections 7.3 and 7.4, it can also be used to make an ion control other nearby ions.

Property	Pr (site 1)	Pr (site 2)	Ref
λ_{vac}	605.977 nm	607.934 nm	[48]
ν	494.726 THz	493.133 THz	[48]
T_1 optical	164 µs	222 µs	[48]
T_2 optical	152 µs ($B = 7.7$ mT)	377 µs ($B = 7.7$ mT)	[48]
T_1 hyperfine	≈ 100 s	≈ 100 s	[58]
T_2 hyperfine	42 s ($B = 80$ mT)	-	[26]
Oscillator strength	$7.7 \cdot 10^{-7}$	$4.5 \cdot 10^{-8}$	[53]
μ_{eg}	$2.5 \cdot 10^{-32}$ C·m	$6.3 \cdot 10^{-33}$ C·m	[53]
$\Delta\mu^{\text{static}}$	$2.4 \cdot 10^{-31}$ C·m	$2.0 \cdot 10^{-31}$ C·m	[53]

Table 4.1: Properties of Pr^{3+}:Y_2SiO_5, in order: vacuum wavelength, frequency, optical lifetime, optical coherence time, hyperfine lifetime, hyperfine coherence time, oscillator strength, transition dipole moment, and the difference between the static dipole moment of the excited and ground states. Magnetic field strengths are noted when used, and the coherence times are achieved by implementing techniques in order to preserve phase information.

Property	Eu (site 1)	Eu (site 2)	Ref
λ_{vac}	579.879 nm	580.049 nm	[54]
ν	516.991 THz	516.840 THz	[54]
T_1 optical	1.9 ms	1.6 ms	[54]
T_2 optical	2.6 ms ($B = 10$ mT)	1.9 ms ($B = 10$ mT)	[54]
T_1 hyperfine	> 20 days	> 20 days	[41]
T_2 hyperfine	6 hours ($B = 1.35$ T)	-	[23]
Oscillator strength	$1.2 \cdot 10^{-8}$	$3.1 \cdot 10^{-8}$	[54]
μ_{eg}	$6.6 \cdot 10^{-33}$ C·m	-	[53]
$\Delta\mu^{\text{static}}$	$7.6 \cdot 10^{-32}$ C·m	-	[53]

Table 4.2: Properties of Eu^{3+}:Y_2SiO_5, see Table 4.1 caption for description.

4.4 An overview of praseodymium (Pr) and europium (Eu) properties in Y_2SiO_5

An overview of life and coherence times, as well as oscillator strengths, transition dipole moments, and differences of static dipole moments between excited and ground states, is provided in Tables 4.1 and 4.2 for Pr and Eu, respectively. For a broader overview of material properties, see reference [38].

The coherence times in the tables (especially the hyperfine) are reduced if necessary precautions are not taken, such as a magnetic field with correct magnitude and direction, as well as dynamic decoupling schemes as discussed in Section 3.3.1. Additionally, as mentioned in Section 4.1.1, phonons rapidly destroy the coherence of the excited state as the temperature goes above 4 K.

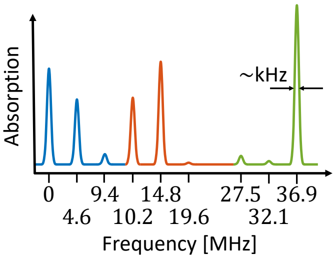

Figure 4.7. *Schematic view of the absorption spectrum for a Pr ion, doped into* Y_2SiO_5*, corresponding to the transitions seen in Figure 4.4. The peak heights correspond to their relative oscillator strengths, as written in Table 4.3.*

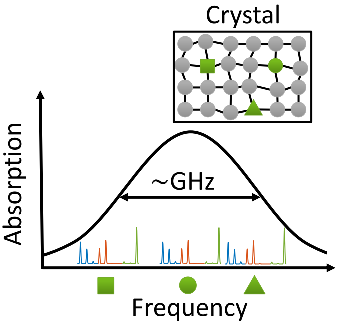

Figure 4.8. *Due to the randomness of the doping process, each dopant ion experiences slightly different electrical surroundings, as shown schematically in the crystal inset figure, where the green symbols represent dopant ions and the gray spheres represent host atoms. The transitions from ground to excited states therefore vary in the GHz range [38], leading to a wide absorption profile if the contributions of all ions in the crystal are taken into account.*

Levels	±1/2e	±3/2e	±5/2e
±1/2g	0.56	0.38	0.06
±3/2g	0.39	0.60	0.01
±5/2g	0.05	0.02	0.93

Table 4.3: Relative oscillator strengths for Pr^{3+}:Y_2SiO_5, based on experimental results in reference [49], but normalized to 1.

4.5 Pr^{3+}:Y_2SiO_5 hyperfine and inhomogeneous absorption profiles

In Pr^{3+}:Y_2SiO_5, the energy splittings of the hyperfine ground states are in the order of tens of MHz, which is much lower than the thermal fluctuations (even at 4 K). Thus, ions at equilibrium are equally likely to be in any of the three ground states. An ion in the ±1/2g can absorb light to any of the excited states and therefore has an absorption profile as seen in the blue peaks of Figure 4.7. These transition lines are in the order of kHz wide for Pr and even narrower for Eu, see Tables 4.1, 4.2, and Equation (3.24). By repopulating the Pr ion to any of the other two ground states, its absorption features shift 10.2 MHz or $10.2 + 17.3$ MHz $= 27.5$ MHz, respectively, as seen in the red and green peaks.

The nine possible transitions between the ground and excited states have different oscillator strengths, as depicted by the peak heights in Figure 4.7. The relative strengths can also be seen in Table 4.3.

Furthermore, the local crystal field surrounding a particular ion determines its exact excitation frequency through the DC Stark effect, see Section 3.4, which generally varies between ions in the GHz range [38] but depends on the doping concentration [41]. The combined absorption of all dopants in a crystal thereby creates an inhomogeneous broadening that is roughly this wide and can schematically be seen as the black line in Figure 4.8. As a result, different ions in the crystal can absorb light at a particular frequency on different transitions, thus forming nine groups of ions at each frequency, corresponding to the nine different transitions.

Ions in the crystal can therefore be selected in groups depending on their excitation wavelength. Since the individual transitions are in the order of kHz or less, whereas the inhomogeneous broadening is GHz, this results in up to millions of addressable frequency channels. This number is important for determining the capability of storing or processing information.

Using clever spectral hole burning techniques, you can relocate ions between their hyperfine ground states in order to tailor the absorption profile in various ways [49], either to create sharp narrowband absorption filters, as in Section 5.2, or more complicated structures to initialize and control qubits, as in Chapter 7.1.

Chapter 5

Light-matter interaction in rare-earth-ion-doped crystals

The previous three chapters have laid the groundwork for light-matter interaction, atoms, and properties of rare-earth-ion-doped crystals, so that this chapter can focus on the main results of Papers **I**-**IV**, all of which study effects in Pr^{3+}:Y_2SiO_5 crystals.

To start off with, Section 5.1 (Paper **I**) theoretically and intuitively discusses how the electric field polarization and absorption changes during wave propagation in birefringent crystals with an off-axis transition dipole moment.

Section 5.2 (Paper **II**) takes a more experimental approach, as the absorption of spectral holes is analyzed with the goal of achieving a narrowband spectral filter.

Such spectral holes have strong slow light effects, and by using the DC Stark effect you can shift the entire transmission window in frequency space. The next topic, covered in Section 5.3 (Paper **III**), uses these effects to frequency shift optical light pulses by changing an external voltage.

When the spectral hole is prepared slightly differently, an external voltage can instead be used to change the frequency width of the transmission window and thereby alter the group velocity that an incoming pulse experiences. This group velocity controller is discussed in Section 5.4 (Paper **IV**), where it is also used to temporally compress a probe pulse.

These last two devices, described in Sections 5.3 and 5.4, can theoretically be prepared such that they are able to operate regardless of the incidence angle and polarization of the incoming light, making them ideal for scattered light applications. Furthermore, they are controlled by only an external voltage and are thereby advantageous in weak light situations.

Finally, Section 5.5 provides an outlook for these projects.

5.1 Wave propagation in birefringent materials with off-axis absorption or gain (Paper I)

Research on rare-earth-ion-doped crystals is a diverse field with many applications, e.g., quantum memories and computing [21, 59, 60], spectral filtering [61], and as laser gain media [62]. Thus, it is useful to understand the basics of wave propagation in such birefringent absorbing materials, which is exactly what Paper **I** analyses.

In a birefringent material, such as the Y_2SiO_5 crystal, the refractive index depends on both the propagation direction and the incoming polarization. Three principal axes, referred to as D_1, D_2, and b, exist for Y_2SiO_5 and have refractive indices of $n_{D_1} = 1.7881$, $n_{D_2} = 1.809$, and $n_b = 1.7851$, respectively, for 606 nm [51].

If incoming light propagates along one of these principal axes in a pure crystal, the polarization is preserved. However, if the light has a polarization which is in between these axes, they acquire a phase retardation with respect to each other due to the difference in optical path length.

If the crystal is doped with some resonant center, such as Pr, another orientation is important: the transition dipole moment direction, $\boldsymbol{\mu}_{eg}$, since the dopants absorb light polarized in this direction. For Pr, the transition dipole moment is tilted 74.6 ± 1.9 degrees from the D_1 axis towards the D_2 axis with almost no component along b [38], see Figure 5.1(a).

To intuitively understand what happens when light propagates through a birefringent crystal with off-axis absorption, you can examine the two effects of absorption and phase retardation one at a time. This is explained below for the case of a Pr^{3+}:Y_2SiO_5 crystal.

An incoming wave, with electric field $\mathbf{E}_{\text{in}}$, propagates along b with its polarization along D_2, as shown in Figure 5.1(a). It polarizes the material along $\boldsymbol{\mu}_{eg}$, which can be seen as an induced electric field, $\mathbf{E}_{\text{P}}$, that is out of phase with the incoming polarization. The two fields interfere and the resultant field, $\mathbf{E}_{\text{res}}$, in Figure 5.1(b), is tilted away from the transition dipole moment direction.

To examine the effects of birefringence, it is easier to split the resultant field into its components along D_1 and D_2, see Figure 5.1(c). Due to the difference in refractive index, the phases of these polarization components evolve differently as the wave propagates through the crystal, see Figure 5.1(d)-(e).

From the effects explained in Figure 5.1, it is clear that the incoming polarization is not generally maintained during propagation, even if it is initially polarized along a principal axis. However, two steady state polarizations exist, but only the solution with the lowest absorption (or highest gain) is stable. Generally speaking,

(a) Input polarization (b) Absorption

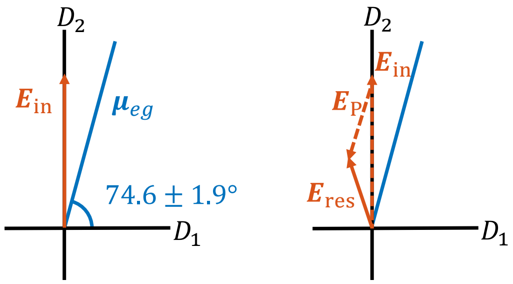

(c) Projection on D_1, D_2 (d) Propagation (e) Propagation

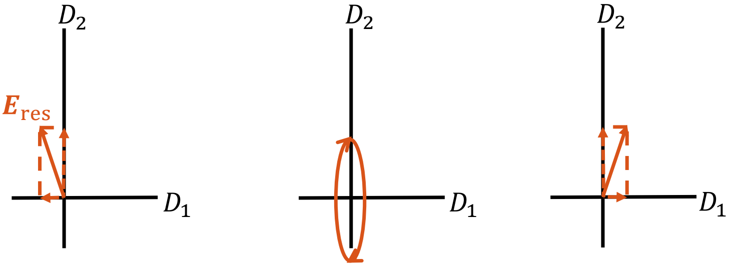

Figure 5.1. *An intuitive explanation of absorption in (a)-(b) and propagation through a birefringent crystal in (c)-(e). (a) An incoming electric field, $\mathbf{E}_{in}$, polarized along D_2 is shown together with the transition dipole moment, $\boldsymbol{\mu}_{eg}$. (b) The material is polarized along the transition dipole moment direction, which can be seen as an electric field vector $\mathbf{E}_P$ that is out of phase with the incoming field. This causes a decrease and rotation of the incoming field, resulting in $\mathbf{E}_{res}$. (c) The field is decomposed into components along D_1 and D_2. (d) Due to the difference in refractive index for the principal axes, the electric field polarization changes from linear to elliptical. (e) Further propagation leads once more to linear polarization, this time with a different polarization angle.*

they are elliptically polarized and differ only by a 90 degree rotation in the D_1, D_2 plane (assuming the transition dipole moment lies in this plane). If the incoming polarization matches one of these steady state solutions, it does not change during propagation, similar to the principal axis polarizations in the pure crystal case.

The ellipticity and direction of these polarizations depend on the ratio seen below:

$$R = \frac{n_{D_2}^2 - n_{D_1}^2}{\chi_{abs}} \tag{5.1}$$

where χ_{abs} is the electric susceptibility connected to the Pr absorption.

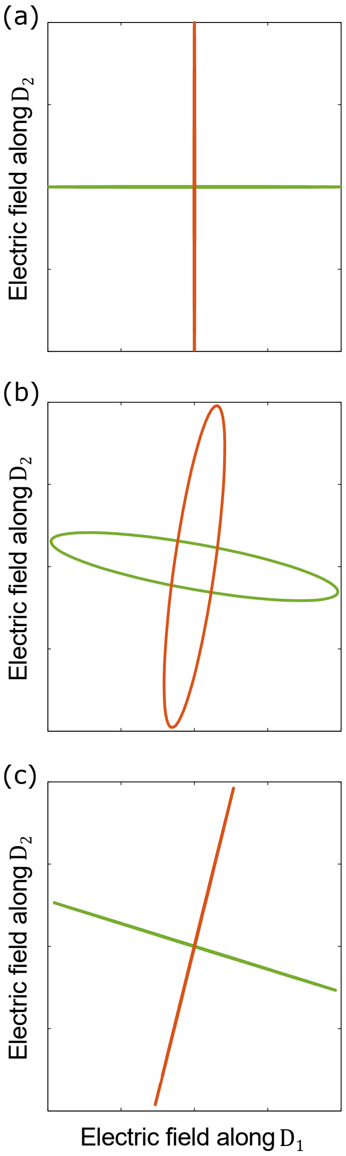

Figure 5.2. *The stable (green) and unstable (red) polarization steady state solutions are shown for different values of* R *given in Equation (5.1). (a)* $R \approx 85$ *(i.e.,* $R \gg 1$*), which is the case for* Pr^{3+}:Y_2SiO_5*. In (b)* $R \approx 1$ *and (c)* $R \ll 1$*.*

Assuming $n_{D_2} \approx n_{D_1} \approx n_{\mathrm{bg}}$, where n_{bg} is a background refractive index, you can write $n_{D_2}^2 - n_{D_1}^2 = (n_{D_2} + n_{D_1})(n_{D_2} - n_{D_1}) \approx 2n_{bg}\Delta n$. Thus, R is approximately the ratio of the rate of accumulating phase retardation, Δn, and the absorption, χ_{abs}.

If $R \gg 1$, phase retardation overshadows absorption, which makes all polarizations that are symmetric along the crystal axes equivalent, since they evolve into each other due to the effects explained in Figure 5.1(c)-(e). As a result, the polarization steady states lie along D_1 and D_2. This is the case for Pr^{3+}:$\mathrm{Y_2SiO_5}$, where $R \approx 85$ ($\chi_{abs} = [8.82 \pm 0.8] \cdot 10^{-4}$, based on $\alpha_{D_1} = 3.6 \pm 0.5$ cm^{-1} and $\alpha_{D_2} = 47 \pm 5$ cm^{-1} [38]), as can be seen in Figure 5.2(a).

If the ratio is at the other extreme, $R \ll 1$, absorption dominates and any phase retardation can be ignored, which leads to one steady state along the transition dipole moment with high absorption and another along the orthogonal direction with very low absorption, see Figure 5.2(c).

If $R \approx 1$, both effects are important and the steady state solutions are more elliptical, lying between the transition dipole moment and the principal axes, as seen in Figure 5.2(b).

As mentioned previously, only the steady state solution with the lowest absorption (highest gain) is stable. When light propagates through a crystal with an incoming polarization that differs from these solutions, the polarization changes and eventually reaches the stable steady state solution. In any practical situation, irregularities and impurities cause the polarization to shift toward the stable solution even if the initial polarization is perfectly aligned with the unstable steady state solution.

Based on the explanation in Figure 5.1(a)-(b), an electric field component along D_2 induces a small component along D_1 when it is absorbed along a tilted transition dipole moment, and vice versa. During propagation, both the D_1 and D_2 components are absorbed, generally with different absorption coefficients. For the steady state solutions, however, the ratio of the two polarization components are such that the difference between the absorption coefficients are compensated for by the induced field and the polarization remains the same during propagation.

Three important conclusions can be drawn from these results. First, the maximum absorption direction depends on the ratio R and might not be along the transition dipole moment, but along the principal axis D_2, as in the case of Pr^{3+}:$\mathrm{Y_2SiO_5}$ described above.

Second, since the polarization of incoming light shifts during propagation, the absorption coefficient α also tends to vary with distance. For example, in Pr^{3+}:$\mathrm{Y_2SiO_5}$ the stable steady state lies close to the D_1 axis since it has the lowest absorption, and even if the initial polarization is perfectly aligned with D_2, the light experiences only the high absorption coefficient α_{D_2} until it has propagated approximately 5.4 mm, after which the stable steady state is reached and the field starts to decay with the low absorption coefficient α_{D_1}.

Third, even if the incoming polarization is perfectly aligned with D_2, it almost immediately creates a D_1 component due to the effects explained in Figure 5.1(a)-(b). Thus, there is little reason to have an incoming polarization purity that is better than the ratio of this created D_1 component compared to the initial D_2. For Pr^{3+}:Y_2SiO_5, this ratio is in the order of $\frac{I_{D_1}}{I_{D_2}} = 10^{-5}$, where I_x denotes the initial intensity along direction x, and corresponds to a polarization angle precision of approximately 0.17 degrees. In other words, a polarizer with a suppression of 10^5 is enough to achieve the longest propagation distance with maximum absorption.

For information about how the simulations were performed, see Paper **I**.

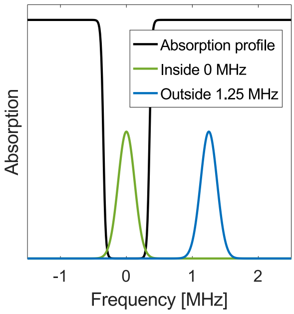

Figure 5.3. *A schematic view of a narrowband spectral filter is seen in black. The goal is to have high transmission for the pulse inside the spectral hole, the green line, whereas the pulse detuned by* 1.25 *MHz relative to the center of the hole, the blue line, should experience strong absorption.*

5.2 Development and characterization of high suppression and high étendue narrowband spectral filters (Paper II)

Narrowband rare-earth spectral filters based on hole burning have a wide range of applications, including quantum memories [56], self-filtering of laser frequencies [63], and ultrasound optical tomography (UOT) [64]. Paper **II** address the critical issues in constructing such high suppression filters, and targets mainly the application of UOT, which is briefly described in the paper and more information can be obtained from references [61, 64].

The filter is illustrated in Figure 5.3, where the black curve shows the absorption coefficient of the filter as a function of frequency, i.e., the spectral hole. The green and blue lines represent the frequency distributions of two pulses located 0 MHz and 1.25 MHz, detuned from the center of the hole, respectively. The goal of the spectral filter is for the pulse inside the spectral hole to have high transmission and low distortion, whereas the pulse located outside the hole should have high absorption. Since the two pulses are separated by only a few MHz, the requirements for the hole edge sharpness and homogeneity throughout the crystal are stringent.

The setup used for the experiments is shown in Figure 5.4. The light comes from a stabilized Coherent 699-21 ring dye laser and can be frequency tuned by an acousto-optic modulator in a double pass configuration. A beam splitter reflects a small portion of the light to a reference detector, PD1 (Thorlabs PDB150A), but the main part is transmitted through a lambda-half plate and a polarizer before it reaches the crystal that is situated in the cryostat. A second polarizer is used to probe the polarization of the transmitted light, after which two different detectors, PD2 (Thorlabs

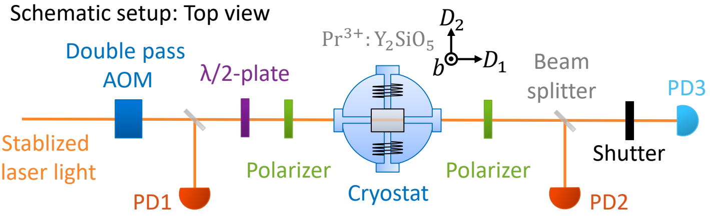

Figure 5.4. *Overview of the experimental setup, see the main text for more information.*

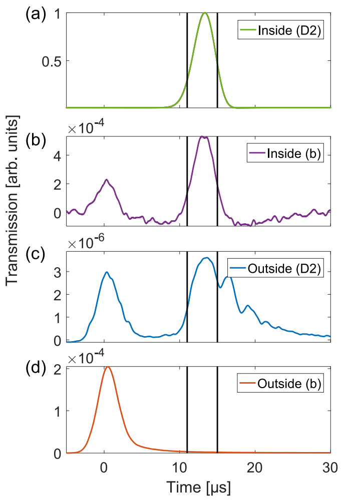

Figure 5.5. *The graphs show the experimental transmission inside and outside the spectral filter for 3 µs full width at half maximum (FWHM) probe pulses, averaged 25 times. The D_2 and b component of transmitted light inside the spectral filter are shown in (a) and (b), respectively. (c) Transmitted D_2 light when probing the spectral filter in the high absorption area 1.25 MHz detuned from the center of the hole. (d) Same as (c) but shows the b component of the transmitted light instead. The black lines show the time gating used for calculating the suppression values, such as those shown in Figures 5.6 and 5.7.*

PDB150A) and PD3 (Hamamatsu PMT R943-02), are used to detect it. PD2 is used to analyze the strong probe pulse transmitted through the spectral hole, whereas PD3 is used to detect the weak light transmitted outside the hole. For more detailed information about the setup, see Appendix A.

A 10 mm thick 0.05% doped Pr^{3+}:Y_2SiO_5 crystal with principal axis orientation, as seen in Figure 5.4, was used for these experiments. In order to increase the lifetime of the spectral hole, a 10 mT magnetic field was applied across the D_2 axis.

Typical results for the filter when propagating inside/outside the spectral hole can be seen in Figure 5.5. All pulses were sent in at time 0 with a D_2 polarization and propagated along the D_1 crystal axis.

In Figure 5.5(a), the transmission inside the spectral hole is shown when the polarizer located after the crystal was aligned with D_2. Due to the large dispersion in the hole, the light slows down and exits after roughly 13 µs (see slow light description in Section 2.2.1). All graphs in Figure 5.5 are normalized to the same scale, where the maximum transmission inside the spectral hole, seen in Figure 5.5(a), is 1.

The transmitted b component, shown in Figure 5.5(b), is much lower, and its magnitude is relatively consistent with the suppression of the polarizer, 10^5, considering that the light propagates through the cryostat windows and is partly reflected at the crystal surface, both of which may reduce the extinction ratio of the polarization that reaches the crystal. Moreover, a slight misalignment of the crystal principal axes with the polarizers can explain why the delayed b component, which is assumed to be due to the outgoing cryostat window and the polarizer after the cryostat, is larger than the non-delayed component.

The D_2 and b components of the transmitted light when propagating outside the spectral hole can be seen in Figures 5.5(c) and (d), respectively. The b component is not delayed, since the absorption coefficient is almost zero along that direction and the magnitude is in the same order as seen in Figure 5.5(b), indicating that it comes from an impure polarization that reaches the crystal, as discussed above.

Fortunately, a polarizer that is aligned with D_2 and is located after the crystal can attenuate the b component of the transmitted light. Thus, this b component does not reduce the potential of the spectral filter (remember that the light transmitted through the spectral hole is oriented almost exclusively along D_2 such that the polarizer after the crystal does not affect it). Alternatively, you can use two stacked crystals with their axes rotated 90 degrees relative to one another in order to achieve high absorption, regardless of incoming polarization [65].

The results of Figure 5.5(c) show that the D_2 light has two parts: one that is slowed down similarly to the transmission inside the spectral hole shown in Figure 5.5(a), and one part that is not. The slow part is assumed to be light leaking through the spectral hole due to an overlap of its frequency components with the spectral hole. This indicates that the hole edges are not as good as illustrated in Figure 5.3 or that the frequency distribution of the pulse is not as narrow. Using time gating, the light that is not delayed can be neglected when evaluating the spectral filter suppression, which is calculated by comparing the total transmission between the two black bars, located at 11 µs and 15 µs, for the cases of being inside or outside the spectral hole.

After a spectral hole was created, four sets of 25 probe pulses each were sent into the crystal, the first and third inside the hole and the second and fourth outside. When calculating the suppression, two values were obtained by comparing the first two sets and last two sets, respectively. This was done in order to evaluate any deterioration of the hole, and thus the suppression, as it was used.

In Paper **II**, the application discussed is UOT, where the pulse duration and frequency separation are not yet fixed. Therefore, the suppression of the filter was examined as a function of the incoming pulse full width at half maximum (FWHM) duration, as seen in Figure 5.6, where the overlap of the two suppression curves, calculated as described in the previous paragraphs, indicates that the hole does not deteriorate. Since the frequency width and the pulse duration are inversely proportional to each other, a short pulse has poorer suppression due to an increased frequency overlap between the spectral hole and the incoming pulse. However, a shorter pulse is preferred in UOT such that a compromise of 3 µs long pulses was chosen. In these experiments, the pulse propagating outside the spectral hole was detuned 1 MHz compared to the center.

The suppression was also measured as a function of detuning for a fixed FWHM duration of 3 µs, as seen in Figure 5.7. You can see that the suppression is almost constant as long as the detuning is larger than 1.25 MHz, where a suppression of 53.4±0.7

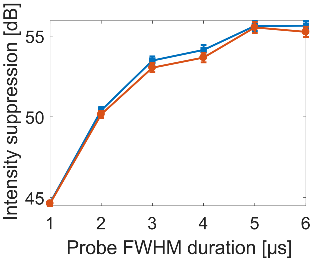

Figure 5.6. *The suppression in dB as a function of the probe FWHM duration. The suppression is calculated by comparing the D_2 transmission for inside and outside probes, time gated between 11 μs and 15 μs, shown as black lines in the example given in Figure 5.5. The two data sets correspond to experiments performed in quick succession using the same spectral hole. The markers show the mean of 25 measurements and the error bars show one standard error of the mean.*

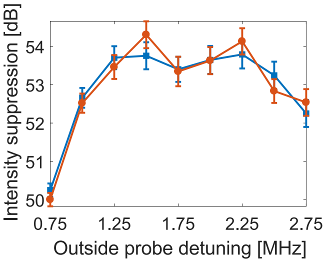

Figure 5.7. *The suppression in dB as a function of the outside probe detuning. For more information about the data treatment, see the caption of Figure 5.6.*

dB is achieved. Note also that a suppression of 63.2 ± 0.6 dB was obtained if the detuning was increased to 10.2 MHz, which agrees well with previous results at that detuning [56]. Such large frequency shifts are not suitable, however, for the application of UOT.

The main advantage of these filters is their insensitivity to the incoming beam direction, as simulated and discussed further in Paper **II**. This is especially important for the application of UOT where a simple Fabry-Pérot cavity, which can act as a high suppression narrowband filter, does not cover enough spatial modes to be useful.

To summarize: in Paper **II**, a narrowband spectral filter was created and analyzed. It achieved a relative suppression of 53.4 ± 0.7 dB for two 3 µs long pulses separated only by 1.25 MHz.

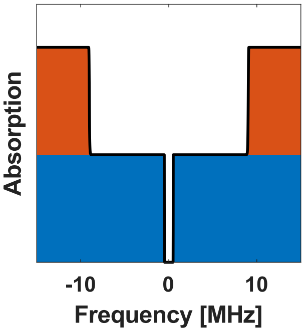

Figure 5.8. *Schematic view of the absorption structure. The blue areas represent ions that shift toward higher frequencies if a positive voltage is applied across the crystal. The red ions shift in the opposite direction.*

5.3 Slow-light-based optical frequency shifter (Paper **III**)

The DC Stark effect, explained in Section 3.4, can be used to alter the absorption profile of a material, as examined in Papers **III** and **IV**. This section covers Paper **III**, which uses the absorption profile shown in Figure 5.8 to frequency shift incoming probe pulses by controlling an external electric voltage. See the article for a detailed description of the structure preparation.

The DC Stark effect causes the blue and red ions to shift their resonant frequencies in opposite directions. If a positive voltage is applied, the blue ions shift to higher frequencies and vice versa for the red ions. Thus, the spectral hole in the blue absorption shifts toward higher frequencies while keeping the same width as long as the shift is small enough that the red absorption does not overlap with the hole. Experimental results of the transmission window movement can be seen in Figure 5.9(a) for five different voltage settings.

When a light pulse propagates through the spectral hole, most of its energy is stored in the nearby ions, as described in Section 2.2.2. This leads to a greatly reduced group velocity compared to the speed of light in vacuum, making it possible to store the entire light pulse inside the crystal. In these experiments, a 1 µs pulse propagated through a 10 mm thick 0.05% doped Pr^{3+}:Y_2SiO_5 crystal.

If an external DC electric field is applied when the pulse is still inside the crystal, the ions that store the energy of the pulse shift their resonance frequencies as described above, and so does the light they re-emit. Denoting the frequency of the incoming light pulse as 0 MHz on a relative scale, the experimental results of the outgoing pulse frequencies can be seen in the solid lines of Figure 5.9(b).

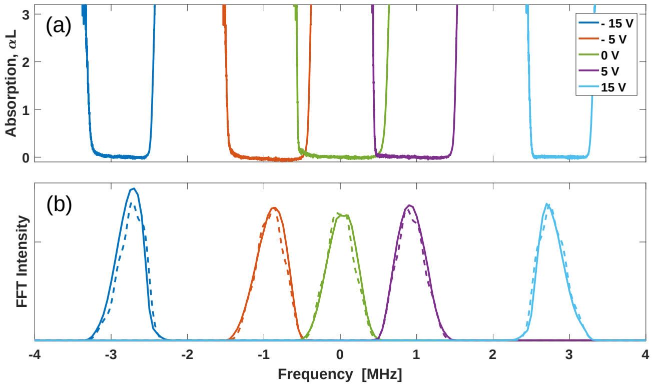

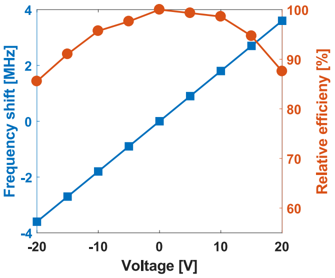

Figure 5.11. *Frequency shift and relative efficiency as a function of applied voltage across the crystal.*

Figure 5.9. *(a) Experimental αL (absorption coefficient multiplied by crystal length) as a function of frequency, shown for five different voltages applied across the crystal. (b) Using heterodyne detection, the Fourier transform intensity of the transmitted probe light is examined. The solid and dashed lines show the experimental and Maxwell-Bloch simulation results, respectively. As can be seen, the probe frequency shifts together with the spectral hole.*

The dashed lines in the same figure are the results of a Maxwell-Bloch simulation and coincide well with the experimental results. Furthermore, the simulations can show the energy distribution of the ions during propagation, as in Figure 5.10(a)-(b), right before and after applying the external electric voltage, respectively. The spectral window is approximately 1 MHz wide, and the energy is stored mostly in the ions just outside the hole. More detailed information about how the simulations were performed can be found in Paper **III**.

Finally, experimental results of the frequency shift and relative efficiency are shown together as a function of the applied voltage in Figure 5.11. The linear behavior of the frequency shift is expected, since the DC Stark effect linearly shifts the transition frequencies. Furthermore, the Stark coefficient in the simulations that yielded the best overlap with the experimental results was 116.7 kHz/(V/cm), which agrees well with the literature value of $\approx$ 112 kHz/(V/cm) [55, 57].

The efficiency drop for large shifts might have several explanations. For example, a misalignment of the electric field to the symmetry axis of the static dipole moment, see Figure 4.6 in Section 4.3, or inhomogeneities in the applied electric field, can cause ions to move differently and reduce the coherent reemission of light. Alternatively, some red ions in Figure 5.8 move closer to the spectral hole, thereby increasing the overall absorption.

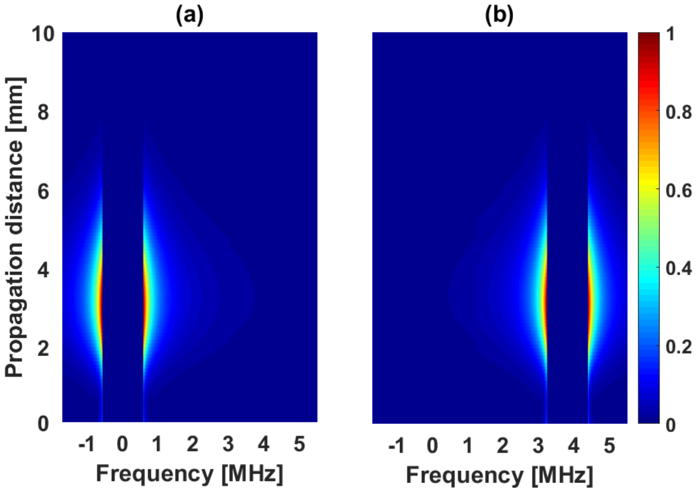

Figure 5.10. *Simulation results of the ion excitation as a function frequency and propagation distance when a 1 μs probe pulse propagates through a spectral hole initially centered around 0 MHz with a width of a little over 1 MHz. Red describes the maximum excitation in the material, whereas dark blue represents zero excitation. Figure (a) is just before an instantaneous frequency shift of the ions is applied, and (b) is right after the shift.*

In conclusion, Paper **III** uses the strong slow light effect of a narrowband transmission window and the DC Stark effect to frequency shift optical light using a voltage source as a controller. In experiments, up to ±4 MHz shifts were achieved with efficiencies above 85%. The technique can potentially be improved to be limited only by the breakdown voltage of the crystal (at least 1 MV/cm [66]), which would lead to frequency shifts in the order of 100 GHz.

Furthermore, it is argued that these frequency shifters can be constructed to have a solid acceptance angle close to 2π and work for any incoming polarization and thus also work for scattered light. These arguments are based on related works [61, 65].

These devices should be particularly suitable in weak light situations due to the fact that the shifters are controlled by an external voltage source and not any additional light pulses.

5.4 Using electric fields for pulse compression and group-velocity control (Paper IV)

In this section, which describes the results of Paper **IV**, the DC Stark effect is once more examined, but now for the absorption

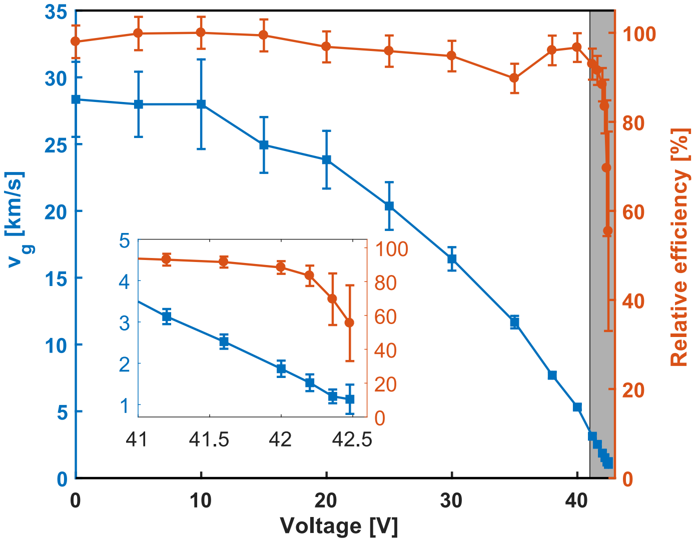

Figure 5.14. *Shows the group velocity and relative efficiency as a function of the applied voltage. The inset shows a zoomed in view of the highest voltages, i.e., the narrowest holes (gray area).*

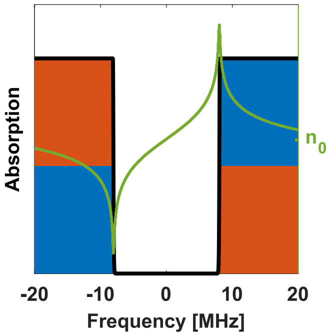

Figure 5.12. *A schematic view of the absorption profile and the corresponding refractive index curve when no external electric voltage is applied. The dispersion is relatively low, and the group velocity is around 30 km/s. Blue ions shift toward higher frequencies if a positive voltage is applied, and vice versa for red ions.*

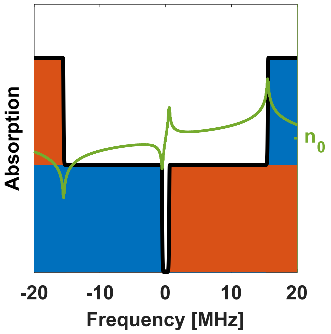

Figure 5.13. *The 16 MHz wide absorption structure in Figure 5.12 changes into the 1 MHz hole seen above when an external voltage of 40 V is applied across the crystal, creating a strong dispersion for the narrow spectral hole with a group velocity of around 5 km/s.*

profile seen in Figure 5.12, and used to alter the group velocity or temporarily compress probe pulses.

Similarly as described in Section 5.3, blue ions shift to higher frequencies when a positive external voltage is applied, whereas red ions move to lower frequencies. If 40 V is applied across the crystal, the absorption profile changes to reduce the width of the spectral hole from 16 MHz to 1 MHz, as seen in Figure 5.13.

The narrower hole has a much steeper dispersion curve, which can be seen when comparing the refractive index curves, the solid green lines, in Figures 5.12 and 5.13, leading to a lower group velocity. See Section 2.2.1 for more details.

By choosing an external voltage and thus a spectral hole width before sending a probe pulse into the crystal, you can choose the group velocity with which it should propagate through the transmission window, see Equation (2.18).

In Paper **IV**, a 6 mm×10 mm×10 mm (crystal axes $b \times D_1 \times D_2$) Y_2SiO_5 crystal doped with 0.05% Pr was used to control the group velocity of pulses in the manner described above.

The experimental results are shown in Figure 5.14, where the blue line represents the group velocity as a function of the applied voltage, which relates to the spectral hole width, where lower voltages mean a wider hole. The red curve is the relative efficiency,

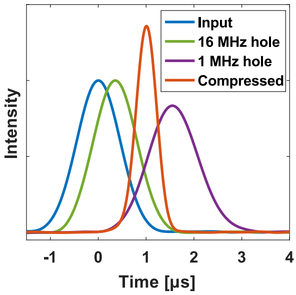

Figure 5.15. *The blue line shows a reference of the input pulse, centered at 0 μs. If it propagates through a 16 MHz wide spectral hole, it is delayed only slightly, as seen in the green line. For a 1 MHz hole, the group velocity is much lower and the delay is longer, see the purple line. If the hole is initially narrow but quickly widens when the pulse is completely inside the crystal, the pulse is compressed, as seen in the red line.*

i.e., the transmission of the pulse normalized such that the maximum is 1. The data shown is averaged 150 times and the bars correspond to one standard deviation.

The device can alter the group velocity of the probe from 30 km/s to 1.5 km/s, corresponding to voltages of 0 V and 42.2 V, respectively, while having a relative efficiency above 80%. The slowest speed recorded was almost 1 km/s but with a relative efficiency of around 50%.

The reasons for the efficiency drop are the same as those discussed in Section 5.3: inhomogeneities in the applied electric field, misalignment of the field with the symmetry axis of the static dipole moment, and increased absorption of the light as the hole narrows.

In Paper **IV** it is argued that the tunability of the controller can be extended from the current factor of 20 to around 600 if, for example, Er^{3+}:$\mathrm{Y_2SiO_5}$ is used where the maximum width of a spectral hole is 575 MHz (based on the hyperfine splittings from [67]) instead of the 18 MHz for Pr^{3+}:$\mathrm{Y_2SiO_5}$.

The current device can also be used for temporal pulse shaping if the external voltage is changed when the pulse is still propagating inside the crystal.

To demonstrate this, a 16 MHz wide spectral hole was created as in Figure 5.12 and a 1 µs long pulse was sent into the crystal at time $t = 0$, a reference of which is shown in the blue line of Figure 5.15. When no voltage was applied, the transmission window remained wide and the pulse arrived at the delayed time $\tau_1 = 350$ ns, as shown in the green trace. This corresponds to a high group velocity of $v_{g1} = L/\tau_1 \approx 29$ km/s, where $L = 10$ mm is the crystal length in the propagation direction.

When a constant voltage of 40 V was used instead, the hole was approximately 1 MHz wide and the pulse became further delayed, as shown in the purple line. It arrived at time $\tau_2 = 1.54$ µs, corresponding to a group velocity of $v_{g2} = L/\tau_2 \approx 6.5$ km/s. At this low group velocity, the 1 µs light pulse was strongly compressed from a FWHM length of about 300 m in a vacuum to 6.5 mm in the crystal such that almost the entire pulse was accommodated inside the crystal at one time.

In a final experiment, the external voltage was rapidly switched off from 40 V to 0 V just as the pulse was about to exit the crystal. The first part of the pulse still went through the entire crystal with group velocity v_{g2}, whereas the last part initially traveled at speed v_{g2}, but traveled the remaining distance at speed $v_{g1} \gg v_{g2}$ after the external field changed and altered the absorption profile. Thus, the last part of the pulse spent a much shorter time inside the crystal and the entire pulse was compressed, as shown in the red trace of Figure 5.15.

Although these initial results show that pulse shaping is possible, the compression was only a factor of about 2 and the efficiency, calculated as the area under the red curve relative to the area of the green trace in Figure 5.15, was only 66%. In Paper **IV**, however, Maxwell-Bloch simulations were performed and compared to the experimental results, showing that larger compressions and higher efficiencies should be possible.

As a recap of Paper **IV**: the group velocity of a pulse was tuned by a factor of 20 while keeping the efficiency above 80%; initial results of pulse reshaping were performed, showing that pulse compression is possible by altering the external voltage over the crystal as the pulse propagates inside it; these devices can be used advantageously in weak light situations since they do not require any other light fields and are controlled solely by the external voltage; and if two crossed crystals are used, they should theoretically have a solid acceptance angle close to 2π [61] and work for all incoming polarizations [65].

5.5 Outlook of projects

This last section briefly reviews the current or potential follow-ups to the projects discussed in this chapter.

The wave propagation model presented and used in Papers **I** and **II** is not currently being expanded any further. However, the ability to model light propagation in materials remains of interest to our group in the ultrasound optical tomography (UOT) project, where the focus is on absorbing and scattering materials [64].

The Pr^{3+}:Y_2SiO_5 spectral filter shown in Paper **II** will be used in preliminary experiments for UOT when measuring on tissue phantoms. More effort is currently being devoted to find other materials for narrowband spectral filtering in the tissue optical window, also for the application of UOT. These filters should preferably have similar or better properties than the one discussed in Section 5.2, but at a wavelength more suitable for penetrating into the human body.

The UOT project may one day use the frequency shifter scheme presented in Paper **III** when taking the next step of phase conjugating and amplifying the scattered light signal in an attempt to refocus it back into the human body and achieve a lasing effect to improve the penetration depth and the signal-to-background ratio.

The group-velocity controller project, Paper **IV**, is not currently being continued or improved upon, but our group has an ongoing general interest in slow light applications.

Chapter 6

A brief overview of quantum computation

This chapter shifts focus toward quantum computing by providing an overview of the field, and is followed by Chapter 7, which presents the progress achieved by our group in the rare-earth quantum computing field, especially projects where I have been involved.

In Section 6.1 a justification for pursuing quantum computers is offered. Section 6.2 describes the DiVincenzo criteria, which are commonly accepted requirements that a fully functional quantum computer needs to meet.

Lastly, the Quantum Technologies Roadmap as a part of the European Commission Quantum Technology Flapship is discussed in Section 6.3.

6.1 Pursuing quantum computing

In a speech at a conference in May 1981 at MIT, Richard Feynman presented the idea that simulating the evolution of a quantum system on a classical computer in an efficient way appeared impossible and urged the world to build a quantum computer, *"... nature isn't classical, dammit, and if you want to make a simulation of nature, you'd better make it quantum mechanical, and by golly it's a wonderful problem, because it doesn't look so easy"* [68]. The conjecture that any local quantum system can be simulated on a quantum computer was proven by Seth Lloyd in 1996 [69].

As always, scientific progress is not due to one person alone and other scientists made important contributions before Feynman's famous speech in 1981. R. P. Poplavskii showed in 1975 the infeasibility of using a classical computer to simulate quantum systems [70], and Y. Manin proposed in 1980 the idea of a quantum computer [71]. A relatively thorough and expanding timeline of the quantum computation field is available on Wikipedia [72].

Nevertheless, the field of quantum computing had been initiated. With the prospect of efficiently simulating quantum systems and discoveries of Shor's algorithm, which provides exponential speedup compared to classical ones when factoring large integers and might theoretically break many present-day encryptions [73]; Grover's algorithm, which provides a quadratic speedup for the common problem of brute force searching a database [74]; and the quantum annealing algorithm, which was shown by Hidetoshi Nishimori et al. to outperform classical simulated annealing [75]; the field of quantum computing became a worldwide interest, which includes leading corporations like IBM [76], Google [77], Microsoft [78], and Intel [79], not to mention new businesses for the sole purpose of quantum computing, such as D-wave [80].

The benefits of such quantum simulators and algorithms, in addition to the prospect of even more discoveries, both fundamental and application-based, and an overall gain in human knowledge, propel the field forward and make it a worthwhile investment for scientists and companies alike.

6.2 DiVincenzo's criteria

Back in 1996 [81], DiVincenzo put forth the idea of minimal requirements for creating a quantum computer. In 2000, he published such a list, which contained five thoroughly evaluated requirements, later referred to as the DiVincenzo criteria [82]. This list appears below as presented in reference [82], where the last two points are requirements for quantum communication and included here for purposes of completeness:

(i) A scalable physical system with well characterized qubits

(ii) The ability to initialize the state of the qubits to a simple fiducial state, such as $|000...\rangle$

(iii) Long relevant decoherence times, much longer than the gate operation time

(iv) A "universal" set of quantum gates

(v) A qubit-specific measurement capability

(vi) The ability to interconvert stationary and flying qubits

(vii) The ability to faithfully transmit flying qubits between specified locations

These criteria will be discussed more in Section 7.7 with regard to the progress of rare-earth quantum computing by our group.

6.3 Quantum Technologies Roadmap

This section discusses the Quantum Technologies Roadmap [83] provided by the European Commission in its Quantum Technology Flagship [84], which is a €1 billion investment in research and applications in the field. The document lists six topics: Quantum Computation; Quantum Communication; Quantum Simulation; Quantum Information Theory; Quantum Metrology, Sensing and Imaging; and Quantum Control. The focus of this section is the computation part.

Below is a general list of future directions as they appear in the Quantum Technologies Roadmap (2015 edition of the European roadmap for Quantum Information Processing and Communication) [83]:

(i) Further development of all current technologies to understand their limitations and find ways around them.

(ii) Assessment of the capabilities of different technologies for being scaled up.

(iii) Optimization of the performance of error correcting codes, by both increasing the error threshold and decreasing the overhead of required qubits.

(iv) Investigation of new ways of performing quantum computation, in particular based on self-correcting codes (as they appear in topological systems).

(v) Development of new quantum algorithms and search for problems where quantum computers will be required.

(vi) Development of quantum complexity theory and its application to many body physics.

(vii) Building interfaces between quantum computers and communication systems.

(viii) Development of quantum-proof cryptography to achieve forward-in-time security against possible future decryption (by quantum computers) of encrypted stored data.

As can be seen, the list is comprehensive in its goals but purposely vague about the specific experimental platform. The first point even specifically requests further investigation into all current technologies.

Reference [83] explains some experimental approaches with state-of-the-art (2015) updates on progress and challenges, as well as short, medium, and long-term goals. The topics discussed are trapped ions, quantum computing with linear optics, superconducting circuits, and electronic semiconductor qubits, as well as impurity spins in solids and single molecular clusters, which include rare-earth-ion-doped crystals. Anyone who wants an experimental overview of the quantum computation field would therefore do well to read this roadmap or an updated version of it.

Chapter 7

Quantum computation in rare-earth-ion-doped crystals

This chapter describes the quantum computation progress achieved by our group at Lund University, particularly the projects I have been involved with.

First, Section 7.1 describes how an ensemble qubit is initialized in Pr^{3+}:Y_2SiO_5, the material that is used for most discussions throughout this chapter and whose relevant energy levels can be seen in Figure 7.1, now employing quantum computation notations for the states.

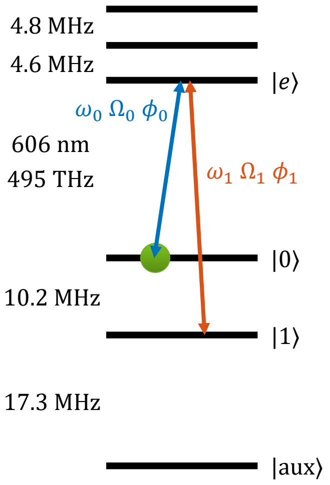

Figure 7.1. *Hyperfine states for* Pr^{3+}:Y_2SiO_5 *using the quantum computation notations for the levels. The arrows indicate two possible electromagnetic fields with frequencies* ω_0 *and* ω_1*, and complex Rabi frequencies* $\Omega_0 e^{i\phi_0}$ *and* $\Omega_1 e^{i\phi_1}$*, respectively.*

Single qubit gates are discussed in Section 7.2, where Section 7.2.1 presents complex hyperbolic secant pulses (sechyp pulses for short), using a single color/frequency, and Section 7.2.2 goes through two-color pulses. Finally, Section 7.2.3 (Paper **V**) uses electromagnetically induced transparency (EIT), i.e., two-color pulses, in order to perform a spin echo sequence.

The pulses described so far can be used to perform any single qubit operation. Thus, the next step is two-qubit gates, which are discussed in Section 7.3 (Paper **VI**), still using ensemble qubits in a Pr^{3+}:Y_2SiO_5 crystal.

Due to poor scaling properties of ensemble qubits, however, a high-fidelity single ion scheme is presented in Section 7.4 (Paper **VII**), where a dedicated readout ion is also doped into the crystal together with the qubit ion, but with a much lower concentration. Two possible readout ions are discussed: neodymium (Nd) in a micro-cavity [85, 86], and weakly doped cerium (Ce) that is detected using a confocal microscope setup [87]. Although both methods are still under investigation, some results of the cerium approach can be seen in Section 7.5 (Paper **VIII**).

The confocal microscope setup has also been used to investigate Eu^{3+}:Y_2O_3 nanocrystals, a paper on which is currently under preparation, and is briefly discussed in Section 7.6.

In Section 7.7, the progress of the single ion quantum computing scheme is evaluated based on the DiVincenzo criteria presented in Section 6.2. Lastly, Section 7.8 discusses the outlook of the quantum computing projects of our group.

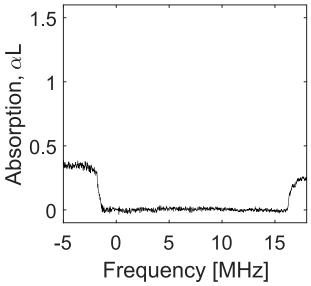

Figure 7.2. *Absorbing ions are removed from a frequency region in preparation for the qubit initialization.*

7.1 Qubit initialization

The inhomogeneous broadening in rare-earth-ion-doped crystals renders it impossible to target only a specific transition, such as $|0\rangle \to |e\rangle$, with a laser pulse without preparing the sample first. The reason is that at each specific light frequency, nine groups of ions are resonant, all at different transitions due to the DC Stark shift induced by the spatially varying crystal field, see Section 4.5.

The first step in initializing a qubit is to create a wide region where no absorbing ions exist. This is done by repeatedly sending in light pulses that scan the targeted area, exciting and optically pumping ions away from the region [39, 88]. The resulting spectral pit can be seen in Figure 7.2 and is the largest possible region that can be completely emptied in Pr^{3+}:Y_2SiO_5 (set by the hyperfine splittings [49]).

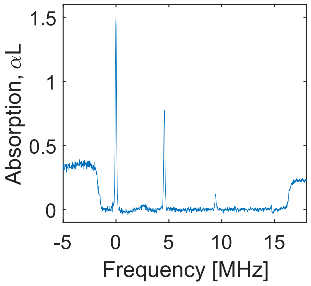

Figure 7.3. *The qubit has been prepared in the $|0\rangle$ state. 0 MHz corresponds to the $|0\rangle \to |e\rangle$ transition shown in Figure 7.1.*

A narrow absorption peak, ∼170 kHz wide, is then created by burning back some ions into the pit. This is done in a careful manner, and after cleaning up unwanted absorption, the remaining peaks inside the pit all correspond to ions in the $|0\rangle$ state and represent our ensemble qubit. The absorption of the ions to the three excited states can be seen in Figure 7.3, corresponding to the blue spectrum in Figure 4.7. The peak heights are proportional to the relative oscillator strengths of the different transitions, as seen in Table 4.3.

For the sake of completeness, the absorption spectrum when the qubit is in state $|1\rangle$ is shown in Figure 7.4, corresponding to the red part of Figure 4.7. Only the transitions to the two lowest excited states can be seen, since the last transition lies outside the spectral pit. The qubit has been transferred from $|0\rangle$ via $|e\rangle$ to $|1\rangle$ using two sechyp pulses that are described in Section 7.2.1.

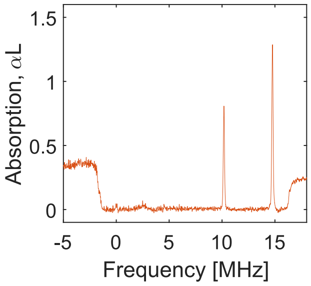

Figure 7.4. *The qubit has been transfered to the $|1\rangle$ state by using two consecutive sechyp pulses.*

7.2 Single qubit gate operations

After initializing the qubit, the next step is to perform simple gate operations. Section 7.2.1 uses one-color pulses, i.e., pulses with only one frequency at a time, to perform transfers between any ground and excited state. Two-color pulses, which can be used to do arbitrary single qubit operations in a robust manner, are then described in Section 7.2.2. Finally, an all-optical nuclear spin echo technique is discussed in Section 7.2.3 (Paper **V**).

7.2.1 One-color sechyp pulses

Since square pulses are very sensitive to Rabi frequency fluctuations, i.e., variations in laser intensity, sechyp pulses are often used instead. In such pulses, the intensity and frequency of the light change as a function of time [89–91], and can be described by the complex Rabi frequency $\Omega(t)$;

$$\Omega(t) = \Omega_0 \text{sech}(\beta(t - t_0))^{1-i\mu} \tag{7.1}$$

where Ω_0 is the maximum Rabi frequency, t_0 is the center of the pulse, and β and μ are parameters related to the FWHM duration and frequency width;

$$t_{\text{FWHM}} \approx \frac{1.76}{\beta} \tag{7.2}$$

$$\nu_{\text{width}} = \frac{\mu\beta}{\pi} \tag{7.3}$$

An example of how the absolute Rabi frequency, and the instantaneous light frequency change as a function of time for a sechyp pulse can be seen in Figure 7.5. For a qubit initially in $|0\rangle$, such a sechyp pulse, resonant with the $|0\rangle \rightarrow |e\rangle$ transition, i.e., the blue arrow in Figure 7.1, causes the Bloch vector to evolve as seen in Figure 7.6. The result is a transfer to the $|e\rangle$ state.

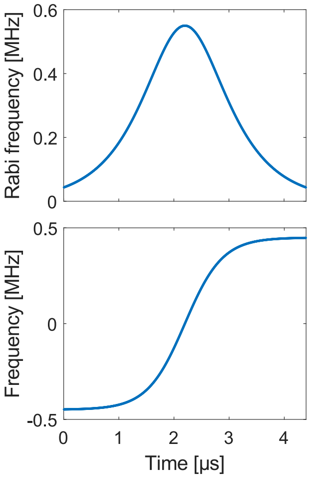

Figure 7.5. *The absolute value of the Rabi frequency, and the instantaneous light frequency of a sechyp pulse are shown in the upper and lower graphs, respectively.*

The benefits of using a sechyp pulse is its stability toward Rabi frequency fluctuations, as well as the fact that it works well for slightly detuned ions while still not exciting ions far from the resonance [91]. This is important because our qubit is an ensemble of ions with frequencies within a ~170 kHz region.

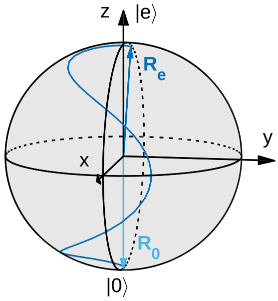

Figure 7.6. *The Bloch vector evolution for the sechyp pulse shown in Figure 7.5. The initial state is $R_0 = (0, 0, -1)$, i.e., $|0\rangle$, and the final state, R_e, is close to $|e\rangle$.*

In Pr^{3+}:Y_2SiO_5, the maximum transfer efficiency reached for two such sechyp pulses, first exciting and then deexciting, is 96% [60], which is close to being lifetime limited, i.e., the decay from the excited state during the duration of the pulses, 8 µs in total, is consistent with the efficiency loss in the experiments. For higher efficiency transfers, one option is to use much shorter pulses, but they require stronger fields and off-resonantly excite ions, which destroy the qubit either by introducing unwanted absorption in the pit or exciting the qubit on another transition.

An alternative for obtaining higher fidelities is to examine materials with longer lifetimes and/or larger hyperfine splittings. Eu^{3+}:Y_2SiO_5 fulfills both of these conditions (see Sections 4.4 and 4.1.2) and fidelities of 99.96% may be possible, see Paper **VII**.

Currently, our group have measured the relative oscillator strengths in $^{151}Eu^{3+}$:Y_2SiO_5 site 2, see Table 7.1, but due to a lack of available Rabi frequency, only one transition could be driven with a potentially high transfer efficiency. In order to estimate this efficiency, the qubit was cycled back and forth between $|1/2g\rangle$ and $|3/2g\rangle$ via $|5/2e\rangle$, where only the $|1/2g\rangle \rightarrow |5/2e\rangle$ transition was

Levels	±1/2e	±3/2e	±5/2e
±1/2g	0.01	0.11	0.88
±3/2g	0.18	0.73	0.09
±5/2g	0.81	0.16	0.03

Table 7.1: Relative oscillator strengths for $^{151}\mathrm{Eu}^{3+}$:$\mathrm{Y_2SiO_5}$ site 2. The uncertainties are estimated to ±0.03, and can be compared to the values measured for $^{153}\mathrm{Eu}^{3+}$:$\mathrm{Y_2SiO_5}$ site 1 in reference [92]

driven with the good pulse. Unfortunately, the uncertainties in the measurements, e.g., spontaneous decay from $|5/2e\rangle$, the read-out pulse affecting the population, and that two different pulses were used to transfer from $|1/2g\rangle$ and $|3/2g\rangle$, respectively, made the analysis inconclusive about the efficiencies of the two different pulses [93]. Thus, more effort is needed in order to reach the expected results.

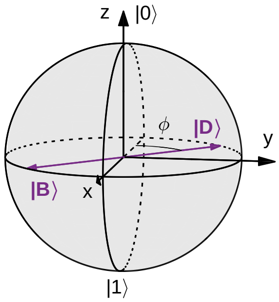

Figure 7.7. *Shows the Bloch sphere for the ground hyperfine levels* $|0\rangle$*, top, and* $|1\rangle$*, bottom, as well as the bright,* $|B\rangle$*, and dark,* $|D\rangle$*, states, which lie at opposite ends of the equator and are set by the angle* ϕ*.*

7.2.2 Two-color sechyp pulses

A one-color sechyp pulse is good for pole to pole transfers on the Bloch sphere but is not designed to do arbitrary single qubit gates, such as creating a superposition or performing a NOT operation. Fortunately, two-color pulses with center frequencies ω_0 and ω_1, as seen in Figure 7.1, where both components change as a sechyp, as shown in Figure 7.5, and have the same Rabi frequency, $\Omega_0 = \Omega_1$, but different phases ϕ_0 and ϕ_1, are able to perform any arbitrary single qubit gate in a robust manner [91]. Note that this section assumes two-color pulses that change as a sechyp, but the entire method is valid even when using simple two-color square pulses.

The two frequency components of the light interfere and, depending on their phase relation, $\phi = \phi_1 - \phi_0$, two ground state superpositions, bright, $|B\rangle$, and dark, $|D\rangle$, are useful to consider.

$$\begin{aligned} |B\rangle &= \frac{1}{\sqrt{2}}\left(|0\rangle + e^{-i\phi}|1\rangle\right) \\ |D\rangle &= \frac{1}{\sqrt{2}}\left(|0\rangle - e^{-i\phi}|1\rangle\right) \end{aligned} \tag{7.4}$$

The bright state interacts with the light, whereas the dark state does not due to destructive interference of the two excitation paths the ion can take, i.e., from $|0\rangle$ or $|1\rangle$ to $|e\rangle$. Using a Bloch sphere where $|0\rangle$ and $|1\rangle$ are on the top and bottom, respectively, the two states, $|B\rangle$ and $|D\rangle$, lie at opposite ends of the equator and make up an alternative basis, see Figure 7.7.

A two-color sechyp pulse, abbreviated to TC pulse, transfers any population in $|B\rangle$ to the excited state $|e\rangle$. By sending in another TC pulse, but with an overall phase shift of $\pi - \theta$, i.e.,

$\phi_0^{\mathrm{new}} = \phi_0 + \pi - \theta$ and $\phi_1^{\mathrm{new}} = \phi_1 + \pi - \theta$, the population returns to $|B\rangle$ once more, but with an added phase $e^{i\theta}$.

In summary, two TC pulses sent in after one another perform the following operation:

$$\begin{aligned} |\Psi_{\mathrm{init}}\rangle &= \alpha|B\rangle + \beta|D\rangle \\ \text{First TC pulse} &\rightarrow \alpha|e\rangle + \beta|D\rangle \\ \text{Second TC pulse} &\rightarrow e^{i\theta}\alpha|B\rangle + \beta|D\rangle \end{aligned} \tag{7.5}$$

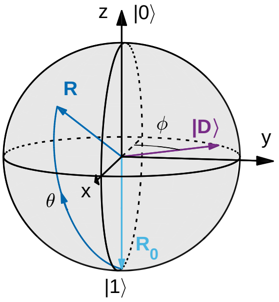

Figure 7.8. *The pair of TC pulses described in the main text and Equation (7.5), rotates the initial Bloch vector $\mathbf{R}_0$ an angle θ around the Dark state, $|D\rangle$, which is determined by the angle ϕ.*

This is equivalent to a rotation with an angle θ around $|D\rangle$ if one neglects any global phase factor, see Figure 7.8. Since any unitary operation on a single qubit can be written as a set of rotations [94, p. 174-177], these TC pulses can be used to perform any arbitrary single qubit gate.

In practice, two additional TC (compensation) pulses are needed after the pair described above, where $\phi^{\mathrm{comp}} = \phi + \pi$ and $\theta^{\mathrm{comp}} = 0$. These two pulses excite the former $|D\rangle$ state (since ϕ^{comp} is opposite the original ϕ on the Bloch sphere) and brings it back without any overall phase shift (since $\theta^{\mathrm{comp}} = 0$). They are needed to compensate for the phase spread obtained when the qubit peak is in the excited state, which occurs due to the slight difference in transition frequency of the various ions in the ~170 kHz wide absorption peak. For example, an ion with slightly higher frequency evolves its phase faster than an ion resonant with the laser and therefore gains an additional phase when excited. If only the first two TC pulses are used, simply the $|B\rangle$ part of the ion is excited and gains the extra phase spread. By using these compensation pulses, the former $|D\rangle$ part is also excited and therefore gains the same phase spread, which ensures that all ions, independent of resonant frequency, gain the desired phase shift of θ for the $|B\rangle$ state when all four pulses are considered.

7.2.3 Fast all-optical nuclear spin echo technique based on EIT (Paper V)

This section contains an overview of Paper **V** in which the bright-dark state description and TC pulses, otherwise known as electromagnetically induced transparency (EIT) pulses, are used in order to perform an all-optical Raman spin echo sequence on the hyperfine ground states $|0\rangle$ and $|1\rangle$ using the two transitions shown in Figure 7.1.

Assuming no state preparation, the relevant absorbing ions are in a completely mixed state, which can be written using the density matrix formalism, see Section 3.2;

$$\rho_{\mathrm{mixed}} = \frac{1}{2}\left(\rho_0 + \rho_1\right) = \frac{1}{2}\left(\rho_B + \rho_D\right) \tag{7.6}$$

where $\rho_x = |x\rangle\langle x|$.

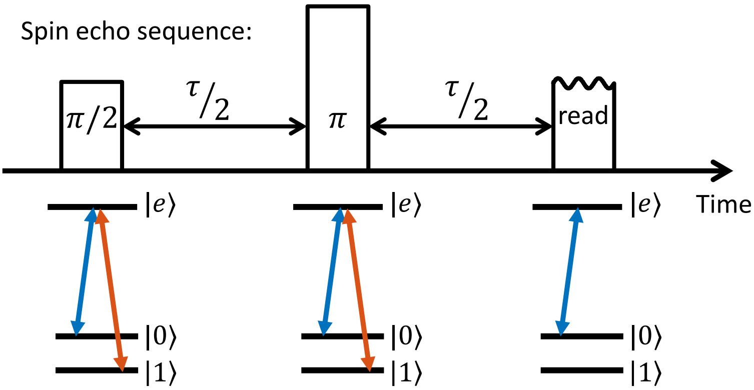

Figure 7.9. *An all-optical Raman spin echo sequence on the hyperfine ground states; see main text for more details.*

A single TC square pulse brings $|B\rangle$ to $|e\rangle$, i.e., $\rho_B \rightarrow \rho_e$. The remaining part of the state is ρ_D, which is a superposition of the hyperfine ground states since $|D\rangle = \frac{1}{\sqrt{2}}\left(|0\rangle - e^{-i\phi}|1\rangle\right)$. In other words, starting from a completely mixed state, a few microseconds long TC pulse creates a superposition between the hyperfine ground states.

Many similar techniques rely on optical pumping and therefore take much longer, many lifetimes of the excited state ($T_1 \approx 164$ µs for Pr^{3+}:$\mathrm{Y_2SiO_5}$ [48]), in order to create a superposition. However, the downside of the TC pulse method is that only half of the state is in a superposition, whereas the other half is in the excited state, but fortunately for some experiments this is not a crucial disadvantage.

For example, the TC pulse can be used as the first step in a spin echo sequence, which is generally called a $\pi/2$ pulse, as seen in Figure 7.9. In our case the TC pulse is a π pulse on the transition $|B\rangle \rightarrow |e\rangle$, but we will nevertheless call it a $\pi/2$ pulse and think about it in the $|0\rangle$-$|1\rangle$ basis, as seen in Figure 7.10(a), where, once more, half of the wave function is in $|e\rangle$ after the pulse is completed.

A general spin echo sequence is used to measure the coherence time of an inhomogeneous system, which in our case is the ground hyperfine inhomogeneity of $30 - 80$ kHz [58]. The first pulse, $\pi/2$ pulse, generates a superposition. After a waiting time of $\tau/2$, during which the ions quickly dephase, ϕ^{dephase}, due to differences in their hyperfine splittings, a π pulse is used to inverse the phase obtained so far, $\phi^{\text{inverse}} = \pi - \phi^{\text{dephase}}$. After another waiting time of $\tau/2$, the ions rephase and emit a strong signal, see Section 3.3.1, but now on the opposite side of the Bloch sphere; $\phi^{\text{rephase}} = \phi^{\text{inverse}} + \phi^{\text{dephase}} = \pi$, regardless of their hyperfine inho-

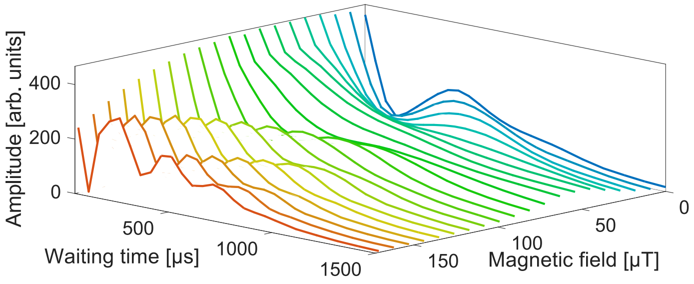

Figure 7.11. *The readout strength of the spin echo sequence seen in Figure 7.9 as a function of waiting time τ and external magnetic field strength. The decay with time is due to the limited coherence of the hyperfine ground states. The coherence time curve is at a maximum for an external field of about 50 μT, which is of similar strength as the Earth's local (Lund University, Sweden) magnetic field [95].*

mogeneity. The coherence time of the system is measured by varying the waiting time τ and analyzing the readout strength, which decreases for longer waiting times due to increased decoherence of the system because of more interactions with the environment.

For our sequence, seen in Figure 7.9, the π pulse is another TC pulse, but with twice the Rabi frequency and a different phase on the $|1\rangle \rightarrow |e\rangle$ transition, $\phi_1^{\text{new}} = \phi_1 + \pi/2$, performing the rotation seen in Figure 7.10(b). The rephasing of the hyperfine ground states is detected by continuously exciting only the $|0\rangle \rightarrow |e\rangle$ transition, see the last pulse in Figure 7.9, which generates a beating signal at 10.2 MHz between the incoming laser light and the rephased coherence between $|1\rangle$ and the part excited from $|0\rangle$ to $|e\rangle$.

In Paper **V**, simulations of this spin echo sequence were made using the optical Bloch equations, as seen in Figure 7.10(a)-(b). A qubit was also prepared experimentally, as described in Section 7.1, and the pulse sequence was tested and analyzed using quantum state tomography, the results of which can be seen in Figure 7.10(c).

Furthermore, the technique was used to optimize an external magnetic field in order to achieve a longer hyperfine coherence time. This experiment was performed without any qubit initialization, i.e., on an initially completely mixed state. A coherence was created within microseconds using the fast $\pi/2$ pulse, which can be compared with other methods that normally require preparation through optical pumping, thereby taking several optical lifetimes, i.e., milliseconds. A full coherence time measurement curve consisting of 30 spin echo measurements with different waiting times τ was performed and analyzed with an update frequency of 1 Hz,

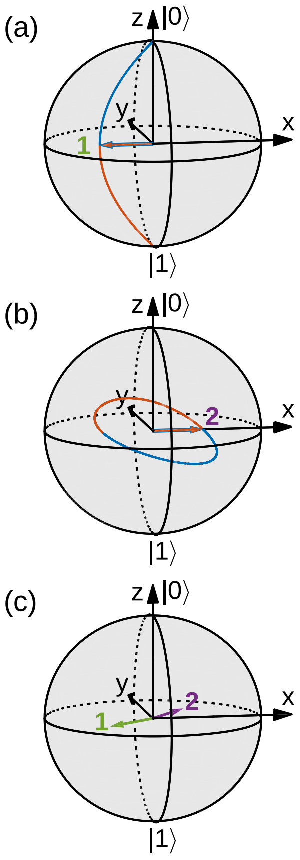

Figure 7.10. *Bloch simulation results of the $\pi/2$ and π TC pulses, i.e., the first two steps of the spin echo sequence in Figure 7.9, are shown in (a) and (b), respectively. Instead of starting in a fully mixed state, the simulations show the two paths ions take if they start in $|0\rangle$, blue lines, or $|1\rangle$, red lines. Note that in both (a)-(b) the blue and red arrows, which indicate the Bloch vector after the pulse(s), overlap. (c) For a qubit initially in $|0\rangle$, experimental quantum state tomographies were performed after the $\pi/2$ pulse, shown in green, denoted by 1, and should match the results in (a), and after both a $\pi/2$ and π pulse, shown in purple, denoted by 2, and should match (b).*

making it possible to optimize the magnetic field strength in real time. The results of this optimization, along the most sensitive magnetic field direction, can be seen in Figure 7.11, where a compensation field of ∼50 µT, corresponding to the local (Lund University, Sweden) vertical component of the Earth's magnetic field [95], yielded the best result.

The ground state hyperfine coherence time was measured as a function of temperature that reached all the way up to 11 K before the readout signal became too weak to yield a reliable measurement value, see Figure 7.12. The difficulties inherent to such experiments lie in the rapid decrease of the optical coherence time with increasing temperature, $T_2^{\text{optical}} \propto 1/T^7$ [41–43], which has limited previous measurements up to 6 K [96]. Thus, these new experiments work for optical linewidths $(11/6)^7 = 70$ times broader than previous ones.

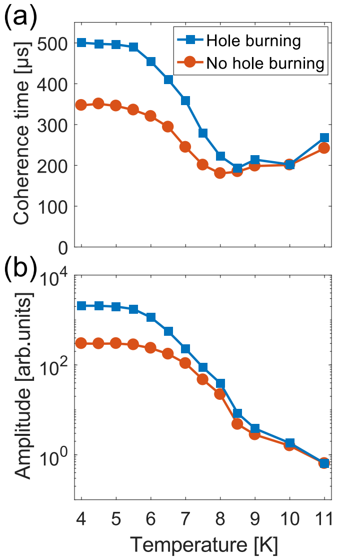

Figure 7.12. *(a) Hyperfine ground state coherence time and (b) readout signal strength of the spin echo sequence, both as a function of temperature. The red data uses only the spin echo sequence, as in Figure 7.9, whereas the blue data also initially burns a 2 MHz wide hole centered around the $|0\rangle \rightarrow |e\rangle$ transition. At around 8 K, this hole burning procedure stops working due to the increased optical linewidth, and the two curves overlap.*

The results presented in Figure 7.12 are based only on the spin echo sequence for the red lines, but use an additional preparatory hole burning procedure that empties a 2 MHz wide region around the $|0\rangle \rightarrow |e\rangle$ transition for the blue lines. Hole burning yielded better results, due presumably to the decrease in instantaneous spectral diffusion that affects the nuclear spin states. At around 8 K, it is no longer possible to burn a spectral hole and the two curves overlap. This might indicate that the decrease in coherence time around $6-8$ K is due wholly to increased optical excitation and not a real decrease in the hyperfine coherence time. See Paper **V** for a more in-depth discussion of these results.

In conclusion, a fast spin echo sequence was implemented and used to adjust a magnetic field in real time, as well as measuring the hyperfine coherence time up to a temperature of 11 K.

7.3 Qubit-qubit interaction (Paper VI)

The next step after performing arbitrary single qubit operations involves two-qubit gates. The idea investigated in this section and Paper **VI** is based on the dipole blockade effect, i.e., the use of the DC Stark effect and the state dependent static dipole moment, explained in Section 3.4 and 4.3, respectively, to control the target qubit based on the state of the control qubit, as illustrated in Figure 7.13.

Unfortunately, the dipole blockade effect works only for target ions situated close to a control ion, since the frequency shift scales with $1/r^3$, where r is the distance between the ions [97], and the magnitude of the shift needs to be large enough to move the ion out of resonance with the laser. Thus, the preparation scheme of our two qubits is more complex than described in Section 7.1.

In the first step of emptying frequency regions of absorption, as shown in Figure 7.2, you have to burn the two pits interleaved

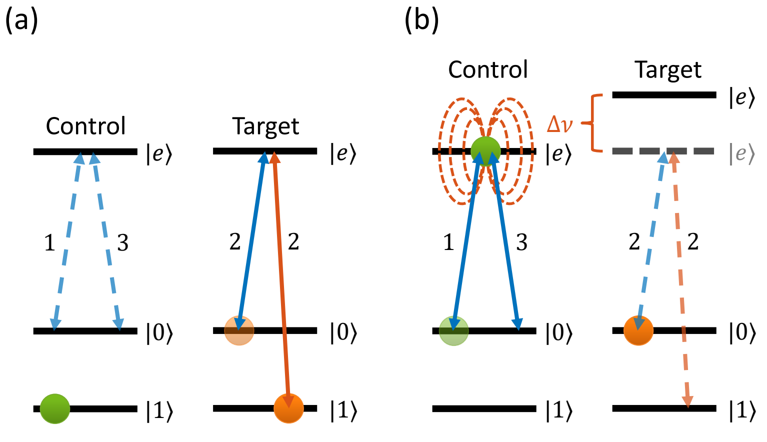

Figure 7.13. *The pulse sequence for a two-qubit interaction, controlled NOT (CNOT) gate, between a control and target qubit is shown with a simplified energy level structure. The target is initially in state* $|0\rangle$. *(a) The control is in* $|1\rangle$. *The first transfer pulse, denoted by* 1, *is ineffective and the control remains in the ground state. The desired single qubit operation, denoted by* 2 *and shown here as a NOT gate, is performed on the target qubit. The third pulse,* 3, *is also ineffective, since the control is not in* $|e\rangle$. *(b) Control is initially in* $|0\rangle$. *Pulse* 1 *excites the control whose new static dipole moment, illustrated by the dashed red lines around the control qubit, shifts the resonance frequency of the target by an amount* $\Delta\nu$. *The two-color pulse, pulse* 2, *is no longer resonant and does nothing. Finally, the control will be brought back to* $|0\rangle$ *by pulse* 3.

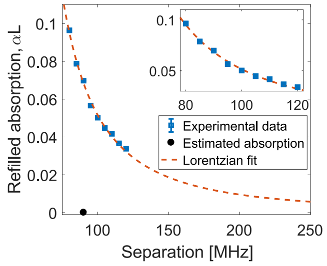

Figure 7.14. *When sequentially emptying two frequency regions of absorbing ions, the first region is partially refilled due to off-resonant excitation during the optical pumping of the second region. This refilled absorption is shown in the blue squares as a function of the frequency separation of the two regions. The error bars, which lie inside the squares, show the standard error of the mean. A Lorentzian fit is shown in the red line, and an estimation of the refilled absorption when using an interleaved burning scheme is shown in the black circle.*

and not one after the other, since off-resonant excitation otherwise reintroduces absorption in the first region during the optical pumping of the second one. The magnitude of this refilled absorption in the first region was studied as a function of the frequency separation between the pits, as seen in Figure 7.14. A Lorentzian fit agrees well with the experimental results. Thus, off-resonant excitation appears to be the reason for the refilling. As mentioned earlier, this effect can be minimized by alternating the burning between the two regions, which results in a very low refilled absorption. This is estimated for the 90 MHz separation used in all the following experiments, by assuming that all 700 burn pulses used to create one empty region contributes equally to the refilled absorption shown in Figure 7.14, and that only the last burn pulse contributes when the interleaved burning scheme is used. This results in a refilled absorption of $0.07/700\ \alpha\mathrm{L} = 10^{-4}\ \alpha\mathrm{L}$, as shown by the black circle in Figure 7.14.

After the absorption peaks have been created for both qubits, initializing them to state $|0\rangle$, the scheme shown in Figure 7.15 is

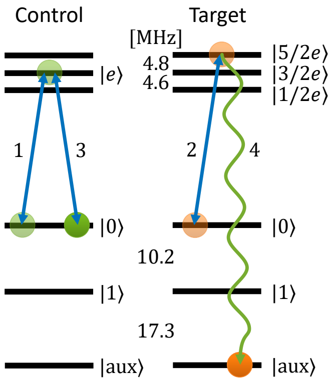

Figure 7.15. *The main part of the preparation scheme to remove unwanted target ions is shown. 1) The control is excited. 2) Unwanted target ions are excited to $|5/2e\rangle$, whereas wanted target ions are not excited due to the dipole blockade effect shown in Figure 7.13(b). 3) The control is deexcited back to $|0\rangle$. 4) The unwanted target ions spontaneously decay, for example to $|\mathrm{aux}\rangle$ where they are removed from the target qubit. See Paper* ***VI*** *for more detailed information about the full preparation scheme.*

used to remove unwanted target ions, i.e., those not located close enough to a control ion for the dipole blockade effect to work. The main part of the scheme consists of four steps:

1. The control is excited on the $|0\rangle \rightarrow |e\rangle$ transition
2. Unwanted target ions located far from any control ion are excited to $|5/2e\rangle$, whereas target ions situated sufficiently close to a control ion are left in $|0\rangle$ due to the dipole blockade effect
3. The control is deexcited from $|e\rangle$ to $|0\rangle$
4. Waiting: the unwanted target ions spontaneously decay, preferably to $|\mathrm{aux}\rangle$

Using this scheme, each target ion located close enough to a control ion has a resonance frequency shift after step 1, is never excited by step 2, and remains part of the target qubit placed in $|0\rangle$. However, undesired target ions are excited in step 2 and thereby can decay to $|\mathrm{aux}\rangle$ where they are no longer part of the qubit. Since this approach is probabilistic, it needs to be repeated several times in order to remove as much as possible of the unwanted background ions. The scheme is presented with more details in Paper **VI**, which includes repumping of ions from state $|1\rangle$ for both the target and control qubit, and finally repeating the whole procedure once more after the control and target roles of the qubits have been switched.

In order to estimate the absorption that originates from target ions close enough to a control ion (referred to as the signal), the target absorption is measured in two cases. First, after performing steps 1-4 once. Second, after only performing steps 2 and 4, where step 2 excites all target ions with equal probability since the control ions were never excited. Thus, after performing the scheme once, the remaining absorption in the target peak is lower in the latter case compared to the former case where target ions situated close enough to a control ion are not removed. The difference in absorption of these two measurements correspond to the absorption from target ions situated close enough to a control ion. More information about the data treatment can be found in Paper **VI**.

This difference in absorption, i.e., the signal, was studied as a function of the control qubit ion density, as seen in Figure 7.16. In these experiments, the control qubit peak was approximately 1 MHz wide (FWHM), whereas the target peak was about 140 kHz in order to increase the likelihood that a target ion was close enough to a control ion in order to be shifted out of resonance with the laser pulses that have a frequency width similar to the peak width. The signal scales linearly with the control qubit ion density, as indicated by the linear fit shown in the red line. The signal also scales linearly with the target qubit ion density. Thus, the signal, i.e., the number of target ions situated close enough to a control ion, scales quadratically with the total ion density per frequency channel. For a given material, the absorption coefficient, α, is therefore a good parameter to maximize by, e.g., being in the center of the inhomogeneous profile or minimizing crystal defects that can otherwise cause a broadening of the inhomogeneous linewidth and thereby a reduction in the maximum absorption coefficient.

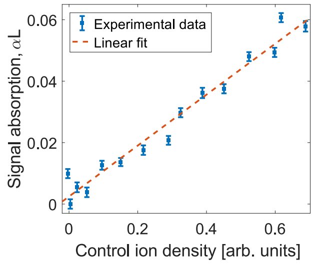

Figure 7.16. *The target signal absorption as a function of the control ion density is shown in the blue squares, where the error bars display the error of the mean. A linear fit is shown in the red line.*

In Figure 7.17, the signal and background absorptions are seen as a function of the number of repetitions of the preparation scheme. The background decreases exponentially at a faster rate than the signal, such that the signal-to-background ratio can be increased. However, the uncertainty, or noise, in the evaluation of a zero signal, as shown in the black line, indicates that the preparation scheme cannot be repeated many more times before the signal-to-noise ratio decreases below 1. For these experiments, both the control and the target qubits were 1 MHz wide, since the transfer pulses can be made shorter in time when using wider peaks, which reduce the duration spent in the excited state for the control ions and thus reduce lifetime decay as well.

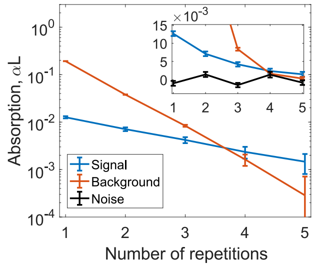

Figure 7.17. *The signal, i.e., the absorption originating from target ions situated sufficiently close to a control ion, and background, i.e., the absorption from unwanted target ions, can be seen in the blue and red lines, respectively, as a function of the number of repetitions of the preparation scheme presented in Figure 7.15. The black line shows the uncertainty, or noise, in the evaluation of a zero signal.*

The interleaved burning scheme, the quadratic scaling of the number of target ions located close enough to a control ion as a function of the ion density per frequency channel, and the demonstration that the signal-to-background ratio can be increased by repeating the preparation scheme, are the current results in Paper **VI**, but some final experiments with a CNOT are planned before the manuscript can be finalized and submitted for peer review and publication.

Unfortunately, the ensemble qubit approach is not scalable in the long run, as the number of ions in each qubit decreases exponentially as more qubits are added. Calling the probability of one ion being close enough to an ion in another qubit p, the probability of finding n qubits that interact in a chain, i.e., qubit 1 interacts with qubit 2, which in turn interacts with qubit 3 etc., is p^{n-1}. Fortunately, if single ions are used instead as individual qubits you can find long chains of interacting qubits. The problem then lies in reading out the state of single ions, a topic discussed in the next section.

7.4 Single ion readout scheme (Paper VII)

To circumvent the poor scaling of ensemble qubits, this section and Paper **VII** investigate a single ion scheme where a dedicated readout ion of a different element than the qubit ion is used to perform state selective detection of single ion qubits. Whereas the qubit element can be heavily doped into the crystal to make it easier to find qubit chains, as seen in Figure 7.18, the readout ion should be sparsely doped such that single ion detection is possible. The

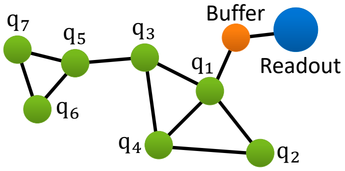

Figure 7.18. *A qubit chain consisting of seven qubits, one buffer (also of the qubit kind), and one readout. The black lines indicate possible two-qubit interactions. The procedure for reading out qubit 1 is shown in Figure 7.19. Any other qubit is read out in the same way after the quantum state of the desired qubit has been switched with qubit 1.*

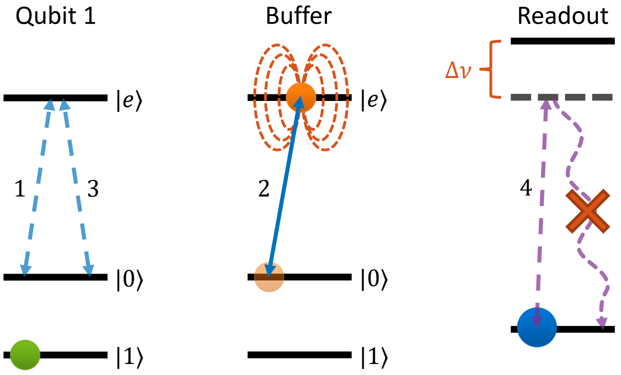

Figure 7.19. *The procedure for reading out the quantum state of qubit 1, seen in Figure 7.18, using one buffer ion. Two possible scenarios exist: qubit 1 is in $|0\rangle$ or $|1\rangle$; this figure explains the latter. Pulse 1 targets the $|0\rangle \rightarrow |e\rangle$ transition of the qubit and does nothing since the ion is in $|1\rangle$. The buffer is then excited by pulse 2, which shifts the resonance frequency of the readout ion. Pulse 3 does nothing on the qubit since it was never excited, and pulse 4 is no longer in resonance with the readout ion and thus no fluorescence is emitted. In the other scenario, the qubit is in $|0\rangle$, 1 excites it, the buffer becomes detuned, pulse 2 is ineffective, and the qubit is deexcited by pulse 3. In this case, the readout ion is in resonance with pulse 4 and a strong fluorescence signal is detected. The state of qubit 1 is thus detected based on a low/high fluorescence signal from the readout ion. This procedure can be repeated multiple times in order to increase the collected photon statistics as long as the buffer is reinitialized to $|0\rangle$.*

scheme also allows for the use of buffer ions, also of the qubit ion element, to increase the readout fidelity at the price of shrinking the qubit chain by one for each buffer ion used.

The readout scheme is presented in Figure 7.19, and is based on the dipole blockade effect explained in Section 7.3 and Figure 7.13, to connect the readout ion fluorescence, via a buffer ion, to the qubit state.

Our group is currently investigating two possible candidates for the readout ion. First, neodymium (Nd) placed in a high-finesse micro-cavity. Its excited state lifetime can be shortened due to the Purcell effect in the cavity, and is estimated in Paper **VII** to become around 200 ns, which is necessary in order to produce enough fluorescence during the limited lifetime of the qubit and buffer ions. Due to the high collection efficiency of the cavity, a total detection efficiency of about 10% is reasonable. This approach is still in its infancy, but additional experiments are planned.

Second, the 4f-5d transition in cerium (Ce) is inherently short lived with a lifetime of 40 ns, and its fluorescence can be detected using a confocal microscope setup. Such a setup has been constructed by our group [87] and is used in Section 7.5 and Paper **VIII** in an attempt to detect single Ce ions. So far, however, no discrete single ion signal has been observed, but the investigation is ongoing.

Simulated photon statistics of this readout scheme can be seen in Figure 7.20, where the results are valid for any type of readout ion as long as the ratio of the lifetime and collection efficiency remains constant. The data assume a Eu^{3+}:Y_2SiO_5 crystal, and photons are collected during an optimum time period based on the number of collected photons per time interval and the Eu excited state lifetime.

Paper **VII** also contains a thorough calculation of an estimated CNOT fidelity without or with readout when using Eu as a qubit ion, resulting in fidelities of 99.4% and 99.1%, respectively. Furthermore, the scalability of the system is analyzed by calculating the estimated fidelity of creating n-qubit Greenberger-Horne-Zeilinger (GHZ) states, the results of which can be seen in Figure 7.21. An important assumption during these calculations was that all qubits could directly interact with the buffer ion, which is reasonable for a system of up to at least five qubits if a 4% qubit doping concentration is used. If the qubits cannot directly interact with the buffer ion, their quantum information can be switched to a qubit that can, at a cost of reducing the readout fidelity. Alternatively, several readout ions with associated buffer ions can be used to create islands of qubits that can be read out directly. This, however, introduces the problem of differentiating between the different readout ions during detection.

Summary of Paper **VII**: a single ion qubit scheme using a dedicated readout ion and buffer ion(s) is presented together with fidelity calculations of the readout, a CNOT, and the system scalability.

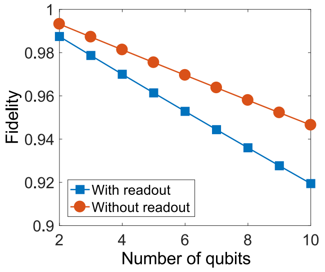

Figure 7.21. *Estimated fidelities of n-qubit GHZ states with or without readout. In the readout case, the results assume that all qubit ions can directly interact with the buffer ion, which is reasonable for up to at least five qubits using a qubit doping concentration of 4%.*

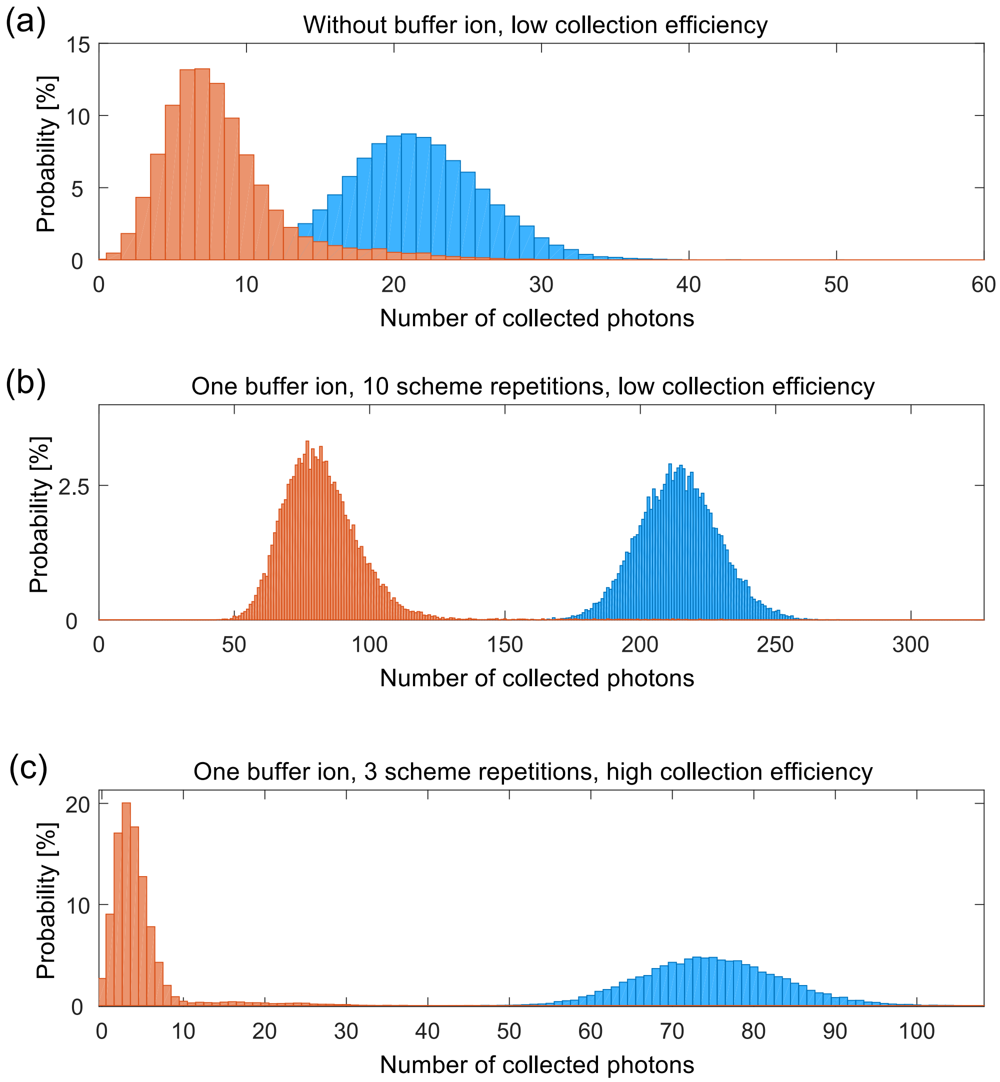

Figure 7.20. *Simulation over the number of detected fluorescence photons for the two qubit states: $|0\rangle$, in blue, and $|1\rangle$, in red. Valid for either Nd in a micro-cavity with a 200 ns lifetime and (a)-(b) 1%, (c) 10% collection efficiency, or Ce in a confocal microscope setup with 40 ns lifetime and collection efficiencies of (a)-(b) 0.2%, (c) 2%: (a) without the use of a buffer ion and low collection efficiency; (b) one buffer ion with 10 repetitions of the scheme shown in Figure 7.19, still using low collection efficiency; (c) one buffer ion and only 3 repetitions, but a high collection efficiency. The probability of distinguishing between the two states is (a) 93%, (b) 99.7%, and (c) 99.85%.*

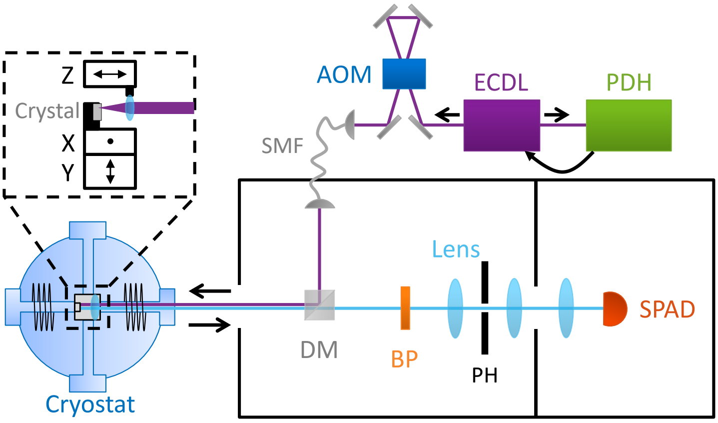

Figure 7.22. *Simplified laser and confocal microscope setup. An external cavity diode laser (ECDL) is locked to a cavity with the Pound-Drever-Hall (PDH) technique. The laser light, shown as purple lines, goes through a double pass acousto-optic modulator (AOM) before propagating through a single mode fiber (SMF) to the microscope setup. A dichroic mirror (DM) reflects the laser light into the crystal holder (see figure at upper left) situated in the cryostat. The crystal can be translated in the transverse directions, x and y, using atto-cubes, and the lens can be moved in the z direction. The fluorescence (turquoise lines) is collected and then transmitted through the dichroic mirror (DM) and the band pass filters (BP), which suppress any reflected laser light. The single photon counting avalanche diode (SPAD) detects the fluorescence after it has passed through a pinhole (PH).*

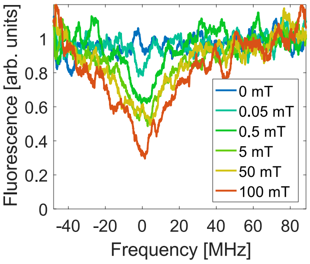

Figure 7.23. *The width of a spectral hole, created by redistributing ions in the Zeeman levels, is investigated as a function of an external magnetic field. The data is smoothed with a moving average corresponding to 4 MHz on the frequency axis. The data has been normalized such that the mean value above 50 MHz is set to one.*

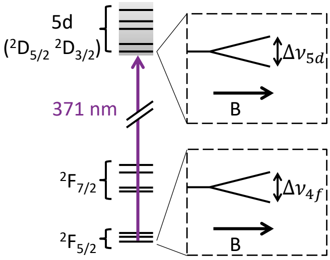

Figure 7.24. *Relevant energy levels of cerium. The insets shows the Zeeman splitting of the ground and excited zero-phonon line states as a function of the applied magnetic field.*

7.5 Cerium (Ce) as a dedicated readout ion (Paper VIII)

In an attempt to experimentally realize the single ion qubit scheme discussed in Section 7.4 and Paper **VII**, much effort has been devoted to detecting a single cerium ion in a Ce^{3+}:Y_2SiO_5 crystal. So far, our group has not been able to detect any discrete fluorescence signals that could indicate single instances. Nevertheless, this section provides an overview of the effort and results of Paper **VIII**, where spectral hole burning in the Zeeman levels and a permanent trapping mechanism in cerium are analyzed. The confocal microscope setup used for these experiments can be seen and is explained in Figure 7.22.

In Figure 7.23, the size of a spectral hole as a function of an external magnetic field is analyzed. The hole is burned in the Zeeman levels that are split due to the non-zero magnetic field, see Figure 7.24. As can be seen, the hole becomes wider and deeper for stronger magnetic fields, but the reason why is unknown. The narrowest hole was achieved for an applied field of 0.05 mT

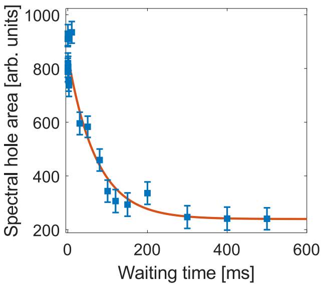

Figure 7.25. *The Zeeman spectral hole area as a function of the waiting time between the readout and the hole burning. The lifetime is estimated to be* 72 ± 21 *ms at an external magnetic field strength of* 10 *mT. Data points are shown in blue, where the error bars mark one standard deviation. The red curve is an exponential fit.*

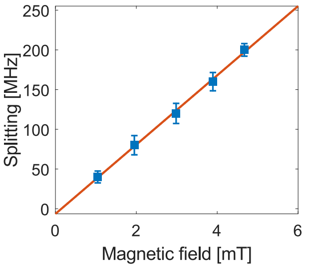

Figure 7.26. *The ground + excited state Zeeman splitting,* $\Delta\nu_{4f} + \Delta\nu_{5d}$*, as a function of the external magnetic field is shown in blue, where the error bars mark one standard deviation. A linear fit is displayed in red with a slope of* 43.4 ± 1.7 *MHz/mT.*

(6 ± 4 MHz wide), yielding an upper limit of 3 ± 2 MHz on the homogeneous linewidth of the 4f-5d zero-phonon line transition.

The lifetime of the spectral hole was also measured by graphing the hole area as a function of the wait time between the hole creation and readout, as seen in Figure 7.25 for an external magnetic field of 10 mT. An exponential fit yields a lifetime of 72 ± 21 ms.

The combined Zeeman splitting of the ground and excited states as a function of applied magnetic field was measured, as seen in Figure 7.26. The fitted red line represents a dependence $\frac{\Delta\nu_{\mathrm{4f}}+\Delta\nu_{\mathrm{5d}}}{\Delta B} = 43.4 \pm 1.7$ MHz/mT. Similar data yields an estimate for only the ground state splitting; $\frac{\Delta\nu_{\mathrm{4f}}}{\Delta B} = 17.9 \pm 1.5$ MHz/mT, which is in agreement with the known ground state splitting rate of 19 MHz/mT [98, 99]. Combining these results yielded an estimate for the excited state Zeeman splitting of $\frac{\Delta\nu_{\mathrm{5d}}}{\Delta B} = 25.5 \pm 2.3$ MHz/mT.

During these investigations, it was observed that the fluorescence signal decreased from its original high photon count rate, as seen in Figure 7.27. Throughout this measurement, the laser shone on the sample with constant intensity. It was also locked and stable within the homogeneous linewidth of the transition. Even after blocking the laser light for up to 40 minutes, the fluorescence signal never returned to its original high count rate. This permanent hole was measured to be around 70 MHz wide (FWHM), where a magnetic field of 0.2 mT was used to compensate for a stray magnetic field present inside the cryostat at the time of the experiment. This relatively narrow linewidth suggests that it goes via the 4f-5d zero phonon line, as no other transition is that narrow. However, the reason for the discrepancy of 70 MHz and the value of 3 ± 2 MHz measured above is still unknown.

A rate equation model with the 4f, 5d, and conduction band levels, as well as a trapping state connected to the conduction band, was used to simulate the decrease in the fluorescence signal. The result of this simulation can be seen in the red line of Figure 7.27, and more details about the simulations can be found in Paper **VIII**.

In conclusion, Paper **VIII** investigates spectral hole burning in the Zeeman levels, determines the hole lifetime, and sets an upper limit on the homogeneous linewidth of the 4f-5d zero phonon line transition. Furthermore, the Zeeman splitting coefficients for the ground and excited state are also estimated. Finally, a permanent trapping that reduces the cerium fluorescence signal was observed.

7.6 Investigating Eu^{3+}:Y$_2$O$_3$ nanocrystals

In addition to trying to detect single cerium ions, the confocal microscope setup presented in Section 7.5 has been used to study europium doped into yttrium oxide (Eu^{3+}:Y$_2$O$_3$) nanocrystals.

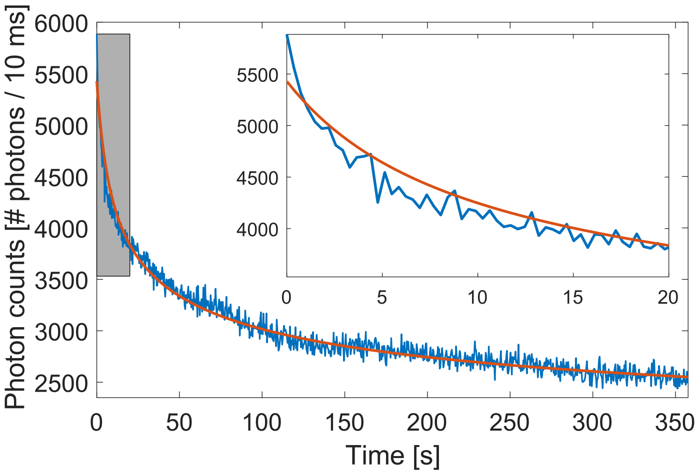

Figure 7.27. *A decrease in the fluorescence signal due to permanent trapping as a function of time under continuous laser illumination of the* Ce^{3+}*:*Y_2SiO_5 *crystal can be seen in the blue line. The strong fluorescence signal does not return, even after blocking the laser for up to* 40 *minutes, indicating that the trap lifetime is at least hours. The red line shows the results of a rate equation model, as further explained in Paper* ***VIII***.

However, since the first draft of this work is not ready yet, I will be very brief about the experimental method and results.

The confocal microscope setup, seen in Figure 7.22, was modified to the Eu^{3+}:Y_2O_3 wavelength of around 580 nm and used to probe approximately 400 nm large nanocrystals with the dye laser setup, instead of the UV external cavity diode laser used for the cerium experiments. For more information about the laser setups, see Appendix A. The setup allows for high spatial and spectral resolution data to be collected from a relatively small ensemble of ions distributed in only a few nanocrystals. Different sample/substrate combinations were analyzed in order to obtain a low background fluorescence and reflection.

A three-frequency measurement technique, where the incoming light quickly alternates between three frequencies, was used to determine the ground hyperfine level orderings for both europium isotopes. Furthermore, the homogeneous linewidth of the ions was measured. Since it was much broader than the natural linewidth, however, more investigations were performed, which revealed interesting properties of the spin dynamics of the ions within the nanocrystals.

7.7 Progress on DiVincenzo's criteria

This section summarizes the progress of rare-earth quantum computing with respect to the DiVincenzo criteria. The discussion is based on the single ion readout scheme presented in Section 7.4 and Paper **VII**, but several other equally likely approaches exist.

A scalable physical system with well-characterized qubits

At the current stage, well-characterized ensemble qubits have been experimentally realized. In order to have a more scalable system, however, single ion qubits are required. Our group's inability to achieve single ion detection so far has resulted in poor experimental progress. Nevertheless, the basic qubit preparation and initialization should be very similar for the two approaches.

The ability to initialize the state of the qubits to a simple fiducial state, such as $|000...\rangle$

Regardless of the ensemble or single ion qubit approach, the scheme for initializing qubits is well-established [49]. In Paper **VI**, two qubits were prepared at different optical frequencies, with only the minor problem of off-resonant excitation causing the spectral hole of the first qubit to be partially refilled during the preparation of the second qubit. This was solved by preparing the qubits simultaneously by alternating the hole burning between the two frequency regions instead of creating one before moving on to the next. At this stage, no major problems are expected when more qubits are initialized, but potential difficulties include spectral diffusion and off-resonant excitation, as mentioned above. It will also be more difficult to analyze the preparation of the nearby absorption structure in the single ion scheme, where only the qubit state is readily available, compared to the ensemble approach, where the vicinity of the qubit peak can be easily probed through an absorption measurement.

For error correcting quantum computation, the initialization of qubits used to measure the error should ideally be on the timescale of the gate operations. Currently, the initialization step takes several lifetimes of the excited states since it uses optical pumping. Short-lived Stark levels could potentially be used to rapidly initialize a qubit, but has so far not been demonstrated.

Long relevant decoherence times, much longer than the gate operation time

As seen in Tables 4.1 and 4.2, the coherence times are up to milliseconds long for the optical transition and can be several hours for the ground spin states in $Eu^{3+}:Y_2SiO_5$. The small hyperfine splittings of $Pr^{3+}:Y_2SiO_5$ set the minimum pulse duration to the microsecond scale, which results in single qubit gate fidelities of about 96% due to the limited optical coherence time [60]. Fortunately, for $Eu^{3+}:Y_2SiO_5$, estimated fidelities of 99.96% seem reasonable, see Paper **VII**, but have not yet been proven experimentally. Furthermore, the extremely good ground hyperfine coherence times mean that quantum information can be stored for a very long time.

A “universal” set of quantum gates

With the use of two-color sechyp pulses, arbitrary single qubit gates can be performed in a robust manner [89–91]. The two-qubit CNOT operation will hopefully be demonstrated experimentally soon with the initial steps being taken in Paper **VI**. Together with arbitrary single qubit gates, it forms a basis that is capable of performing any quantum gate. However, the fidelities need to be improved for any practical quantum computation application.

A qubit-specific measurement capability

Due to the lack of single ion detection, this requirement is the critical point at which more effort is needed in order to proceed with the scalable single ion qubit scheme.

7.8 Outlook of projects

In this last section, the future of the quantum computation projects is discussed.

The electromagnetically induced transparency (EIT) project, Paper **V**, measured the ground hyperfine coherence time for temperatures up to 11 K. No experiments are currently planned for reaching higher temperatures. But the effort devoted to creating a real-time display of entire measurement curves has proven extremely useful and speeds up present-day experiments.

With regard to the two-qubit interaction project presented in Paper **VI**, additional experiments are planned in order to demonstrate a CNOT gate. It seems likely that some parts of the CNOT gate will soon be demonstrated, e.g., showing $|00\rangle \rightarrow |00\rangle$ and $|10\rangle \rightarrow |11\rangle$. The additional error introduced by placing the control in a superposition, and, after the CNOT gate, performing a full quantum state tomography, might unfortunately be too large to demonstrate a full entanglement between the two qubits. After these experiments have taken place the manuscript will be updated and submitted for peer review and publication.

The two single ion readout schemes discussed in Section 7.4 and Paper **VII**, the Nd micro-cavity and the Ce confocal microscope, are still under investigation, but no experimental realization of the scheme has yet been achieved.

The Nd^{3+}:Y_2O_3 coherence time was recently measured in a ceramic sample, and the initial unpublished results are promising. The next step is to set up the micro-cavity and look at Nd^{3+}:Y_2O_3 nanocrystals inside the cavity.

The Ce approach has had its setbacks over the years. Although no single ion has yet been detected, the results are progressing with further investigation into both the permanent trapping, Paper **VIII**, and the problems we face in detecting single ions. Our current effort is devoted to using micro-crystals instead of bulk in the confocal microscope setup in order to reduce the fluorescence signal obtained from ions far away from the focus along the laser beam propagation direction. Even though single ion detection of rare-earth-ions have been achieved, e.g., in references [100–106], no one has so far performed state selective readout of a qubit ion based on the fluorescence from a single dedicated readout ion.

An article about the Eu^{3+}:Y_2O_3 nanocrystals is currently under preparation, and no further experiments are planned at this time.

CHAPTER 8

CONCLUSIONS

How light propagates and is absorbed in rare-earth-ion-doped crystals, a few applications of slow light, and some steps toward quantum computing; that is the briefest summary I can make of my thesis work.

With respect to the light-matter interaction results, we have drawn attention to how the polarization of light changes while propagating through birefringent crystals with off-axis absorption or gain, even if the incoming light is polarized along a principal axis (Paper **I**). Furthermore, a narrowband spectral filter has been created with a suppression of 53.4 ± 0.7 dB between light pulses separated in frequency by only 1.25 MHz (Paper **II**).

The slow light and DC Stark effects have been used to frequency shift light within ±4 MHz with efficiencies above 85% (Paper **III**), tune the group velocity of a pulse from 1.5 km/s to 30 km/s, i.e., a tunable range of a factor of 20, with efficiencies above 80%, and temporally compress an incoming pulse by a factor of approximately 2 (Paper **IV**).

From an initially mixed state, we showed that a partial superposition can be achieved in microseconds between two ground nuclear states using an optical two-color pulse (Paper **V**). In this state, half of the wave function is in the excited state, whereas the other is in a superposition of two ground states. This can be compared to optical pumping methods, which, although they can generate a full superposition state, take many times the excited state lifetime to complete, i.e., up to several milliseconds. The optical two-color method was used to measure the ground state hyperfine coherence time as a function of temperature, reaching up to 11 K.

With regard to quantum computing, two ensemble qubits have been initialized simultaneously and qubit-qubit interactions have been shown in preparation of performing a CNOT gate (Paper **VI**). However, due to poor scaling of the ensemble qubit approach, another scheme using single ion qubits has also been investigated. In order to perform state selective readout of these single ions, we suggested to use a dedicated readout ion and buffer ions to reach high fidelity readouts (Paper **VII**). One potential candidate for the dedicated readout ion is cerium, and although we have not detected a single cerium ion yet, an upper bound on the homogeneous linewidth, 3 ± 2 MHz, was obtained and a slow, minute timescale, permanent spectral hole burning mechanism was observed (Paper **VIII**).

8.1 A personal perspective

During my time here, I have learned a great deal, especially with respect to light-matter interaction, which actually was the name of the course in which I came into contact with Stefan Kröll, my supervisor. The group's ideas about ultrasound optical tomography (UOT) have recently evolved into today's full-fledged project with monthly meetings and collaboration between several scientifically diverse research teams. My hope is that the effort devoted to the spectral filters and frequency shifters will benefit the future of this project, just as my knowledge of light-matter interactions has helped during various discussions.

As is often the case in science, a lot of work is hidden beneath the surface of the few results that eventually become an article, including entire projects. For me, the attempt on reaching high fidelity transfers in europium was such a project. Similarly, the detection of a single cerium ion has continued to elude us, and a new problem of permanent trapping was discovered instead. The electromagnetically induced transparency article contains a quick method for generating coherence from a mixed state, but we have not identified a place for it in quantum computing so far. In contrast, even though the qubit-qubit interaction project is not finalized yet, the initial results are promising. In conclusion, you might say that the quantum computing progress has been slowly stumbling forward for the past few years. Fortunately, the group has recently expanded and new people and fresh insights will hopefully bring us beyond the single cerium detection step, which has been an obstacle for a long time, into the uncharted territory of single ion quantum computing using rare-earth-ion-doped crystals.

Learning theory, running simulations, and performing experiments have been the continuous cycle of working here, and the feeling when the last piece of knowledge falls into place, when the coding error is finally resolved, or when the oscilloscope displays those expected, but highly awaited, results, is according to me one of the best things about working in science.

Another great benefit is the diversity, both in the people with whom you work, but also in what you do: some days you are truly a physicist trying to understand nature; the next day you work as an (amateur) programmer, debugging your code; a (rookie) chemist, mixing and preparing the dye solution for the laser; a (make-believe) detective, attempting to locate faulty equipment by examining evidence, ruling out unlikely candidates, and investigating the list of suspects until the culprit is found; or, finally, as a (novice) writer when results should be published, or as in this case, when the words of your PhD should be composed into a book.

APPENDIX A

EQUIPMENT

In order to concentrate on the physics of the papers included in this thesis, I have moved most descriptions of the experimental setups from the main chapters to this appendix. In Section A.1, the setup used in all papers except Paper **VIII** is explained. Even the papers that are mostly theoretical, Papers **I** and **VII**, have some experiments associated with them and have used this setup. Section A.1 has three subsections: the dye laser setup, which includes the pulse creation and part of the locking setup; the rest of the locking setup; and the most common experimental setup on the cryostat table, as well as how it was modified for the various experiments.

Brief information about the liquid helium bath cryostat is provided in Section A.2, and the cerium setup used for Paper **VIII** is explained in Section A.3.

A.1 Main setup

Thanks to present and previous members of our group, a (mostly) well working system has been developed, including a tunable dye laser that is locked to an ultra low expansion glass cavity; a Rabi frequency calibration system; and high level coding, such as "Create_pit" and "Create_170kHz_qubit" used to initialize a qubit as seen in Figures 7.2 and 7.3 in just two code lines. The following subsections briefly review the equipment used. For more information, see previous overviews of the system in, for example, references [107–110], keeping in mind that some parts have been updated through the years, e.g., we are no longer locking the laser to a crystal, as was done when the system was initially developed, but to a cavity instead.

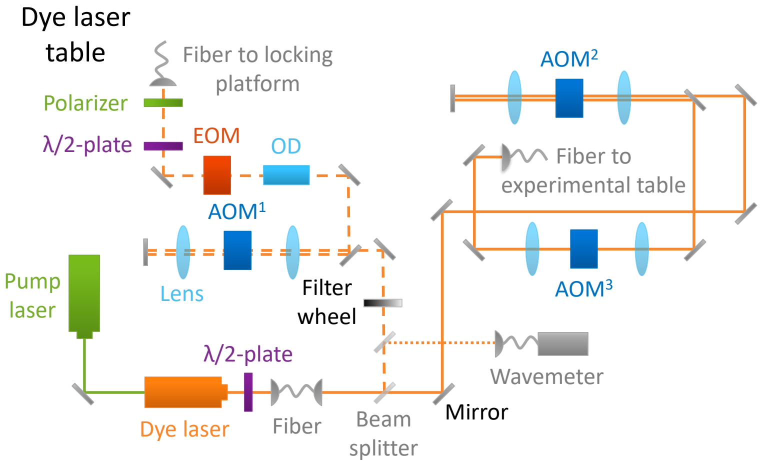

Figure A.1. *Experimental setup of the dye laser table, see Section A.1.1 for more information.*

A.1.1 Dye laser setup

The setup on the dye laser table, which can be seen in Figure A.1, is inside a cleanroom in order to minimize disturbances from dust. A 6W 532 nm Verdi-V6 solid state laser pumps the dye laser of type Coherent 699-21. The dye is Rhodamine 6G mixed with ethylene glycol pumped at 4.2 bar and cooled to 10°C, with a tuning range of approximately 570-635 nm and possible output powers of ∼1 W at 580 nm (Eu^{3+}:Y_2SiO_5) and ∼600 mW at 606 nm (Pr^{3+}:Y_2SiO_5).

The laser mode is cleaned up with a single mode polarization maintaining (PM) fiber, where a half-wave plate, as well as some mirrors that are not shown in the figure, are used to align the incoupling. A small fraction of the transmitted light is split off using a beam splitter and sent towards the locking platform (dashed line). Another beam splitter reflects some light into a wavemeter (dotted line), HighFinesse WS-6IR, whereas the transmission (dashed line) goes through a filter wheel and a double pass acousto-optic modulator (AOM^1), Brimrose GPF-1125-750-590, which is capable of tuning the frequency by up to 1.5 GHz in the two passes. An optical Faraday rotator and two polarizers are then used as an optical diode (OD) to let light through in this direction only. An electro-optical modulator (EOM), New Focus 4002, generates sidebands at 50 MHz, which are used for the laser locking. The light is sent to the locking platform, explained in Section A.1.2, via another fiber, where the incoming beam polarization is aligned with a half-wave plate and a polarizer.

The majority of the light from the laser is transmitted through

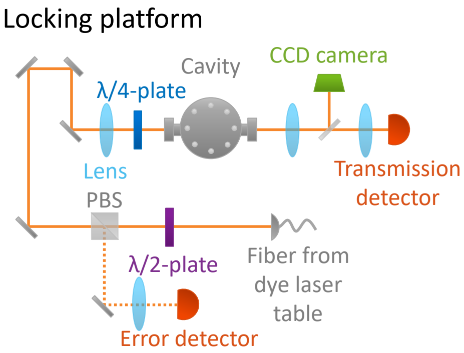

Figure A.2. *Located on an actively stabilized platform is a cavity that is used to lock the dye laser. See Section A.1.2 for more details.*

the first beam splitter (solid line) and is sent into a double pass AOM[2], AA.ST.200/B100/A0.5-vis, which can alter the frequency, phase, and/or amplitude of the transmitted light, and is used to create pulses. A single pass AOM[3], AA.ST.360/B200/A0.5-vis (recently changed to a 60 MHz AOM of type Isomet 1205C-2) is used to generate two-color pulses when needed by sending in an RF signal containing two frequencies, usually separated by 10.2 MHz, i.e., the ground hyperfine splitting between $|0\rangle$ and $|1\rangle$ in $\mathrm{Pr}^{3+}{:}\mathrm{Y_2SiO_5}$. Both AOMs are controlled by an arbitrary waveform generator (Tektronix AWG520) through LabView and MatLab scripts. Finally, the light is guided into a fiber connected to the experimental table, which is explained in Section A.1.3.

This setup has remained fairly unchanged during my thesis work. However, updates have recently been made with regard to fiber noise stabilization in an effort to improve the laser linewidth at the crystal location. None of these changes have been included in Figure A.1, since they were not used for any experiments in this thesis.

A.1.2 Dye laser locking

A small fraction of the dye laser light is guided to the locking platform, as seen in Figure A.2. The platform is actively stabilized against vibrations using a Table Stable TS-140. The light is linearly polarized and contains sidebands at 50 MHz. A half-wave plate makes sure that the polarization direction is vertical before the light is transmitted through a polarizing beam splitter cube (PBS). Using a few mirrors and a lens, the light is coupled into an ultra-stable cavity, before which a quarter-wave plate is located. The cavity is kept at 10°C and a pressure of 10^{-9} mbar to 10^{-8}

mbar. Any reflection from the cavity is rotated once more by the quarter-wave plate, resulting in a total rotation of 90 degrees, i.e., turning the light polarization from vertical to horizontal. The PBS splits off this horizontally polarized reflection (dotted line), which is then focused onto a homebuilt error detector [110] to be used in the Pound-Drever-Hall locking technique, explanations of which can be found in references [107, 111]. The designed linewidth of the locking system is 10 Hz, but no experiments have been performed to verify it, as it would require an equally stable reference.

The cavity transmission can be examined with both a CCD (charge-coupled device) camera to look at the spatial mode, and another homebuilt detector [110].

Normally, the frequency of a locked laser is limited to the discrete locations of the cavity modes, separated in our case by a mode spacing of roughly 3.3 GHz. However, by frequency shifting the light reaching the cavity, using AOM^1 shown in Figure A.1, the dye laser can be locked at almost any frequency. Since the tuning range of the AOM is only approximately half that of the cavity mode spacing, it needs to be realigned with the $+1$ or -1 order of the AOM to cover most of the frequency space. More commonly, the AOM is kept at one alignment at the price of being able to reach only half of all available frequencies. This option to lock at most frequencies is important for experiments that benefit from being in the center of the inhomogeneous absorption profile.

A.1.3 Experimental table

In contrast to the setups described so far, the equipment on the experimental table is always changing. However, most of my experiments have had a fairly simple and common starting point, as shown in Figure A.3.

Using AOM^2 and AOM^3, seen in Figure A.1, arbitrary pulses within a wide frequency range can be created, and are sent via a fiber to the experimental table, Figure A.3. A beam splitter reflects a small fraction of the light (dashed line), which is then focused onto a reference detector, Thorlabs PDB150A, used to calibrate for laser intensity fluctuations and the frequency dependent AOM efficiency, which is not always perfectly compensated for by the calibration system. The majority of the light (solid line) passes through a half-wave plate and a polarizer, which are used to orient the linear polarization to the desired crystal axis. Afterwards, the light is focused into the cryostat and propagates through the crystal before it is collimated and eventually focused onto the transmission detector, Thorlabs PDB150A. In most experiments, a focus size of approximately 100 μm was used inside the crystal, but for more precise details, see the articles.

The experiments performed in Paper **I** used a setup similar to the one described above, but where the half-wave plate and

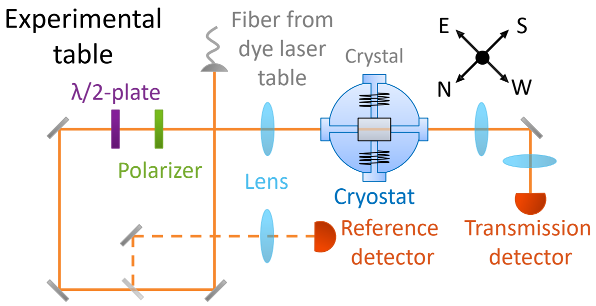

Figure A.3. *The most common components of the experimental setup on the cryostat table. See Section A.1.3 for more information.*

polarizer switched places, and a second polarizer was added after the cryostat to measure polarization specific transmission.

For the setup in Paper **II** a second polarizer was again added after the cryostat, as well as another transmission detector, Hamamatsu PMT (photomultiplier tube) R943-02, to measure the very weak light when propagating through the high absorption regions of the crystal. A schematic view of this setup can be seen in Figure 5.4 in Section 5.2.

In Paper **III**, a heterodyne detection scheme was used, i.e., another beam splitter was inserted before the cryostat to create a reference beam that when overlapped with the transmitted beam after the cryostat, results in a beating pattern at the difference frequency.

The setup used in Papers **IV**-**VI** was precisely the one seen in Figure A.3.

Even though Paper **VII** is a theoretical article, I performed experiments on Eu^{3+}:Y_2SiO_5 using a similar setup as before, but with a pinhole after the cryostat to probe only the transmission from ions radially centered in the focus in an attempt to reach transfer fidelities above 99%. Due to a lack of available laser power, i.e., Rabi frequency, the desired pulse scheme could not be fully tested and the results were not good enough for publication.

Finally, the signals were analyzed using an oscilloscope, either Tektronix TDS 540 or LeCroy WaveRunner HRO66Zi, and all data treatment was performed using LabView or MatLab.

A.2 Cryostat

The cryostat used for all experiments in my thesis has been a liquid helium bath cryostat from Oxford Instruments of type spectromag-4000-8. The sample space is a 25 mm diameter cylinder, inside

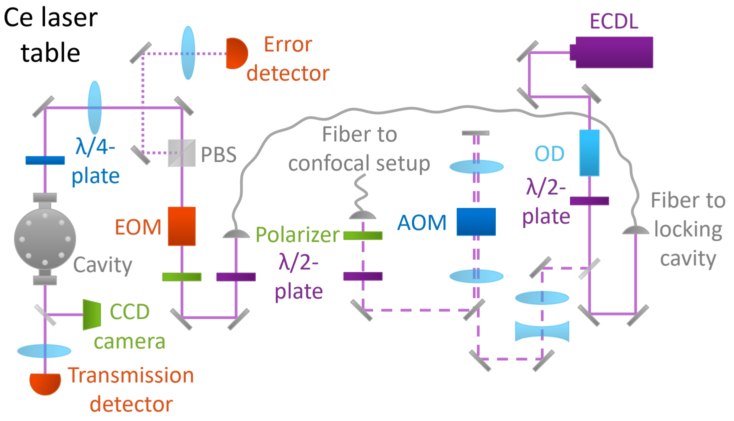

Figure A.4. *The 371 nm external cavity diode laser setup with locking and pulse creation can be seen, and is explained further in Section A.3.*

which the crystal is mounted in a holder at the end of an approximately 1 m long sample rod. The outer vacuum shield is normally pumped by either Leybold PT 70 F Compact or Pfeiffer Vacuum HiCube 80Eco to around 10^{-6} mbar to 10^{-5} mbar.

The cryostat is oriented as shown in Figure A.3 in a northeast → southwest direction and the Earth's magnetic field is north: 17.1 µT; east: 1.2 µT; and down: 47.4 µT (2017) [95]. To compensate for this field, three coils, one in each direction, have been added outside the cryostat, but have been used only in Paper **V**. The cryostat also contains two superconducting magnets capable of reaching 8 T along the direction perpendicular to the light shown in Figure A.3, but a much smaller field of about 10 mT to 100 mT has typically been used.

A.3 Cerium (Ce) setup

The setup used for Paper **VIII** is different from the other articles, as it operates in the ultraviolet. The 371 nm laser setup can be seen in Figure A.4 and is mounted on a 75 cm by 90 cm movable optical table. The external cavity diode laser (ECDL) uses a littrow configuration with a 371 nm laser diode, Sacher SAL-372-10. The light passes through an optical diode (OD), Thorlabs IO-5-370-HP, after which a half-wave plate is located. The reflection from a beam splitter (dashed line) passes through a telescope that shrinks the beam size before it is sent into an AOM, Isomet 1250C-829A, in double pass configuration. Using a pickup mirror, the transmitted light passes through a half-wave plate and a polarizer before a fiber guides it to the confocal microscope setup, as explained in Section 7.5, Figure 7.22, and reference [87].

The main part of the light (solid line) passes through the beam splitter after the OD and into a fiber that carries it to the locking part of the setup. The polarization is rotated and cleaned up using a half-wave plate and a polarizer before an EOM, Linos PM25 KD*P, generates sidebands at 20 MHz. The light is transmitted through a polarizing beam splitter cube (PBS) and focused into an ultra-stable cavity before which a quarter-wave plate is located. The transmitted light can be observed using both a normal detector, S5973-02 photo diode and Femto HCA-10M-100k amplifier [110], as well as a CCD camera, PointGrey Firefly. The reflection from the cavity is once more rotated by the quarter-wave plate such that the PBS reflects the light (dotted line) into the error detector, modified version of Femto HCA-S-200M-Si-FS [110].

This laser is also locked using the Pound-Drever-Hall locking technique [107, 111]. More detailed information about the cerium setup can be found in references [87, 110, 112, 113].

THE AUTHOR'S CONTRIBUTION TO THE PAPERS

Note that the thesis author previously published under Adam N. Nilsson.

I **Wave propagation in birefringent materials with off-axis absorption or gain**
M. Sabooni, A. N. Nilsson, G. Kristensson, and L. Rippe.
Phys. Rev. A **93**, 013842 (2016).

Simulations, experiments, and the first draft of an article regarding wave propagation through birefringent crystals with off-axis absorption were initially performed by Mahmood Sabooni. The most important results are that the absorption coefficient generally varies during propagation due to the rotation of the polarization inside the crystal, and that steady state polarizations exist, i.e., polarizations that do not change during propagation.
I continued the research and performed new simulations, which caused us to modify most of the article, which I rewrote, and draw new conclusions.

II **Development and characterization of high suppression and high étendue narrowband spectral filters**
A. Kinos, Q. Li, L. Rippe, and S. Kröll.
Appl. Opt. **Vol. 55 No. 36**, 10442 (2016).

A high suppression (53.4 ± 0.7 dB) narrowband (1.25 MHz) spectral filter was created in Pr^{3+}:Y_2SiO_5. The filter was analyzed with respect to ultrasound optical tomography (UOT), and simulations were performed in order to study the potential étendue of the filters.
I performed all simulations, experiments, analysis, and wrote the manuscript.

III **Slow-light-based optical frequency shifter**
Q. Li, Y. Bao, A. Thuresson, A. N. Nilsson, L. Rippe, and S. Kröll.
Phys. Rev. A **93**, 043832 (2016).

Optical pulses were frequency shifted (±4 MHz) using the linear DC Stark and slow light effects in Pr^{3+}:Y_2SiO_5. The device is controlled by an external voltage and we claim that the solid angle of acceptance could be close to 2π.
I contributed to discussions, especially regarding the analysis, simulations, and manuscript.

IV **Using electric fields for pulse compression and group-velocity control**
Q. Li, A. Kinos, A. Thuresson, L. Rippe, and S. Kröll.
Phys. Rev. A **95**, 032104 (2017).

A group-velocity controller, based on the DC Stark and slow light effects in a Pr^{3+}:Y_2SiO_5 crystal, was shown to alter the velocity of light pulses from 1.5 km/s to 30 km/s without significant loss or distortion. A proof of principle experiment was also performed, which temporally compressed a pulse by a factor of approximately 2.
Qian Li and I performed all experiments together, and I was then included in discussions about the simulations, analysis, and manuscript.

V **Fast all-optical nuclear spin echo technique based on EIT**
A. Walther, A. N. Nilsson, Q. Li, L. Rippe, and S. Kröll.
Eur. Phys. J. D **70:**, 166 (2016).

Using electromagnetically induced transparency (EIT), an all-optical Raman spin echo technique, which is capable of inducing coherence directly from a mixed state, was analyzed experimentally and in simulations.
I performed the simulations, joined Andreas Walther for the experimental work, and was involved in discussions about the analysis and manuscript.

VI **Towards CNOT operations using ensemble qubits**
A. Kinos, L. Rippe, A. Walther, and S. Kröll.
(2018) *Manuscript in preparation.*

Qubit-qubit interactions based on the dipole blockade effect are studied using two ensemble qubits in Pr^{3+}:Y_2SiO_5. To minimize the effect of off-resonant excitation, an interleaved optical pumping scheme is used during the qubit initialization. Furthermore, the number of interacting ions are shown to grow quadratically with the ion density per frequency channel, and to decrease at a slower rate compared to the background absorption when repeating the preparation scheme.
I prepared and performed the experiments, analyzed the data, and wrote the manuscript.

VII **High-fidelity readout scheme for rare-earth solid-state quantum computing**
A. Walther, L. Rippe, Y. Yan, J. Karlsson, D. Serrano, A. N. Nilsson, S. Bengtsson, and S. Kröll.
Phys. Rev. A **92**, 022319 (2015).

A single ion readout scheme is presented, where a buffer ion is used to improve qubit readout fidelity. A CNOT-gate fidelity with and without readout is calculated, and the scalability to several qubits is investigated.
I contributed to discussions. The Eu^{3+}:Y_2SiO_5 high fidelity transfer experiments, which I performed, should have been included in this article, but due to a lack of available Rabi frequency, the fidelities were never publication worthy.

VIII **High-resolution transient and permanent spectral hole burning in Ce^{3+}:Y_2SiO_5 at liquid helium temperatures**
J. Karlsson*, A. N. Nilsson*, D. Serrano, A. Walther, P. Goldner, A. Ferrier, L. Rippe, and S. Kröll;
(*Authors contributed equally).
Phys. Rev. B **93**, 224304 (2016).

A slow permanent trapping in Ce^{3+}:Y_2SiO_5 was analyzed, as well as spectral hole burning in the Zeeman levels, where an upper bound on the homogeneous linewidth (3 ± 2 MHz) of the 4f-5d transition was estimated.
Jenny Karlsson and I performed all experiments together, and both of us analyzed the data and wrote the manuscript.

ACKNOWLEDGEMENTS

As is often the case, I have too many people to thank for their help with respect to my PhD: from my first teachers, who laid the foundation of my math and physics interest, to the current colleagues with whom I perform experiments. I will nevertheless try to list a few by name and mention some of the assistance they have provided.

First and foremost, I thank my main supervisor Stefan Kröll for always being there to help, always having time to discuss, and allowing me to focus on what I find most interesting. My co-supervisors Andreas Walther, for all the discussions about quantum mechanics, for ever-present help, and for letting me share your room for a while; and Peter Samuelsson, for being a nice and warm person who always says that things seem to be going well with my PhD.

Lars Rippe for constantly talking, be it about physics or other topics; it really contributes to the group's spirit. Qian Li for letting me be a part of the slow light experiments, the general discussions, the laughs, and being an absolutely perfect office mate. Jenny Karlsson for the cerium experiments and the always happy smile. Ying Yan for laying the foundation of the cerium project before I started, and recently returning to perform high fidelity transfer experiments with me. Diana Serrano for all her knowledge about rare-earth crystals. Mahmood Sabooni for letting me continue the wave propagation simulations and manuscript, and Gerhard Kristensson for many helpful discussions about the same project.

To the students whom I have helped supervise: Pernilla Helmer for being the first one, and an exemplary one at that; Philip Dalsbecker for efforts and discussions about spectral filters; and Vassily Kornienko for the constant enthusiasm about our work, it lights up the day.

To the collaborators whom I have worked with: Philippe Goldner, Alban Ferrier, John Bartholomew, Karmel De-Oliveira Lima, Ivan Scheblykin, and Axel Thuresson, thank you so much for your help and dedication.

To all, both previous and present, group members whom I have had the pleasure to meet, I thank you for the work you are do-

ing, and for continuing to make the quantum information group a wonderful and happy workplace.

A special thanks to all administrative and technical personal: Anne Petersson Jungbeck for always having the answers to all my questions; Åke Johansson for on several occasions fixing my computer and helping with other equipment; Jakob Testad for taking care of the financial issues; and Leif Magnusson and Stefan Schmiedel for always having helium available, even on very short notice.

Thanks to Anders Persson for help with the teaching and fixing lasers, and to Lars Engström for planning and keeping track of the doctoral teaching.

To the SPIE/OSA chapter members, thanks for all the events and fun activities.

I would also like to thank the entire atomic division for their company during lunches at work, Friday meetings, and Monday cakes.

Finally, I extend my gratitude and thanks to my friends and family, especially my wife Linnéa and daughter Vega, for being there when I need it, for believing in me, and making me smile.

REFERENCES

1. R. P. Feynman, R. B. Leighton and M. Sands. *The Feynman Lectures on Physiscs - Volume 1.* AddisonWesley (1963).
2. R. P. Feynman, R. B. Leighton and M. Sands. *The Feynman Lectures on Physiscs - Volume 2.* AddisonWesley (1963).
3. R. P. Feynman, R. B. Leighton and M. Sands. *The Feynman Lectures on Physiscs - Volume 3.* AddisonWesley (1963).
4. NASA Earth Observatory. *Planetary Motion* (2017). URL `https://earthobservatory.nasa.gov/Features/OrbitsHistory/`.
5. NASA. *100 Years of General Relativity* (2017). URL `https://asd.gsfc.nasa.gov/blueshift/index.php/2015/11/25/100-years-of-general-relativity/`.
6. J. Gleick and H. Roberts. *Genius: The Life and Science of Richard Feynman.* LSB (1995).
7. S. M. Blinder. *Radiation Pulse from an Accelerated Point Charge* (2017). URL `http://demonstrations.wolfram.com/RadiationPulseFromAnAcceleratedPointCharge/`.
8. R. N. Shakhmuratov. *The energy storage in the formation of slow light.* Journal of Modern Optics **57**, PII 920439128 (2010).
9. E. Courtens. *Giant Faraday Rotations In Self-induced Transparency.* Physical Review Letters **21**, 3 (1968).
10. M. Sabooni, Q. Li, L. Rippe, R. K. Mohan and S. Kröll. *Spectral Engineering of Slow Light, Cavity Line Narrowing, and Pulse Compression.* Physical Review Letters **111**, 183602 (2013).
11. R. N. Shakhmuratov, A. Rebane, P. Megret and J. Odeurs. *Slow light with persistent hole burning.* Physical Review A **71**, 053811 (2005).
12. A. Walther, A. Amari, S. Kröll and A. Kalachev. *Experimental superradiance and slow-light effects for quantum memo-*

ries. Physical Review A **80**, 012317 (2009).

13. R. P. Feynman. *Quote from The Character of Physical Law - Part 6: Probability and uncertainty - the quantum mechanical view of nature* (1965). URL `https://en.wikipedia.org/wiki/The_Character_of_Physical_Law`.
14. J. J. Sakurai and J. Napolitano. *Modern quantum mechanics.* Pearson Education (2011).
15. M. Born. *Zur Quantenmechanik der Stoßvorgänge [On the quantum mechanics of collisions].* Zeitschrift für Physik **37**, 863–867 (1926).
16. Wikipedia. *Copenhagen interpretation* (2017). URL `https://en.wikipedia.org/wiki/Copenhagen_interpretation`.
17. F. Bloch. *Nuclear Induction.* Physical Review **70**, 460–474 (1946).
18. R. P. Feynman, F. L. Vernon and R. W. Hellwarth. *Geometrical Representation of the Schrödinger Equation for Solving Maser Problems.* Journal of Applied Physics **28**, 49–52 (1957).
19. L. Allen and J. H. Eberly. *Optical resonance and two-level atoms.* Wiley New York (1975).
20. P. W. Milonni and J. H. Eberly. *Lasers.* John Wiley & Sons New York (1988).
21. E. Fraval, M. J. Sellars and J. J. Longdell. *Dynamic decoherence control of a solid-state nuclear-quadrupole qubit.* Physical Review Letters **95**, 030506 (2005).
22. E. Fraval. *Minimising the decoherence of rare earth ion solid state spin qubits.* PhD thesis The Australian National University (2005).
23. M. J. Zhong, M. P. Hedges, R. L. Ahlefeldt, J. G. Bartholomew, S. E. Beavan, S. M. Wittig, J. J. Longdell and M. J. Sellars. *Optically addressable nuclear spins in a solid with a six-hour coherence time.* Nature **517**, 177–U121 (2015).
24. M. F. Pascual-Winter, R. C. Tongning, T. Chaneliere and J. L. Le Gouet. *Spin coherence lifetime extension in* Tm^{3+}*:YAG through dynamical decoupling.* Physical Review B **86**, 184301 (2012).
25. A. Arcangeli, M. Lovric, B. Tumino, A. Ferrier and P. Goldner. *Spectroscopy and coherence lifetime extension of hyperfine transitions in* $^{151}Eu^{3+}:Y_2SiO_5$. Physical Review B **89**, 184305 (2013).
26. G. Heinze, C. Hubrich and T. Halfmann. *Stopped Light and*

Image Storage by Electromagnetically Induced Transparency up to the Regime of One Minute. Physical Review Letters **111**, 033601 (2013).

27. P. W. Milonni. *Why Spontaneous Emission.* American Journal of Physics **52**, 340–343 (1984).
28. H. B. Callen and T. A. Welton. *Irreversibility and Generalized Noise.* Physical Review **83**, 34–40 (1951).
29. R. R. Puri. *Spontaneous Emission - Vacuum Fluctuations or Radiation Reaction.* Journal of the Optical Society of America B-optical Physics **2**, 447–450 (1985).
30. P. W. Milonni. *Spontaneous Emission - Vacuum Fluctuations or Radiation Reaction by Puri - Comment.* Journal of the Optical Society of America B-optical Physics **2**, 1953–1954 (1985).
31. M. Pollnau. *What we thought we knew and what we ought to know about stimulated and spontaneous emission.* Presentation given at Lund University (15th November 2017).
32. G. Steele. *The Physics of Spontaneous Emission and Quantum Mechanical Decay.* Department of Physics, MIT, MA 02139 (2000).
33. L. Fonda, G. C. Ghirardi and A. Rimini. *Decay Theory of Unstable Quantum Systems.* Reports on Progress in Physics **41**, 587–631 (1978).
34. G. C. Ghirardi, C. Omero, T. Weber and A. Rimini. *Small-time Behavior of Quantum Non-decay Probability and Zeno Paradox in Quantum-mechanics.* Nuovo Cimento Della Societa Italiana Di Fisica A-nuclei Particles and Fields **52**, 421–442 (1979).
35. J. H. Eberly, N. B. Narozhny and J. J. Sanchezmondragon. *Periodic Spontaneous Collapse and Revival in a Simple Quantum Model.* Physical Review Letters **44**, 1323–1326 (1980).
36. Wikipedia. *Spontaneous emission* (2017). URL `https://en.wikipedia.org/wiki/Spontaneous_emission`.
37. H. Walther, B. T. H. Varcoe, B. G. Englert and T. Becker. *Cavity quantum electrodynamics.* Reports on Progress in Physics **69**, 1325–1382 (2006).
38. Y. C. Sun. *Spectroscopic Properties of Rare Earths in Optical Materials - Chapter 7.* Springer Series in Material Science (2005).
39. R. M. Macfarlane and R. M. Shelby. *Coherent transient and holeburning spectroscopy of rare earth ions in solids.* In

A. Kaplyanskii and R. Macfarlane, editors, *Spectroscopy of solids containing rare earth ions*. North-Holland Amsterdam (1987).

40. A. J. Freeman and R. E. Watson. *Theoretical Investigation of Some Magnetic and Spectroscopic Properties of Rare-earth Ions*. Physical Review **127**, 2058 (1962).
41. F. Könz, Y. Sun, C. W. Thiel, R. L. Cone, R. W. Equall, R. L. Hutcheson and R. M. Macfarlane. *Temperature and concentration dependence of optical dephasing, spectral-hole lifetime, and anisotropic absorption in* Eu^{3+}*:* Y_2SiO_5. Physical Review B **68**, 085109 (2003).
42. W. M. Yen, A. L. Schawlow and W. C. Scott. *Phonon-induced Relaxation in Excited Optical States of Trivalent Praseodymium in* Laf_3. Physical Review A-general Physics **136**, A271 (1964).
43. S. B. Altner, G. Zumofen, U. P. Wild and M. Mitsunaga. *Photon-echo attenuation in rare-earth-ion-doped crystals*. Physical Review B **54**, 17493–17507 (1996).
44. Z. Q. Sun, M. S. Li and Y. C. Zhou. *Thermal properties of single-phase* Y_2SiO_5. Journal of the European Ceramic Society **29**, 551–557 (2009).
45. L. Petersen. *High-resolution spectroscopy of praseodymium ions in a solid matrix: towards single-ion detection sensitivity*. PhD thesis ETH Zurich (2011).
46. G. H. Dieke and H. M. Crosswhite. *The Spectra of the Doubly and Triply Ionized Rare Earths*. Applied Optics **2**, 675–686 (1963).
47. W. T. Carnall, G. L. Goodman, K. Rajnak and R. S. Rana. *A Systematic Analysis of the Spectra of the Lanthanides Doped into Single-crystal* Laf_3. Journal of Chemical Physics **90**, 3443–3457 (1989).
48. R. W. Equall, R. L. Cone and R. M. Macfarlane. *Homogeneous Broadening and Hyperfine-structure of Optical-transitions In* Pr^{3+}*:*Y_2SiO_5. Physical Review B **52**, 3963–3969 (1995).
49. M. Nilsson, L. Rippe, S. Kröll, R. Klieber and D. Suter. *Hole-burning techniques for isolation and study of individual hyperfine transitions in inhomogeneously broadened solids demonstrated in* Pr^{3+}*:*Y_2SiO_5. Physical Review B **70**, 214116 (2004).
50. T. Aitasalo, J. Holsa, M. Lastusaari, J. Legendziewicz, J. Niittykoski and F. Pelle. *Delayed luminescence of* Ce^{3+} *doped* Y_2SiO_5. Optical Materials **26**, 107–112 (2004).

51. R. Beach, M. D. Shinn, L. Davis, R. W. Solarz and W. F. Krupke. *Optical-absorption and Stimulated-emission of Neodymium In Yttrium Orthosilicate.* Ieee Journal of Quantum Electronics **26**, 1405–1412 (1990).

52. R. C. Hilborn. *Einstein Coefficients, Cross-sections, F Values, Dipole-moments, and All That.* American Journal of Physics **50**, 982–986 (1982).

53. F. R. Graf, A. Renn, G. Zumofen and U. P. Wild. *Photon-echo attenuation by dynamical processes in rare-earth-ion-doped crystals.* Physical Review B **58**, 5462–5478 (1998).

54. R. W. Equall, Y. Sun, R. L. Cone and R. M. Macfarlane. *Ultraslow Optical Dephasing In* Eu^{3+}*:*Y_2SiO_5*.* Physical Review Letters **72**, 2179–2181 (1994).

55. F. R. Graf, A. Renn, U. P. Wild and M. Mitsunaga. *Site interference in Stark-modulated photon echoes.* Physical Review B **55**, 11225–11229 (1997).

56. S. E. Beavan, E. A. Goldschmidt and M. J. Sellars. *Demonstration of a dynamic bandpass frequency filter in a rare-earth ion-doped crystal.* Journal of the Optical Society of America B-optical Physics **30**, 1173–1177 (2013).

57. M. P. Hedges. *High performance solid state quantum memory.* PhD thesis Australian National University (2011).

58. K. Holliday, M. Croci, E. Vauthey and U. P. Wild. *Spectral Hole-burning and Holography in an* Y_2SiO_5*:*Pr^{3+} *Crystal.* Physical Review B **47**, 14741–14752 (1993).

59. H. de Riedmatten and M. Afzelius. *Quantum Light Storage in Solid State Atomic Ensembles.* In A. Predojević and M. M.W., editors, *Engineering the Atom-Photon Interaction.* Springer New York (2015).

60. L. Rippe, B. Julsgaard, A. Walther, Y. Ying and S. Kröll. *Experimental quantum-state tomography of a solid-state qubit.* Physical Review A **77**, 022307 (2008).

61. H. Zhang, M. Sabooni, L. Rippe, C. Kim, S. Kröll, L. V. Wang and P. R. Hemmer. *Slow light for deep tissue imaging with ultrasound modulation.* Applied Physics Letters **100**, 131102 (2012).

62. M. J. Digonnet. *Rare-earth-doped fiber lasers and amplifiers, revised and expanded.* CRC press (2001).

63. C. W. Thiel, R. L. Cone and T. Boettger. *Laser linewidth narrowing using transient spectral hole burning.* Journal of Luminescence **152**, 84–87 (2014).

64. A. Walther, L. Rippe, L. V. Wang, S. Andersson-Engels and

S. Kröll. *Analysis of the potential for non-invasive imaging of oxygenation at heart depth, using ultrasound optical tomography (UOT) or photo-acoustic tomography (PAT)*. Biomedical Optics Express **8**, 4523–4536 (2017).

65. C. Clausen, F. Bussieres, M. Afzelius and N. Gisin. *Quantum Storage of Heralded Polarization Qubits in Birefringent and Anisotropically Absorbing Materials*. Physical Review Letters **108**, 190503 (2012).

66. J. H. Wesenberg, K. Mølmer, L. Rippe and S. Kröll. *Scalable designs for quantum computing with rare-earth-ion-doped crystals*. Physical Review A **75**, 012304 (2007).

67. A. Orieux and E. Diamanti. *Recent advances on integrated quantum communications*. Journal of Optics **18**, 083002 (2016).

68. R. P. Feynman. *Simulating Physics with Computers*. International Journal of Theoretical Physics **21**, 467–488 (1982).

69. S. Lloyd. *Universal quantum simulators*. Science **273**, 1073–1078 (1996).

70. R. P. Poplavskii. *Thermodynamic models of information processes*. Soviet Physics Uspekhi **18**, 222 (1975).

71. Y. Manin. *Computable and Uncomputable (in Russian)*. Sovetskoye Radio, Moscow (1980).

72. Wikipedia. *Timeline of quantum computing* (2017). URL `https://en.wikipedia.org/wiki/Timeline_of_quantum_computing`.

73. P. W. Shor. *Algorithms for Quantum Computation - Discrete Logarithms and Factoring*. 35th Annual Symposium on Foundations of Computer Science, Proceedings pages 124–134 (1994).

74. L. K. Grover. *A fast quantum mechanical algorithm for database search*. In *Proceedings of the twenty-eighth annual ACM symposium on Theory of computing* pages 212–219. ACM (1996).

75. T. Kadowaki and H. Nishimori. *Quantum annealing in the transverse Ising model*. Physical Review E **58**, 5355 (1998).

76. IBM. *Quantum Computing* (2017). URL `https://www.research.ibm.com/ibm-q/`.

77. Google. *Quantum AI* (2017). URL `https://research.google.com/pubs/QuantumAI.html`.

78. Microsoft. *Quantum Computing* (2017). URL `https://www.microsoft.com/en-us/quantum/`.

79. Intel. *Quantum Computing* (2017). URL https://newsroom.intel.com/press-kits/quantum-computing/.

80. D-Wave. *The Quantum Computing Company* (2017). URL https://www.dwavesys.com/home.

81. D. P. Divincenzo. *Topics in quantum computers.* Mesoscopic Electron Transport **345**, 657–677 (1997).

82. D. P. DiVincenzo. *The physical implementation of quantum computation.* Fortschritte Der Physik-progress of Physics **48**, 771–783 (2000).

83. Quantum Technologies Roadmap. *2015 edition of the European roadmap for Quantum Information Processing and Communication* (2015). URL http://www.osa.org/en-us/corporate_gateway/publications/publication_report_library/quantum_technologies_roadmap/.

84. European Commission. *Quantum Technology Flagship* (2017). URL https://ec.europa.eu/digital-single-market/en/policies/quantum-technologies.

85. T. Zhong, J. M. Kindem, J. Rochman and A. Faraon. *Interfacing broadband photonic qubits to on-chip cavity-protected rare-earth ensembles.* Nature Communications **8** (2017).

86. T. Zhong, J. M. Kindem, J. G. Bartholomew, J. Rochman, I. Craiciu, E. Miyazono, M. Bettinelli, E. Cavalli, V. Verma, S. W. Nam, F. Marsili, M. D. Shaw, A. D. Beyer and A. Faraon. *Nanophotonic rare-earth quantum memory with optically controlled retrieval.* Science **357**, 1392–1395 (2017).

87. J. Karlsson, L. Rippe and S. Kröll. *A confocal optical microscope for detection of single impurities in a bulk crystal at cryogenic temperatures.* Review of Scientific Instruments **87**, 033701 (2016).

88. R. M. Macfarlane. *High-resolution laser spectroscopy of rare-earth doped insulators: a personal perspective.* Journal of Luminescence **100**, PII S0022–2313(02)00450–7 (2002).

89. M. S. Silver, R. I. Joseph, C. N. Chen, V. J. Sank and D. I. Hoult. *Selective-population Inversion in Nmr.* Nature **310**, 681–683 (1984).

90. M. S. Silver, R. I. Joseph and D. I. Hoult. *Selective Spin Inversion in Nuclear Magnetic-resonance and Coherent Optics through an Exact Solution of the Bloch-riccati Equation.* Physical Review A **31**, 2753–2755 (1985).

91. I. Roos and K. Mølmer. *Quantum computing with an inhomogeneously broadened ensemble of ions: Suppression of errors from detuning variations by specially adapted pulses and co-*

herent population trapping. Physical Review A **69**, 022321 (2004).

92. B. Lauritzen, N. Timoney, N. Gisin, M. Afzelius, H. de Riedmatten, Y. Sun, R. M. Macfarlane and R. L. Cone. *Spectroscopic investigations of* Eu^{3+}*:*Y_2SiO_5 *for quantum memory applications.* Physical Review B **85**, 115111 (2012).
93. P. Helmer. *High fidelity operations in a europium doped inorganic crystal.* Bachelor's thesis Lund University (2015).
94. M. A. Nielsen and I. L. Chuang. *Quantum Computation and Quantum Information.* Cambridge University Press 10th anniversary edition (2010).
95. National centers for environmental information. *Geomagnetism* (2017). URL https://www.ngdc.noaa.gov/geomag/magfield.shtml.
96. B. S. Ham, M. S. Shahriar, M. K. Kim and P. R. Hemmer. *Frequency-selective time-domain optical data storage by electromagnetically induced transparency in a rare-earth-doped solid.* Optics Letters **22**, 1849–1851 (1997).
97. D. Serrano, Y. Yan, J. Karlsson, L. Rippe, A. Walther, S. Kröll, A. Ferrier and P. Goldner. *Impact of the ion-ion energy transfer on quantum computing schemes in rare-earth doped solids.* Journal of Luminescence **151**, 93–99 (2014).
98. I. Kurkin and K. Chernov. *EPR and spin-lattice relaxation of rare-earth activated centres in* Y_2SiO_5 *single crystals.* Physica B+C **101**, 233–238 (1980).
99. M. S. Buryi, V. V. Laguta, D. V. Savchenko and M. Nikl. *Electron Paramagnetic Resonance study of* Lu_2SiO_5 *and* Y_2SiO_5 *scintillators doped by cerium.* Advanced Science, Engineering and Medicine **5**, 573–576 (2013).
100. R. Kolesov, K. Xia, R. Reuter, R. Stohr, A. Zappe, J. Meijer, P. R. Hemmer and J. Wrachtrup. *Optical detection of a single rare-earth ion in a crystal.* Nature Communications **3**, 1029 (2012).
101. R. Kolesov, K. Xia, R. Reuter, M. Jamali, R. Stohr, T. Inal, P. Siyushev and J. Wrachtrup. *Mapping Spin Coherence of a Single Rare-Earth Ion in a Crystal onto a Single Photon Polarization State.* Physical Review Letters **111**, 120502 (2013).
102. P. Siyushev, K. Xia, R. Reuter, M. Jamali, N. Zhao, N. Yang, C. Duan, N. Kukharchyk, A. D. Wieck, R. Kolesov and J. Wrachtrup. *Coherent properties of single rare-earth spin qubits.* Nature Communications **5**, 3895 (2014).
103. K. Xia, R. Kolesov, Y. Wang, P. Siyushev, R. Reuter, T. Kornher, N. Kukharchyk, A. D. Wieck, B. Villa, S. Yang and

J. Wrachtrup. *All-Optical Preparation of Coherent Dark States of a Single Rare Earth Ion Spin in a Crystal.* Physical Review Letters **115**, 093602 (2015).

104. T. Utikal, E. Eichhammer, L. Petersen, A. Renn, S. Goetzinger and V. Sandoghdar. *Spectroscopic detection and state preparation of a single praseodymium ion in a crystal.* Nature Communications **5**, 3627 (2014).
105. E. Eichhammer, T. Utikal, S. Gotzinger and V. Sandoghdar. *Spectroscopic detection of single Pr^{3+} ions on the $^3H_4$-$^1D_2$ transition.* New Journal of Physics **17**, 083018 (2015).
106. I. Nakamura, T. Yoshihiro, H. Inagawa, S. Fujiyoshi and M. Matsushita. *Spectroscopy of single Pr^{3+} ion in LaF_3 crystal at 1.5 K.* Scientific Reports **4**, 7364 (2014).
107. L. Rippe. *Quantum Computing With Naturally Trapped Sub-Nanometre-Spaced Ions.* PhD thesis Lund University (2006).
108. A. Walther. *Coherent Processes In Rare-Earth-Ion-Doped Solids.* PhD thesis Lund University (2009).
109. M. Sabooni. *Efficient Quantum Memories Based on Spectral Engineering of Rare-Earth-Ion-Doped Solids.* PhD thesis Lund University (2013).
110. J. Karlsson. *Cerium as a quantum state probe for rare-earth qubits in a crystal.* PhD thesis Lund University (2015).
111. E. D. Black. *An introduction to Pound-Drever-Hall laser frequency stabilization.* American Journal of Physics **69**, 79–87 (2001).
112. X. Zhao. *Diode laser frequency stabilization onto an optical cavity.* Master's thesis Lund University Lund Reports on Atomic Physics LRAP-473 (2013).
113. Y. Yan. *Towards single Ce ion detection in a bulk crystal for the development of a single-ion qubit readout scheme.* PhD thesis Lund University (2013).

Printed by Media-Tryck, Lund 2018 NORDIC SWAN ECOLABEL 3041 0903

This thesis, written by Adam Kinos, contains research on wave propagation in absorbing birefringent crystals, slow light applications, and quantum computing using rare-earth-ion-doped crystals, as well as extensive light-matter interaction discussions surrounding the same topics.

LUND UNIVERSITY
Faculty of Engineering, LTH
Department of Physics
Division of Atomic Physics

ISBN: 978-91-7753-543-0 (print)
ISBN: 978-91-7753-544-7 (pdf)
ISSN 0281-2762
Lund Reports on Atomic Physics, LRAP-543 (2018)

LUND
UNIVERSITY